



CRANFIELD UNIVERSITY

School of Engineering

MSc Thesis

Academic Year: 2019-2020

BARCELO ADROVER, Marc

**Multi-Physics Investigation of Ferro- and
Magneto-hydrodynamic effects in Non-Isothermal
Non-Newtonian Blood Flows with relevant application in
Medical and Aerospace fields**

Supervisor:

Dr. László Könözsy

© Cranfield University, 2020.
All rights reserved. No part of this publication may be reproduced
without the written permission of the copyright holder.

Except where acknowledged in the customary manner, the material presented in this thesis is, to the best of my knowledge, original and has not been submitted in whole or part for a degree in any university.

A handwritten signature in black ink, appearing to read "Marc Barceló Adrover".

Marc Barceló Adrover

Abstract

The aim of this report is to investigate how magnetic fields influence the blood flow by considering Non-Isothermal Ferro- and Magnetohydrodynamic effects. These have been implemented via UDF in ANSYS-FLUENT software and results have been validated with [1]. The presence of the a localized magnetic field induces the apparition of two energetic vortexes which are dependent on the field intensity and severely affect the blood flow.

Since blood behaves, according to experimental results, as a shear-thinning fluid; Non-Newtonian models are required if more accuracy in the flow model is desired. Power-Law, Standard Casson, K-L Casson, Modified Casson and Quemada Models have been adapted and then implemented in the blood flow due to their high performance. Their results have been conveniently compared and, as it is witnessed, Casson- family models have proven excellent accuracy even though Quemada entails more versatility and ability to describe any shear-thinning Non-Newtonian flow.

Recent investigations suggest that further changes on the viscosity must be done in order to yield effects such as the orientation of Red Blood Cells under the perturbation of a magnetic field. This is why, the function proposed by [2] has been here considered and simulated. Results show more consistency with what one should logically expect.

Depending on the proximity of the blood vessel to the heart but also on the vessel's geometry, the velocity of the inflow will be pulsatile. Thus, a high-fidelity of the most severe case -the aorta inflow- has been modeled from a real systole-diastole cycle and evaluated in the present document.

Finally, the linear onset of the Rayleigh-Bénard instability has been investigated for two different blood flows, with laminar and turbulent cases. The parametric study is performed. A pattern of steady Bénard Cells has been obtained for the Laminar, while Turbulent logically arises chaotic and energetic structures which suffer from dissipation and diffusion. This instability is also studied in conjunction with the FHD and MHD effects for the localized magnetic field, studying how both vortex cores interact.

Acknowledgements

In the first place, I would like to acknowledge and give my full gratitude to my supervisor, Dr. László Könözsy, for his guidance and support during all the investigation. It is specially important to consider hence, given the current covid-19 situation, he has weekly shown availability to discuss my MSc Thesis and help me with advice and suggestions when needed; but also with all my classmates, which totally demonstrates capabilities, will and professionalism. Besides, he has been really supportive through all the decisions and investigation paths I have taken during this Individual Research Project. Nonetheless, it is still fair to recognize his labour during this MSc ACE course. In the end, one realizes how much he has learnt and feels confident to face problems that one did not expect previously. This fact could not be achieved without the structured learning and module choices performed by Dr. Könözsy. Once this document is submitted, I look forward to publishing with him all the outstanding findings gathered within this document and further investigate it together.

Regarding the MSc Aerospace Computational Engineering, a classmate and friend with whom it has been a pleasure to work with is Mr. Julio Maldonado. From the first assignment until the Group Design Project, we have worked and helped each other always aiming for the highest mark possible. I am certain we both are proud of what we have submitted together, resulting in very solid assignments. Therefore, I would like to acknowledge his hard work, rigor and collaborative spirit.

It would not be honest if I did not mention my gratitude to my family, particularly my brother Joan, and parents Xisca and Andreu who have always supported me -it did not matter which challenge did arise. They have made an enormous effort to make both of their sons achieve their dreams and goals. And they still do.

I feel that it is really important to show how thankful I am with my dearest friend, Ignacio Martínez Suárez, and his family: Carmen, Manolo, Juan and Irene. During the complicated covid-19 outbreak, I could not return back home since my family presents health issues. They offered their hospitality, and with an outstanding generosity, they

hosted me, gave me love, and treated like a son for a couple of months. Both my family and I are in a great debt for their benevolence, and look forward to seeing them once this difficult situation is no longer present. But also, I wanted to seize this opportunity to say "thank you very much Nacho, for being by my side during the 6 most important years of my life". He has never deceived me and has helped in many occasions even though I did not ask for help. Whenever I will be in the future, you will always have a really close friend and a home to stay.

During the making of this document, I still remember and acknowledge the work of my previous supervisor, Dr. Ignacio Izpura Torres, and the whole department in which I had the pleasure to carry out the BSc Thesis. I learned a lot through their guidance of one of my passions, electrodynamics, and felt really lucky to work with them. I would undoubtedly repeat this experience if it is presented in a near future.

Finally, but not least, I would like to recognize the support and work of my uncle Dr. Gabriel Rebassa, who is currently aiding people overcome the Covid-19 illness in order to have another chance to live. During all these years, he has backed me up and helped every time a health question did arise in my head. Now, regarding the fact that this investigation is strongly related with his work field, Medicine, I wanted to dedicate this research to him.

To any reader of this document, I sincerely hope you enjoy it and that it turns to be useful for your investigation.

Contents

Abstract	v
Acknowledgements	vii
List of Figures	xiii
List of Tables	xiv
Abbreviations	xv
Symbols	xvi
1 Introduction	1
1.1 Background and Motivation	1
1.2 Literature Review	2
1.2.1 Blood Rheology	3
1.2.2 Ferro- and magneto-hydrodynamics (FHD, MHD)	4
1.2.3 Numerical Modelling of the Blood Flow	4
1.2.4 Instabilities	6
1.2.5 Non-Newtonian Models	10
1.2.6 Multiphase Flow	12
1.2.7 Applications of similar investigations	15
1.3 Structure of the M.Sc. Thesis	17
2 Theory fundamentals	19
2.1 Flow Mechanics and Maxwell Governing Equations	19
2.1.1 Navier-Stokes Continuity equation	19
2.1.2 Navier-Stokes Momentum equation	20
2.1.3 Navier-Stokes Energy Equation	20
2.1.4 Maxwell Governing Equations	21
2.2 Blood Composition and Rheology	22

2.2.1	Blood Cells	22
2.2.2	Blood Plasma	24
2.3	FHD/ MHD approach	25
2.3.1	Magnetohydrodynamic Effect (MHD)	25
2.3.2	Ferro-hydrodynamic Effect (FHD)	26
2.4	Coupled Flow Mechanics Equations with the MHD and FHD contribution	29
2.4.1	Coupled Momentum Equation	29
2.4.2	Coupled Energy Equation	30
2.5	Bénard-Rayleigh Convective Instability	30
2.6	Non-Newtonian Flows	36
2.6.1	Non-Newtonian Models	37
2.6.1.1	Simple and Generalized Power Law	37
2.6.1.2	Casson	38
2.6.1.3	Casson-type K-L	40
2.6.1.4	Modified Casson	40
2.6.1.5	Quemada model	41
2.7	Multiphase Hemodynamics	43
2.7.1	Effects	44
2.7.1.1	Roleaux - Smoluchowski effect	44
2.7.1.2	Fahraeus effect	45
2.7.1.3	Fahraeus-Lindqvist effect	45
2.7.1.4	Additional Effects	45
3	Methodology	46
3.1	Problem Description	46
3.1.1	Physical Application. 2-D Turbulent biomagnetic fluid flow in a rectangular channel, localized magnetic field	46
3.1.2	Geometry and Mesh	49
3.2	Numerical Setup	50
3.2.1	SIMPLE Algorithm	50
3.2.2	Turbulence Modelling	52
3.2.2.1	Realizable k- ε turbulence model	53
4	Results	54
4.1	Validation Case	54
4.1.1	Turbulent 2-D Rectangular duct with Localized Constant Magnetic Field	54
4.2	Non-Newtonian Model Investigation	67
4.2.1	Newtonian	69

4.2.2	Casson	70
4.2.3	Modified Casson	71
4.2.4	Casson-type K-L	72
4.2.5	Quemada	73
4.2.6	Comparison of the Velocity and WSS Contours	75
4.3	Magnetoviscous Contribution	82
4.4	Pulsatile Velocity Inlet	86
4.5	Rayleigh-Bénard Convective Instability	92
4.5.1	Tzirtzilakis Conditions	92
4.5.1.1	Turbulent	93
4.5.1.2	Laminar	102
4.5.2	Amendment on Tzirtzilakis Blood Modelling	104
4.5.2.1	Laminar Case	106
4.5.2.2	Turbulent Case	109
4.6	Ferro- and Magneto-hydrodynamic effects in conjunction with Rayleigh-Bénard Instability	116
4.6.1	Thermal difference of $T = 50$ K	116
4.6.2	Thermal difference of $T = 100$ K	118
5	Conclusions	120
5.1	Introduction	120
5.2	Validation and FHD/MHD Effects	121
5.3	Non-Newtonian Modelling for Blood Shear-Thinning behaviour	122
5.4	Apparent viscosity change due to erythrocyte orientation	124
5.5	High-Fidelity Aorta Velocity Function	124
5.6	Rayleigh-Bénard Convective Instability	125
5.7	Rayleigh-Bénard Convective Instability in conjunction with Ferro and magneto-hydrodynamic effects	126
5.7.1	Final Ideas and Future Work	127
Bibliography		128
6	Appendix	137
6.1	Appendix 1. Convergence Study. Residual Plots	137
6.2	Appendix 2. UDF Code	144
6.3	Appendix 3. MATLAB Code	156
6.3.1	Non-Newtonian Plot Code	156
6.3.2	Rayleigh-Bénard Plot Code	163

List of Figures

2.1	Chemical formulation of Hemoglobin	23
2.2	Typical hysteresis -or magnetization- curve (M against H) for a ferrofluid. Source: [3]	27
2.3	Flow in a channel heated in both superior and inferior impermeable walls	31
2.4	Rayleigh-Benard Stability Threshold, Neutral Curve.	36
2.5	Shear stress vs shear rate typical curve for the Casson model. Source: [4]	39
2.6	Two-Phase Scheme of the Blood Flow	43
3.1	Flow Geometry Scheme	46
3.2	2-D Blood Flow Geometry Scheme	49
3.3	2-D Blood Flow Mesh	50
4.1	Application of the magnetic field with initial and final transition, and subsequent magnetization of the fluid	56
4.2	Velocity Results for different magnetic fields and Mn_M , Mn_F parameters, Re=400, Turbulent Case	58
4.3	x-Velocity Results for different magnetic fields and Mn_M , Mn_F parameters, Re=400, Turbulent Case	60
4.4	Y-Velocity Results for different magnetic fields and Mn_M , Mn_F parameters, Re=400, Turbulent Case	61
4.5	Temperature Contours for different magnetic fields and Mn_M , Mn_F parameters, Re=400, Turbulent Case	63
4.6	Streamlines comparison with Tzirtzilakis [1] for Cases 1 and 5	65
4.7	Comparison of effective viscosity against shear rate for the Non-Newtonian Models	67
4.8	Results for the Newtonian Model, B=10 T	69
4.9	Results for the Casson Model, B=10 T	70
4.10	Results for the Modified Casson Model, B=10 T	71
4.11	Results for the K-L Casson-type Model, B=10 T	72
4.12	Results for the K-L Quemada Model, B=10 T	73

4.13	Velocity profiles for the different Newtonian and Non-Newtonian Models, at different sections along the x axis	76
4.14	WSS Curves for the Newtonian Case, B=10T. Red: Upper Wall, Blue: Lower Wall	79
4.15	WSS Distribution in the Upper Wall for the Non-Newtonian Models, B=10T	80
4.16	WSS Distribution in the Lower Wall for the Non-Newtonian Models, B=10T	80
4.17	Effective Viscosity for the Newtonian Case, B=10T	82
4.18	Effective Viscosity with the Magnetoviscous Contribution, B=10T	83
4.19	WSS Contour along the Upper Wall for the Newtonian and the Model with the Magnetoviscous* Additional Contribution	84
4.20	WSS Contour along the Lower Wall for the Newtonian and the Model with the Magnetoviscous* Additional Contribution	84
4.21	Velocity Waveform in the Aorta. Source: [5]	86
4.22	Pulsatile Velocity Inlet Model	87
4.24	Transient Simulation of Pulsatile Velocity Flow. Evaluation of the FHD/MHD effect	90
4.25	Transient Simulation of Rayleigh Bénard Instability, t=0.1 s. Laminar Case	95
4.26	Transient Simulation of Rayleigh Bénard Instability, t=4.7 s. Laminar Case	96
4.27	Transient Simulation of Rayleigh Bénard Instability, t=6.7 s. Laminar Case	97
4.28	Transient Simulation of Rayleigh Bénard Instability, t=15.3 s. Laminar Case	98
4.29	Transient Simulation of Rayleigh Bénard Instability, t=24.2 s. Laminar Case	99
4.30	Transient Simulation of Rayleigh Bénard Instability, t=40 s. Laminar Case	100
4.31	No Rayleigh-Bénard instability onset for ΔT of 0.19 K, Ra=1541 . . .	102
4.32	Rayleigh-Bénard instability onset for $\Delta T = 1$ K	103
4.33	Rayleigh number parametric dependency	105
4.34	Laminar Transient RBI Simulation. Contours of Magnitude Velocity and Z-Vorticity	107
4.35	Transient Simulation of Rayleigh Bénard Instability, variation of ΔT . .	108
4.36	Transient Simulation of Rayleigh Bénard Instability, variation of ΔT . .	109
4.37	Turbulent Simulation t = 65 s	110
4.38	Turbulent Simulation, t= 142 s	111
4.39	Turbulent Simulation, t= 280 s	112
4.42	Turbulent Transient Simulation for Blood Flow Rayleigh-Bénard Convection onset, thermal case study	114
4.43	Real Velocity Systole Inlet, $\Delta T = 100$ K	115
4.44	Steady Flow variables, FHD/MHD coupled with RBI for $\Delta T = 50$ K . .	117

4.45	Temperature contour time evolution, FHD/MHD coupled with RBI for $\Delta T = 50 \text{ K}$	118
4.46	Steady Flow variables, FHD/MHD coupled with RBI for $\Delta T = 100 \text{ K}$	119
6.1	Residual Plot for $B=2 \text{ T}$	137
6.2	Residual Plot for $B=10 \text{ T}$	138
6.3	Residual Plot for Newtonian Model	138
6.4	Residual Plot for Standard Casson Model	139
6.5	Residual Plot for Modified Casson Model	139
6.6	Residual Plot for K-L Casson Model	140
6.7	Residual Plot for Quemada Model	140
6.8	Residual Plot for the Magnetoviscous additional contribution	141
6.9	Residual Plot for Pulsatile Inflow	141
6.10	Residual Plot for Bénard-Rayleigh Convection	142
6.11	Residual Plot for Turbulent Bénard-Rayleigh Convection	142
6.12	Residual Plot for Bénard-Rayleigh Convection in conjunction with FHD/MHD term	143

List of Tables

3.1	Additional mesh quality information	50
4.1	Conditions evaluated in Turbulent 2-D Rectangular duct with Localized Constant Magnetic Field	55
4.2	Localized magnetic field induction and magnetization flow parameters to be studied	56
4.3	Non-Newtonian Deviations from the Newtonian Model at $x/h=3$	77
4.4	Non-Newtonian Deviations from the Newtonian Model at $x/h=7$	77
4.5	Non-Newtonian Deviations from the Newtonian Model at $x/h=13$	78
4.6	Flow Condition Values for the Simulations of Blood in a 2-D Rectangular Channel. Investigation of Rayleigh-Bénard Instability.	93
4.7	Corrected Flow Condition Values for the Simulations of Blood in a 2-D Rectangular Channel. Investigation of Rayleigh-Bénard Instability.	104
4.8	Critical Temperature Different for different medical cannula sections.	105

Abbreviations

2D	Two Dimensions
3D	Three Dimensions
BC	Boundary Conditions
CAD	Computer Aided Design
CFD	Computational Fluid Dynamics
CFL	Courant-Friedrichs-Levy Number
DOF	Degrees of Freedom
DNS	Direct Numerical Simulation
FHD	Ferro-hydrodynamics
FEA	Finite Element Analysis
FEM	Finite Element Method
FDS	Finite Difference Splitting Scheme
GCI	Grid Convergence Index
LES	Large Eddy Simulations
MHD	Magneto-hydrodynamics
MUSCL	Monotonic Upstream-Centered Scheme for Conservation Laws
N-S	Navier-Stokes Equations
PDE	Partial Derivative Equation
RANS	Reynolds Average Navier-Stokes
Re	Reynolds Number
RBC	Red Blood Cells
RBI	Rayleigh-Bénard Instability
SST	Shear Stress Transport model
WSS	Wall Shear Stress

Symbols

E_T	Energy
E_c	Eckert Number
ϵ	Strain tensor
F	Force
∇	Nabla Operator
Δ	Laplacian operator or increment.
g	gravity field
q	Heat Flux
J	Jacobian
l	Length
L	Lift force
λ	Eigenvalue linearized solution
M	Mach number
μ	Kinematic viscosity
ν	Dynamic viscosity
∂	Partial derivative operator
p	Pressure
π	Pi number
Pr	Prandtl Number
Ra	Rayleigh Number
Re	Reynolds Number
ρ	Density
S	Surface
σ	Cauchy stress tensor, conductivity
t	Time
T	Temperature
τ	Reynolds stress tensor component
\mathbf{u}	Flow velocity
u	Flow speed X component

v	Flow speed Y component
w	Flow speed Z component
ω	Natural frequency
x	First spatial component
y	Second spatial component
z	Third spatial component

Chapter 1

Introduction

1.1 Background and Motivation

The irruption of the recent 5-G broadband communications systems has produced two opposing effects on population: whilst some received the news with tremendous fears and imagined conspiracy theories, other defend the applications and convenience of this technology and argue that there are no harmful effects caused by it. The reality is that none of the both is fully backed up by scientific evidence even though the first slope derived in inconsistencies and untrustworthy non-scientific discourses.

The reality is that science has paid more attention to ionizing radiation which evidently has a demonstrable and huge impact on real life in short, medium and long terms. Proofs of it is the modification of genetic properties in species and specially in trees in order to select a mutation which has the most beneficial or practical properties (size, pomace-pine ratio, etc), cancer treatments with radiotherapy, or unfortunate to mention, human fatalities such as the still present Chernobyl accident or the Hiroshima-Nagasaki bombs. However, even though all the mentioned above have an artificial trait, the reality is that nature also hits us with the same medicine. According to the American Cancer Society, Cancer -which is an anomalous and harmful effect of human cells- of the skin is diagnosed in 5.4 million of inhabitants per year in the US country as a result of the solar radiation. And this is produced even the fact that gamma radiation (γ), which is definitely the most harmful, is quite-fully stopped by the highest layers of the atmosphere.

Given the severe impact of the ionizing radiation, one could think that mild fields (non-ionizing) are not definitely such harmful. But the truth is that it remains unknown by science, since their effects are difficult to document. Nonetheless, the fact that our current society is completely and constantly immersed and exposed to non-ionizing radiation,

1. Introduction

there could be some effects that must be given attention and carefully investigated. And this is the aim of this document, to demonstrate the influence of electromagnetic steady fields in the blood flow. The effects described in here are not totally new since techniques such as Magnetic Drug Targeting and Heat Transfer enhancement by introducing ferromagnetic particles in oil are direct applications of this principle. However, there are still many effects to discover and so more improvements to conduct on the mathematical model description of the blood flow and our human body.

From this investigation, some conclusions could help to future medicine. Furthermore, one of the motivations of our study and which is totally involved in the aerospace environment, is the understanding of which phenomena do take place in reentry space missions when astronauts are exposed to hostile and salvage electrodynamic fields which can reach up to 1000 Teslas. Even though no direct diseases have been derived from astronauts, the limited number of them and the slow lapse of time in which they have been investigated, no firm conclusions can be pronounced by now. Hence we hope that this work could entail a theoretical further step to understand these complex phenomena produced in space missions during reentry stages.

1.2 Literature Review

The topic dealt in this document is as interesting as challenging in the same time. One could think to investigate as many traits of the title as he wanted: as supervisor Dr. Könözsy pointed "it is a lifetime and eternal investigation". Lots of researches have been done parallelly regarding the evident medical aspect, how to characterize the flow, proposals of modelling the complex flow behaviour (including the systole-diastole cycle) and geometries, yet the problem still rises more questions to be solved than answers. This is why, the literature to be reviewed is wide and the problem is attacked through different perspectives and therefore a scheme of the publications reviewed in order to fully acknowledge the problem turns to be necessary.

The disposition of the read publications will follow the logical order of starting with the analysis of the blood rheology and its model, to then review the governing equations that motivate its behaviour. Afterwards, different models to describe the flow (Non-Newtonian characterization, turbulence definition, etc) will be detailed. Third, an statement of the Ferrohydrodynamic and Magnetocaloric insights which are going to be developed in the analyzed problem will be conveniently discussed. Finally, possible practical applications of the present work such as the magnetic drug targeting, extra-corporeal blood processes, cancer treatment and non-widely explored sensitivity to electrodynamic sources will be commented.

1. Introduction

1.2.1 Blood Rheology

In order to properly model an element , first, a surgeon work must be carried out. The deep and thorough investigation of the element is required until the essence of it is fully acknowledged. This research must keep digging until the most tiny components that give information on the topic are reached. Once achieved, the personal criteria will govern which elements are important to consider and which effects are important to mathematically describe. When this stage is fully finished -and it might be one of the most important- the mathematical description of the designed model takes place.

This is why, in our research, the first stages were governed by documenting about publications and textbooks about what was known as blood, which are their components, how it behaves in terms of fluid mechanics and its reactivity to electric and magnetic fields based on the charged particles that it constantly carries throughout the circulatory system. The most useful publications in the understanding and description of blood could not be more than medical encyclopedia and biochemistry text books such as [6], [7] and even [8] in which a brief but interesting detail of how blood behaves in the presence of steady magnetic fields due to its components is provided.

Then, the two phenomena governing the reactivity of a fluid in these circumstances, the FHD and MHD models have been revised. The first one has been known by years and has been described elegantly in [9] but it was not applied to blood or what is known as "bio-fluids" until Haik et al [10]. The second phenomenon was described by [11] when he was studying the solar dynamics. Both effects were merged together by [12], which supposed a pioneering step yet his mathematical description can be further improved. More information about the MHD and FHD and publications reviewed in order to understand their nature will be accordingly developed in the following subsection.

Then, the shear-thinning Non-Newtonian behaviour of blood, which is actually most of times neglected, has been the second trait to observe and investigate. Several models such as the Bingham, Power-Law, Carreau, Casson and Herschel-Bulkley have been used in a large series of papers to model the blood. However, according to [13] where most of the previous Non-Newtonian models have been compared, the Casson and Herschel-Bulkley might be the most interesting to consider. This Newtonian and non-Newtonian model will be further detailed in the following lines.

As it has been known, the different components of blood -which sometimes are considered as homogeneous- will have a strong influence in the flow behaviour. The charged proteins suspended in the plasma layer and the ferromagnetic Hemoglobin in the Red Blood

1. Introduction

Cells will provide different but noticeable impact on the flow when it is examined under the action of magnetic fields. This is why, multi-phase hemodynamics has been also examined in order to know which have been the models used by up-to-date investigations for these particular components.

1.2.2 Ferro- and magneto-hydrodynamics (FHD, MHD)

Both sciences have had different origins until they were merged together by Tzirtzikis when modelling the blood in [12].

The Magnetohydrodynamics was initially proposed by [11] when he tried to bring some light on the solar dynamics. One of the most basic principle behind it is the contribution of the Lorentz force to the momentum equation (which will evidently provide a dissipation term in the energy equation) as a consequence of charged particles travelling with a determined speed along an electric or magnetic field.

In the other hand, the Ferrohydrodynamics evolved when ferritic colloidal fluids were studied and when fuel efficiency was intended to be enhanced by the introduction of particles of the same material. This is why, the introduction of the magnetization curve, in a medium in which there's a gradient of the magnetic field or even a gradient of temperature, is considered. Old publications and text books such as [9] demonstrate the basis of this principle with great detail. Haik et al first considered this application into biofluids in [10]. It has been later revisited by [14].

Even though it has been commented that Tzirtzikis is known to be the pioneer in applying both principles in the blood flow study, several publications such as [15] suggested this idea in general fluids. However, since the work from [16] but also in [17], it was assumed that the MHD term was almost negligible and hence the posterior studies only embraced the FHD theory.

There are several investigations nowadays that demonstrate the necessity of applying both together. One example of it is the contribution from [8] where the blood rheology and erythrocytes orientation is carefully reviewed besides the fact that their aim is to explain how to experimentally investigate the action of external fields on blood.

1.2.3 Numerical Modelling of the Blood Flow

The work made by Tzirtzikis in [12] aims to mathematically model the blood flow under the action of magnetic fields by considering the FHD terms introduced by Haik et al [10] but also the MHD effect from Alfvén [11]. Hence, the influence of the magnetization effects regarding the erythrocytes and the Lorentz Forces created by the ionized particles into the

1. Introduction

blood plasma are considered. Here, blood is unfortunately assumed to be Newtonian and the methodology of the solver is a pressure-linked pseudo-transient method (PLEM). In order to account for these effects, the simulations are evaluated with the Hartmann flow problem (case II) - in which logically only the MHD force will be present- and a spatially varying magnetic field (case I). In the results, the flow regime is notably decreased due to the magnetic field influence, specially important for the deoxygenated blood case. Besides, when the spatially varying magnetic field is evaluated, two vortical structures appear and largely influence the blood flow as a consequence of this magnetic field gradient. Nonetheless, if this gradient is set to zero (being this case the Hartmann Flow) no secondary vortices take place. Generally, reductions of the overall flow have been obtained with up to a 40 % of the axial velocity when strong fields are applied, which gives an idea of the susceptibility of this biofluid to electrodynamic sources even when they are not considered as ionizing radiation.

Even though Tzirakis et al [18] recognize the validity of the former Newtonian approach in blood model for shear rates higher than 100 s^{-1} , they clearly state the need of the Non-Newtonian blood characterization. This effect is even more considerable when cyclic inlet conditions simulating the systole-diastole signal and subsequent unsteady flow, or for arteries and veins with smaller sections or injured as a result of different injuries such as stenosis. Hence, their aim is to improve the mathematical unified model proposed by Tzirtzikis [12] by considering the Non-Newtonian behaviour of the blood, thus, a merging and transition function will be required. The choice of the Non-Newtonian stress tensor model has been the Herschel-Bulkley (instead of the widely used Casson model) since its additional DOF permits a more accurate description of the flow. Besides, according to [19], Casson model struggles with the prediction of velocity profiles for arteries with small diameters ($<0.065\text{ mm}$).

Another important improvement introduced by this work has been the magnetoviscous model, which is additive to the normal viscosity, and will therefore be proportional to the magnetic field. In some cases, this effect has reached an influence of 11.6 % which is indeed significant. Regarding the numerical setup, the pressure correction scheme introduced by Patankar [20] with the additional contributions made by Botti and Di Pietro [21] in order to deal with discontinuous velocity profiles is implemented and validated. An important remark made by the authors, in terms of geometry meshing, is that they strongly encourage using hexahedral elements as, according to De Santis et al [22], the same level of accuracy can be achieved by using 1/6 of the commonly used tetrahedrals. Two cases have been studied by Tzirakis et al: a Couette flow and then a pulsatile flow in which the heart pump is simulated. The function they used to model this systole-diastole cycle has been provided as well. As main outcomes of the investigation, they clearly state

1. Introduction

a significant deviation of the flow even caused by moderate magnetic fields. Furthermore, the additive magnetoviscous term proposed in this publication has also demonstrated an important contribution and significant effects on the flow behaviour.

1.2.4 Instabilities

The publication from Finlayson [23] is one of the first to study the Rayleigh-Bénard convective instability of a ferromagnetic fluid under the action of a constant magnetic field such that the intensity H and its magnetic induction B are parallel. It is assumed that, according to [16] the MHD contribution is negligible in a charge-free fluid such as the dipole-dipole magnetic interactions regarding [24]. The effect of gravity will be also considered,

The first section faced is the derivation of the equations, where the incompressibility constraint is imposed. It is shocking that the convective term is absent in the N-S momentum equation. Viscosity is assumed to be isotropic, and constant, therefore it is not sensitive to the magnetic field such as in [18]. The Boussinesq approach is logically used as it will only permit the variation of density regarding the mass forces term. In a similar manner, the temperature is equally derived by invoking the Fourier Law. Regarding the magnetocaloric effect, the Maxwell Laws for non-conductive fluids are also recalled. The boundary conditions have been applied (a difference of temperatures in the upper plate and lower plate, with an averaging middle temperature parameter T_a such that $T_a = \frac{1}{2}(T_u + T_l)$ whilst density is calculated with the equation of state $\rho = \rho_0(1 - \alpha(T - T_a))$, being α the thermal expansion coefficient. The solution for the steady state are easily derived. However, the stability of the solution must be studied and hence a linear stability analysis is performed. The normal mode hypothesis or separation of variables is used and then the stability equations are expressed in the dimension-less form. Thanks to this, it is more easy to establish the dependency of the flow variables sensitivity to the different contributions. Magnetic numbers, Prandtl, Rayleigh and magnetic departure of linearity have been the most significant parameters. The solution for this set of stability equations is straightforward in the case of free-free boundaries, but in the case of solid entail the use of a Galerkin-type method which aims to solve the algebraic set of equations: $L \cdot W = a \cdot R^{1/2} \cdot M \cdot W$, being L the linearizing coefficient, W the velocity perturbation field, R the Rayleigh stability number, a the waveform parameter, and M the conservative field of variables. From the results, consistency with the prior publications is observed. In the linear regime the classical problem of Rayleigh is obtained where $Ra=1707.8$ is achieved as the threshold of stability. However, when the stability is studied under the effects of buoyancy, the magnetic number has also to say on the stability and therefore it

1. Introduction

is coupled with the Rayleigh critical number. Given the results, it must be concluded that the magnetization gradient will induce a convection movement if the magnetization curve of the fluid is a function of the temperature and hence if a gradient of temperature does take place.

The job of Finlayson [23] has been indeed used in most of the convective stability analysis of ferrofluids, however, his method can be further improved. One example of the enhancements conducted is the publication from (Stiles, Kagan; 1989) in [25] where the Galerkin Method is deeply boosted and hence more-rapidly converging results are obtained. The prediction of the critical values are successfully explicitly computed, which is nobel given the stability problems that this method usually arises. The results, which are in good agreement with Finlayson, determine that gravity tends to destabilize the solution and help the onset of the convective instability as the critical values on its absence are consistently bigger.

A very light and introductory definition of the Rayleigh-Bénard convection in Micropolar fluids has been provided in [26] where the general definition of the problem plus 4 literature reviews on this phenomena investigation has been performed. As it is known, Micropolar fluids do not posses symmetrical stress tensor, as they model Non-Newtonian fluids with random polarized particles in the flow. The importance of it is the fact that blood can be considered as one case of it and therefore the interest of evaluating this problem. A particularity arised by this definition is the two independent variables held by micropolar fluid dynamics: the velocity vector and the spin. Therefore, micropolar fluids cannot be fully described by the Navier-Stokes Equations and the additional equations proposed by Eringen at [27] become necessary. Actually, the micropolar theory is not as hard to implement as conventional fluid dynamics due to the power and simplicity of their mathematical description. Here, some insights of the Hydrodynamic Stability Theory proposed by [28] and giving special attention to the Rayleigh-Bénard Convection is commented. It is interesting to note that, according to Iridis et al, regarding the Bénard-Marangoni effect, the presence of suspended microparticles delays the apparition of the Bénard-Convection cells established -for determined boundaries- above Rayleigh number $Ra > 1708$. This linear stability analysis has been further improved by recent development of [29] where the Fourier heat Conduction Law was replaced by the Maxwell-Cattaneo formulation, using Galerkin scheme for different boundaries.

Following the previous principles from Goel [26], the full investigation conducted by Abraham in [30] has been the most complete publication reviewed dealing with the Rayleigh-Bénard Convection in micropolar ferromagnetic fluids. An original vertical magnetic field such as in [1] is analytically studied by evaluating different boundary conditions on the

1. Introduction

channel walls: isothermal, free-free, spin-vanishing and infinity magnetic susceptibility for a stationary flow case. The results have been compared to the typically studied Newtonian case such as in [31], [32], [33], [34], [35], [25]. However, it must be said that the Boussinesq approach taken here and in many publications do not offer the best result on the Rayleigh-Bénard convection if the density is considered to be constant. This has been the main drawback noted on the publication, as the mathematical derivation provided is exquisite and totally in-depth. Interestingly enough, Abraham demonstrates the possibility of having the Bénard convection cells when the upper plate is heated instead of the lower, but this can only take place in micropolar fluids for very large Rayleigh number (Ra) flows. The results provided show high quality as several pioneer set of magnetization parameters (M_1, M_3) and micropolar fluid parameters (N_1, N_3 and N_5) are used and hence give total versatility to the problem, and will clearly differentiate the cause of the behaviour if the parametric study is properly conducted. Remarkably, the critical wave number shows sensitivity to the magnetization parameters but does not to micropolar parameters. Besides, these simulations are compared to the classic Newtonian fluid case.

As it has been detailed, the blood can be considered as a Casson-type fluid. Therefore, the work from Aghighi et al in which the Rayleigh convection of Casson fluids is examined could entail interesting outcomes to bare for our investigation. One of the easiest models to implement that account for the Non-Newtonian shear-thinning behaviour of fluids is the Bingham model, due to this, it might be the most used in numerical investigation. However, as it may be evident, this apparent simplicity incurs in artificial results frequently. Therefore, Herschel-Bulkley or Casson fluids remain a more reliable approach to the real-life investigation whilst considering the effect of the yield stress. When those two models have been adopted, several remarkable results have been obtained: the yield stress has a stabilizing effect, the steady state solution remains stable in a linear-ish mode for the inelastic viscoplastic flows [36] and that convection does take place for wide perturbations and if the intermediate regime from convective to conductive is clearly subcritical [37]. Due to this, most of the plots imply the evaluation of the Y parameter which represents the relationship between yield stress and the buoyancy contribution. As it is evident, the critical Y_c is not as carefully reviewed due to the fact that the boundary conditions, which largely affect this parameter, are mostly different. The investigation has been performed for a square cavity geometry being all the components of velocity 0 in the walls in order to account for the convective-conductive effects. As it has been demonstrated in [38], the steady state is not influenced by the transient hence the simulation is set up in this mode. The Boussinesq approach is definitely used and equations are non-dimensionalized in order to run a parametric study. The results are validated with [39].

1. Introduction

As the Reynold-Bénard instability takes place when buoyancy surpasses the effects of viscosity and thermal dissipation, the slope of the critical Rayleigh is evaluated against the Bingham number. Ra_c is shown to be proportional to Bn and Pr (Prandtl number), hence the stabilization effects of Casson-type fluids. Then, the velocity contours, temperature and heat transfer -this last through the Nusselt number- have been analyzed. The results are consistent with what has been detailed so far. As additional outcomes, the non-linearity trait of temperature is certainly proportional to the Rayleigh number. The Nusselt number equally decreases by increasing the Bingham number as a result of the stabilizing effect of the yield stress. The transition regime, in the other hand, is abrupt when passing from convection to conduction when the Nu is plotted, which is consistent with [37]. Furthermore, even though a variation of the Pr number will not entail any noticeable change for Newtonian flows, for Casson-type flows it will be inversely proportional to the heat transfer. In comparison with other literature, the Casson model yields the lowest heat-transfer rate.

Moreover, in [40] the geometry of a square-cavity with a copper foil "partition" located in the middle is studied without inlet and outlet conditions. There are thence 4 walls, as the confined magnetic fluid - alkyl-naphthalene - is warmed by the lower wall and cooled in the upper: motivating an ascending convection flow. The side walls are considered and set up as adiabatic. This geometry is numerically tested with and without the action of a strong magnetic field with maximum magnetic field intensity H_0 . In order to account for the heat transfer, the Nusselt and Rayleigh numbers are evaluated and even a new Rayleigh magnetic parameter is defined to yield for the magneto-caloric convective term so that $Ra = \frac{\mu_0 H_0 M_s h^2}{\kappa \eta}$; where μ_0 is the magnetic susceptibility, h the height of the channel, κ the thermal diffusivity and η the viscosity with 0 magnetic field. The difference noted in the application of the strong magnetic field is evident in two manners: when it is not present, the flow shows 4 vortical structures formed next to the corners of the copper foil. However, when the magnetic field is switched on, only the two upper remain. Logically, the temperature field is highly perturbed by this phenomenon as plots show. On the other hand, when the heat transfer is evaluated, it is perceived that it is mitigated for low Rayleigh numbers ($Ra \leq 5000$) but interestingly is then enhanced for ($Ra > 5000$). This effect is a consequence of the fact that the buoyancy and magnetic body force have opposing nature, being the buoyancy predominant in low Ra . However, when it is highly increased, the magnetic force becomes the main effect due to the higher magnetization motivated at the same time by higher temperature gradient, hence the heat transfer is strongly boosted.

1. Introduction

1.2.5 Non-Newtonian Models

Blood flows exhibit, especially for low shear rates, a shear-thinning behaviour. This means that, when forces or stresses are applied to the fluid, it demonstrates more tendency to flow and to have consequently less contribution of the viscous term. This nature, when viscosity cannot be assumed as constant such as in classic Newtonian, is properly described with Non-Newtonian behaviours. Fortunately, for blood and other shear-thinning fluids, science has developed a large variety of models which could success in describing and predicting the blood flow. This is why, those models will be carefully reviewed and the most promising ones will be evaluated in this document.

Interestingly enough, recent investigations, using the analysis of a C-T developed aorta geometry and by simulating a pulsatile flow emulating the systole-diastole cycle, recognize a correlation between the Wall Shear Stress (WSS) in the aorta with sensitivity to suffer from different diseases. A solid example of it is the proven development of atherosclerotic plaques in blood flow as a result of the "oscillatory" and low WSS distribution. As it has been said, the way of modelling blood will have an evident impact on the solution achieved computationally. Whilst there's a difference of opinions regarding the Newtonian or Non-Newtonian approaches which is actually still remarkable, Karimi et al [13] tries to demonstrate the effects of the different Non-Newtonian models in the aorta geometry and compare them with experimental data. In their investigation, the 3-D aorta mesh is obtained by using C-T imaging from a healthy patient, and the CAD model results from the union of 992 cross-sectional tomography. Then, they describe the usual governing equations in which surprisingly, the gravitational contribution is not considered even though its effect may be appreciable.

Afterwards, some ideas of the 9 Non-Newtonian models to compare (Power-Law, Generalized Power-Law, Modified Power-Law, Carreau, Carreau-Yasuda, Cross, Casson, K-L and Modified Casson) are provided along with the values of their parameters in order to model the blood shear-thinning behaviour. Once simulated, the first evident conclusion obtained by Karimi et al is the inaccuracy demonstrated by the Cross model instead of the other models investigated, which deployed alike tendencies. Moreover, the greatest deviation is noticed in the diastole point, whilst in the systole regime differences are not so easily noted. Even though the Newtonian approach is widely used for simplicity and might suppose a valid approach in several cases, it systematically underpredicts WSS specially when it moves towards low ranges, this effect might be critical when stenosis is present. Furthermore, the systole-diastole inlet velocity function demonstrates a significant effect on the shear-thinning behaviour of blood. This is why some Non-Newtonian parameters should be further improved. Thus, current Non-Newtonian models are not able to describe the thixotropy effects hence, the authors of this publication, strongly encourage the

1. Introduction

enhancement of its modelling in order to run more accurate studies.

Even though the existence of blood experimental investigations is unfortunately scarce and thus the impossibility to prove interesting models and conjectures made during the last decades, several experimental investigations have been made for different fluids which might show similar traits. One example of it is the Carbopol study carried out by [41] where this non-newtonian shear-thinning fluid is thoroughly evaluated under Rayleigh-Bénard stability convection. Previous analytical work has been developed and will be set into prove with the experimental results from this paper. For instance, in [42] they used the simulation of the Carreau-Bird non-newtonian to achieve the conclusion that, even though the onset of the convection will remain equal than a Newtonian case, the roll pattern of the convective instability can form hexagons or even squares as well. Furthermore, they state the fact that depending on the shear-thinning magnitude of the fluid, the bifurcation formed can turn out to be subcritical. This last trait has been more carefully reviewed by [43] where it is demonstrated the most likely phenomenological bifurcation to take place is the supercritical bifurcation, as this paper from [41] will then reveal. Besides, Liang et al conclude that the buoyancy patterns formed are similar than for the Newtonian case, since the main difference is the increase of the Nusselt number. Here, in [41], a step forward is carried out by considering that the non-newtonian nature will trigger the convective instability once the stresses due to buoyancy overpass the yield stress of the fluid. Therefore, as it is required, the viscous characteristic time will be substituted by a characteristic time dependant on the fluid microstructure. This will redund in the modification of the Rayleigh effective number so that $Ra = \frac{\alpha\beta\Delta T g H}{\tau_y} \frac{t_d}{t_{microstructure}}$ which will be logically greater than the critical rayleig Ra_c .

The fluid is experimentally evaluated in a rectangular channel of dimensions (Length x Widht x Height)= (386 mm x 186 mm x 20 mm). In order to set up the buoyancy, the bottom plate is heated with a resistance and direct current so that $P \simeq I \cdot R^2$ where $R= 25.5 \Omega$. On the other hand, the upper plate is cooled down using a heat exchanger. It must be said that, even though only the steady-state solution is considered, two main transient modes will take place in the experiment. The first one will call for the Fourier-Conduction nature with the expression: $\Delta T = \Delta T_{max} \left(1 - e^{-\frac{t_0-t}{t_d}} \right)$. The other one will correspond to the Landau stability theory: $\Delta T = \Delta T_\infty + De^{-\frac{2t}{t_c}}$, where specially the characteristic time t_c will be the responsible and control parameter of the non-linear convective rolls apparition.

Moving forward to the result analysis, the first result to notice is the difference of the heat transfer mechanism dependant on the power provided to the inferior plate. When a first "Newtonian-like" fluid, glycerine, is examined, at a critical power $P_c = 16.32W$ the heat transfer passes abruptly from being mainly conductive to convective. Furthermore, relating to the Rayleigh theoretical assumption, this critical Rayleigh turns to be $Ra \simeq$

1. Introduction

1774, which is approximately the theoretical value established at $\text{Ra} = 1708$. The velocity amplitude for the onset of the convective flow will be determined by the law of imperfect bifurcations estimated by Landau so that $P_r - aV^3 + h = 0$. Additionally, in the contrary with what some publications state, here the convection stability is triggered without the action of any perturbation. The transition to the Rayleigh-Bénard convection instability is similar to the Newtonian case in the sense that no hysteresis is present and that no discontinuities take place either. As Liang et al [43] proclaimed, the bifurcation is directly super-critical and is followed by a slow-down regime. Hence, it can be described and predicted with Landau's theory as well. Furthermore, in consonance with what was explained on the critical Rayleigh number, it is revealed that it primarily depends on the yield stress state, which is at the same time characterized by the yield number. The stability will be clearly non-linear in contrast with what [44] state -they argue that the linear stability is enough to describe the problem-. Regarding all these findings, the authors conclude -with the carbopol experimental analysis- with three main ideas: the convective instability patterns can be obtained by modifying the heat flux in consonance with the imperfect bifurcation. This last can be predicted by using Landau's theory. In the slow-down regime, practically the same results have been obtained that in the Newtonian case. Finally, the last idea to tread lightly is the great dependency of the Rayleigh critical number on the yield stress, which can make it vary in even three orders of magnitude, which reveals the importance of considering the elastic energy due to the microstructure in spite of the classical "viscous terms" assumption. In this sense, the solid-fluid transition is coupled and this is why the authors of this document encourage future publications to investigate the coexistence between solid and liquid phases in the convective onset.

1.2.6 Multiphase Flow

Blood, as it is detailed in most of the medical encyclopedia and biology - biochemistry literature, is composed by different components therefore it is completely homogeneous. What is more, the components even react different to forces, therefore the need of properly modelling the blood with its real complexity and the consideration of the main elements. Most of times, in hemodynamics, two phases (given their majority concentration in the blood flow) are modelled: the plasma layer and the red blood cells. However, when FHD and MHD contributions are studied, they might not be enough since the charged proteins that travel suspended in plasma have much to say. This is why, the implementation of the FHD-MHD monophase investigation with the multiphase hemodynamics is a pending exercise in which the author of this document has special interest to perform after this thesis defense.

The multiphase representation of the blood has been usually limited to two phases: a

1. Introduction

plasma layer surrounding a red blood cell layer. Actually, experimental investigations suggest the accuracy of this supposition. One of the most referenced publications in which a bi-phase model for the blood flow is developed is the work from (Sharan, Popel; 2000) in [45]. In it, the Fahraeus effect, Fahraeus-Lindqvist effect , the existence of a cell free layer in the vicinities of the boundary, the blunt velocity profile and the phase separation effects are carefully considered due to the different components conforming the blood flow. Sharan and Popel first assume that the shear rates in which the blood flow is involved is high enough to consider both phases: the hematocrit and the surrounding plasma layer as Newtonian, immiscible between them, and with a discontinuity of viscosity in their interface. The geometry considered will be a cylindrical tube. The mathematical derivation of the flow using the Poiseuille velocity scope is obtained and the relationship between the hematocrits (core hematocrit and discharge hematocrit) is calculated. From this balance, it is seen that the core hematocrit must be evidently larger than the discharge in order to satisfy the logical fact that the tube diameter must be larger than the core diameter. Equally, the derivation for the relationship of the maximum velocity against the averaged and the WSS (Wall Shear Stress) are obtained. This model has been closure by using empirical data obtained in experimental investigations, such as the Discharge/ Core Hematocrit balance function from [46], but also the relative apparent blood viscosity and in bulk. Results are in consonance with both theoretical and empirical investigations and evidence the fact that the thickness of the cell-free layer decreases as the RBC concentration in volume increases. The effective viscosity of the outer layer is also found to be proportional to the hematocrit. Another interesting trait observed is the fact that the velocity profile acquires more bluntness as the tube diameter increases or hematocrit decreases. Authors finish their work stating the fact that the continuous case consider abruptly fails when the size of the tube diameter is approximately the same than the red blood cells, where discrete models are necessarily used such as the micropolar fluids models.

The same idea has been investigated in [47], even though they state the necessity of using the Non-Newtonian approach for small vessels (less than 300 μm), whilst for larger, the Newtonian model is enough to describe the blood flow. The same effects described in the previous publication [45] (fahraeus, fahraeus-lindqvist, plasma layer without erythrocyte concentration next to the wall, and blunt velocity profile) observed in vitro and in vivo experiments suppose challenging in terms of mathematically describing them and hence the multiphase is indeed required. The enhancement made to the Sharan and Popel model is the viscosity function depending on the hematocrit concentration instead of assuming it as constant. By using the Einstein's formula, the effective viscosity is known to be : $\eta = \frac{\mu}{\mu_1} + nm_2$. In order to obtain the nm_2 parameter, an empirical dependence is used.

1. Introduction

With this approach, better results have been respectively obtain and a further step has been done in order to ensure a generalized theory. It must be said that the blunter velocity profile comparing to the pure parabolic Poiseuille flow has been achieved, but also the dependency of the hematocrit on the vessel diameter, the cell-free plasma layer and having the blood viscosity as a function of the vessel radius.

An interesting publication which deals, at the same time, with multiphase and Rayleigh-Bénard convection is [32]. The aim of this publication is to have a more rigorous and mathematically correct model of the effects, since most of investigations regarding this topic do not consider phenomenological laws and mixture theory and consequently incur in the binary Soret effect. This trait is specially critical considering that the nanoparticles strongly affect the viscosity, thermal conductivity and many other flow variables. This is why Siddehwar et al implement this missing considerations. Besides, they follow the nanoparticles-base liquid multiphase mechanics proposed by [48]. The study of [49] and [50] using Buongiorno's model demonstrated that Brownian motion and thermophoresis effect are negligible in most of the cases. Hence, the purpose of Siddehwar is to provide a better model to account for the enhanced heat transfer of nanoliquids yet also achieve the correct boundary treatment given the Nield and Kuztnesov studies from [51]. First, the equations are derived and the phenomenological laws and mixture theory implemented, assuminf isothermal and isoconcentration boundary conditions. Afterwards, the linear and non-linear weak stability of the problem is analyzed in order to establish the regimes for the convection Rayleigh-Bénard instability. The Nield and Kuztsenov BC treatment is considered. Once achieved the mathematical model, up to 20 nanoparticle liquids are simulated and evaluated in which the blood is not present. As a first evident result, the heat transfer enhancement is shown to be strongly dependent on the Brownian effect coupled with the thermophoresis when laminar flows are studied. Nonetheless, when the turbulent case is reviewed, it has been shown that the thermophoresis does exclusively have an impact on the onset of the Rayleigh-Bénard convection and in heat transfer. If this effect is not considered, the previous Soret effect is obtained and as stated it is not a decent approach. Furthermore, it has been noted that for all the 20 nanoliquids, subcritical instabilities have been achieved. Moreover, the Nield-Kutzsenov boundary treatment has been implemented and demonstrated its suitability and adequacy to model the problem. What has been also surprising is the fact that 10 % of volume proportion of nanoparticles have exactly the same effects than 6% thence this last case has been the one studied due to its computation relative simplicity. In comparison with other publications, where the Brinkman model is adopted for viscosity model ant Hamilton-Crosser for thermal conductivity, the mixture theory and phenomenological laws demonstrated great consistence and power to predict the nanoliquid flow. This last idea should be further

1. Introduction

reviewed by running experimental results regarding the convection of nanoliquids, since the advantages of using single-phase or multi-phase flow models has not been still clearly established.

1.2.7 Applications of similar investigations

The principles of Tzitzilakis in [12] have been further supported by Reddy et al in [8] with the interest of giving detail of Tzirtzilakis assumptions with clear evidences but without creating an extense publication such as the reference text from Rosensweig at [9]. Besides, their extense literature review provided practical information of up-to-date investigations dealing with MHD and FHD of bio-fluids, including multiphase and even heat transfer optimixation in which the Rayleigh-Bénard convection aimed at our investigation should attend. These research documents are specially represented by the two [52] and [40] suggested by Reddy et al. In those works, the interesting trait of the convection attributes dependency on the angle formed between the temperature gradient and the magnetic field is evidenced. Furthermore, in [53] numerical simulations testing the magnetic convection are carried out on different geometries. Interesting enough, the same magnetoviscous term introduced by Tzirakis in [18] has been modelled in [54]. It must be said that an important error is displayed in Reddy et al in the explanation of Hemoglobin: it does not carry forms of iron oxides, its nucleus is not merely iron, since it is an ion of Fe^{2+} . Hence, they should not refer to oxides but ions. This correction is consistent with the biochemical extense description of [6] and [7]. The magnetostatic field influence and Boussinessq approach similarly seen in all the literature surveys are here derived as well. Additionally, an insight of the Brinkman Equations where porous media is considered is also provided in this document.

Another evident application of the FHD/MHD effects is the guidance of magnetic particles along the bloodstream in order to deliver medicines in a localized region, incurring in more effectiveness and in less presence of secondary effects. This methodology is known as Magnetic Drug targeting, it has been reportedly investigated in the last 2 decades and is even commonly used in recent medical operations where in mot of times localized cancers is treated. Results by now support the effectiveness of this method. A really interesting reserch upon this field has been the simulation carried out by (Cherry, Eaton; 2013) in [55]. As they point out, one of the major problems is the model of viscosity, being one of the approaches through bi-phase hemodynamics, supposing plasma to be Newtonian and and the RBC flow in the middle as strongly Non-Newtonian. Another valid approach seen in literature is the use of statistical models that will describe the collisions between the individual cells in the bloodstream. Finally, a continuous shear-dependent viscosity model such as the Olroyd-B model from [56] can be also specially useful when results with

1. Introduction

smooth velocity profiles are aimed without implying an excessive computational costs. In this last case, the viscosity fit expression derived known as the Brooks viscosity function [57] is usually invoked. In the work of cherry, three models are examined: the viscosity model from Brooks et al, the bulk magnetization force known as the FHD effect together with inter-particle magnetization coupling from [58] and the particle dispersion model using the Direct Monte Carlo simulation. The geometry employed is a straight cylindrical artery and with the simulations it is intended to know more about the optimal results for cluster size, concentration of magnetic particles and shape. The first evident result is the perturbation of the normal blood flow when these magnetic clusters are introduced. Then, varied results are obtained depending on the medical treatment. If the MDT is aimed for a short period, the optimal solution is the use of high AR, low volume and low concentration clusters, whilst for long period the opposite values show a proper effect. However, it must be said that the results of these investigations are not as encouraging as expected as, in the best case scenario, the model predicted that only a 20 % of the original concentration of medicine magnetic clusters will remain in the localized position after an averaged residence time of 10s.

Regarding the optimization of the MDT technique, the work from [59] provides a genuinely shaped focused magnet that is able to enhance the technique and guide the magnetic drug with more percentage of success to the desired location, but also by giving more depth than the MDT equipment used by 2011. This principle is specially awarding in terms of non-invasive, as the success of chemotherapy depends on the delivery of the drug and to the fact that it is not lost significantly in the blood flow as they entail a toxicity hazard for healthy tissue. The work from the authors relies on the numerical model developed by Voltairas et al in [60], but suppose an improvement since their results show that the magnetic field is not large enough to work with deep positions in the human body. In the end, the focused magnet from [59] is conformed by 36 pyramidal prisms which allows the correct use in 2.5 to 3 cm deeper heights.

The Non-Newtonian Effect is carefully reviewed when the coronary arteries are simulated in [61]. In it, the first requirement imposed is the necessity to run the simulation of all the arterial network in order to obtain trustworthy results. The results of the flow upwards and downwards the examined artery geometry should be appropriately implemented as boundary conditions. This idea has been efficiently carried out by [62], allowing the implementation of network outlet BCs in commercial CFD packaged. However, the geometry tested was too simple to describe and did not consider curvature neither results did fully converge either. With the present work, one secondary purpose is the acceleration of converged results through the Shanks algorithm, which consider time-depending outlet

1. Introduction

conditions. Several steps have been done in order to improve the artery geometry as well. The Non-Newtonian model chosen has been the Casson, as in many literature it has been stated as the most appropriated for blood flow shear-thinning representation. The flow will use the velocity profile from the Poiseouille problem in each of the vessels. Interestingly enough, Apostolidis et al also present some of the failures conducted in the CFD research community when conducting a convergence study, as the pulsatile nature of blood, mesh density, integration time step are infrequently attended. This is why, they will be considered in this study. It has been noted that the non-linearities introduced by the Casson model imply the further refinement in both spatial and time dimensions as they struggle the convergence of the solution. Evidently, results largely vary with the systole-diastole cycle, as Casson model can display a difference in the results up to a 50 % with the Newtonian case. Authors conclude the achievement of their purpose with validated and verified results, which are in good agreement with similar publications and with logic dictates.

On the other hand, the motivation of Tanghient et al in [52], different to the wide variety of Magnetic Drug Targeting studies, is to increase the efficiency of motors by including magnetic particles in the oil and make it act as a ferrofluid, since contemporary publications suggest an increment of the heat transfer when magnetic fields are applied. An initial simulation is performed and their results are commented to bring more light in this matter. The equations they used to describe the flow problem come from [23]. In the contrary of what [63] obtained, a significant effect and heat transfer enhancement is perceived. Without the action of the magnetic field, only one main re-circulation zone is depicted due to the action of the gravity field, whilst the magnetic field adds one more with strong character. Besides, the velocity contours are primarily induced by the magnetic field, since they remain barely equal when the gravity contribution is disabled.

1.3 Structure of the M.Sc. Thesis

The scheme of the thesis will follow an logical order in which we will depart from the basics and general ideas and will get into the specific and detailed traits. As it can be seen, the literature survey which helped us to understand in which stage of investigation is currently located the scientific society and which approaches have been followed has been already detailed.

Now, the governing equations of the flow mechanics and electrodynamics will be briefly explained. Blood, which will be the fluid investigated, will be described by giving special attention to its structures with special sensitivity to magnetic fields and that will consequently affect the blood flow. Given this explanation, the magneto and ferrohydrodynamic will

1. Introduction

be derived and included in the Navier-Stokes equations. Then, one of the main elements to consider, the Rayleigh-Bénard Convective instability, will be also explained and incorporated in the investigation, specially paying attention to the magnetocaloric heat contribution in the energy equation. Then, the non-newtonian models estimated useful to model the shear-thinning behaviour of the blood will be presented, giving also a brief explanation of the multiphase hemodynamics and the subsequent effects noted on blood flow.

The following Methodology section will describe the computational framework, the numerical setup, the models chosen, the algorithms that will be used and the geometries that will be investigated and simulated by using ANSYS package.

The results from this simulations, starting by a validation benchmark problem from [1] will be conveniently described and detailed and the solid conclusions from them will be withdrawn in its corresponding section. They will contain the evaluation of different Non-Newtonian Models, Magnetoviscous additional contributions, high fidelity in-house pulsatile velocity inlet and Rayleigh-Bénard Instability will be provided.

Any additional contribution interesting but non essential to the reader, such as convergence plots and codes developed, will be annexed to the appendix section.

Chapter 2

Theory fundamentals

2.1 Flow Mechanics and Maxwell Governing Equations

The study of the motion of the blood along the different geometries we find in a human body: arteries, veins, vessels, capillaries will undoubtedly require the evaluation of the Fluid Dynamics equations of this precise bio-fluid. Besides, considering the fact that the purpose of this investigation is to determine the influence of different electrostatic and magnetic fields to the blood, several source terms representing the influence of this fields will be consequently added to the momentum and energy equations of the flow motion. We will always consider the evaluation of the flow variables over a differential volume control, making use of the Reynolds Transport Equation to establish the dependencies of the total derivatives of variables with their non-stationary and convective contributions. Here, we will present the 3 main equations of the Fluid Dynamics which are commonly known as Navier-Stokes equations, which will impose the conservation of mass, momentum and energy along the control volume specified.

2.1.1 Navier-Stokes Continuity equation

The mass cannot be created or destroyed along the specified domain, it is one of the most solid principles of the classic physics. Equally, in fluid mechanics, we will make use of the intensive variable density ρ which relates mass per volume, which will be specially useful for the integration calculus.

$$\frac{D\rho}{Dt} = 0 \rightarrow \frac{\partial \rho}{\partial t} + \nabla \cdot (\rho v) = 0 \quad (2.1)$$

As it has been said, the Reynolds Transport equation has been used to relate the total derivative of ρ with its non-stationary and convective term. Now, regarding the fact that

2. Theory fundamentals

blood is considered to be an incompressible fluid in liquid stated which is moving at velocities $M < 0.24$, the incompressible constraint can be imposed and will reduce the expression 2.1 into:

$$\nabla \cdot v = 0 \quad (2.2)$$

2.1.2 Navier-Stokes Momentum equation

When the speed of the flow varies throughout a control volume (both in space and time), it is because forces act on it that entail its acceleration and the velocity convection, being the variation of pressure the most relevant term in flow dynamics. We must not lose sight of the fact that, despite we are probably facing the most hostile equation in classical physics, we are merely applying Newton's 2nd Law to the blood flow.

By imposing this principle on a fluid volume, on the one hand we will have the total derivative of the velocity multiplied by the intensive volumetric variable density, and on the other hand of equality, the contribution of the forces (mass in which the gravitational effects and inertial forces, pressures stress terms, viscosity contribution). Here is where the forces will be supplemented with the ferro- and magneto-hydrodynamic momentum source terms that will -by now- be modelled and represented with the variable $f_{Maxwell}$.

$$\rho \frac{\partial v}{\partial t} + \rho v \cdot (\nabla \otimes v) = \rho f_m - \nabla p + \nabla \underline{\tau} + f_{Maxwell} \quad (2.3)$$

Where τ stands for the viscous stress tensor and will depend on the features of the fluid (Newtonian or Non-Newtonian formulation) while the $f_{Maxwell}$ term gathers both FHD and MHD contributions that will be derived from the Maxwell Laws. It is important to remark that this equation is a vectorial expression and hence 3 coordinate equations (e.g. in x-axis, y-axis and z-axis given a Cartesian Coordinate System) derive from it depending on the coordinate system .

2.1.3 Navier-Stokes Energy Equation

If this previous equation 2.3 is multiplied vectorially by the velocity, the mechanic energy equation is obtained. If we couple the internal energy equation with the mechanic energy equation, the total energy equation (scalar) will be derived.

$$\rho \frac{D}{Dt} (e + v^2/2) = \rho \dot{q} + k \Delta T - \nabla(v \cdot p) + \underline{\tau} : (\nabla \otimes v) + q_{Maxwell} \quad (2.4)$$

In which the LHS shows the total derivative of the internal energy (which depends on temperature) and velocity component, and the right hand side expresses the heat fluxes

2. Theory fundamentals

along the control volume. The first term $\rho \dot{q}$ indicates the introduction of a determined heat source, $k\Delta T$ is the Fourier's Conduction Law, and $\nabla(v \cdot p) + \underline{\tau} : (\nabla \otimes v)$ are the pressure and viscous stress dissipation terms. Finally, the $q_{Maxwell}$ will be the contribution of the FHD and MHD effects through the Magnetocaloric effect and Joule Effect as it will be seen in the following lines.

2.1.4 Maxwell Governing Equations

The influence of the magnetic and electric fields perturbing the blood flow will rely on the electrodynamic principles known as the Maxwell Laws [15]. The immense merit of Maxwell's work is known by the unification and mathematical formulation of the electrodynamic laws derived from relevant physicists (Coulomb, Faraday, Ampère, Gauss) into a set of 20 original equations which contain the principles of non-stationary electric and magnetic fields and the dependence between them. Later on, a review of these laws made by Heaviside and Gibbs, reduced its number into 4 main laws, which can be supplemented by other constitutive equations. They, in conjunction with the Ohm's Law -which is going to be represented with the last of the following equations- will be the responsible for the FHD and MHD source and dissipation terms added to the Navier-Stokes Momentum and Energy equations.

$$\begin{aligned}\nabla \cdot D &= \rho_e \\ \nabla \cdot B &= 0 \\ \nabla \times E &= -\frac{\partial B}{\partial t} \\ \nabla \times H &= J + \frac{\partial D}{\partial t} \\ J &= \sigma(E + (v \times B))\end{aligned}\tag{2.5}$$

The first equation is known as the Gauss' Law, and introduces the dependency of the spatial variation of electric flux density (D) with the charge density (ρ_e) contained in the field. Afterwards, the Magnetic Gauss Law follows and represents the impossibility of the existence of a magnetic mono-pole: the magnetic field flux over a closed surface is 0, it does not diverge, as its poles represent the field closed lines, therefore, the spatial variation of the magnetic flux density or magnetic induction variable (B) is logically null. Then, the 3rd equation implies the mathematical formulation of the Faraday-Lenz, in which the existence of a magnetic force implies the creation of a non-steady electric flux opposing it (Lenz's contribution) and vice-versa. This principle led to the creation of electric motors, which are a strong evidence of this simple law.

Finally, the Ampere's Law complements the preceding statement and postulates that the

2. Theory fundamentals

origin of a magnetic static field is a consequence of a stationary electric current, which is at the same time related with the volumetric flux variable J of the Ohm's Law from 2.5.

2.2 Blood Composition and Rheology

Blood is considered to be the principal yet equally the most complex bio-fluid present in animals and consequently in human beings. A large list of its duties has been reported, in which the transportation of fundamental molecules, heat regulation, pH control and immune response may be the most evident tasks in which blood is the main responsible. Another important aspect to consider is the extreme complexity of the infrastructure of veins, arteries and vessels in which blood travels and indeed largely affects its flow. Hence the challenging of acquiring full-body simulations with reliable predictions, so that investigations of small sections in all the scales are required in order to account for the most representative phenomena description in each and then the addition of all these small steps give a complex and accurate idea of the real problem.

As it can be perceivable, the blood composition will grossly characterize its properties and behaviour regarding the flow dynamic equations but also its response to different scenarios, perturbations and sources such as the electromagnetic fields that will be carefully reviewed. Blood, in a simplified classification, consists of blood cells and plasma.

2.2.1 Blood Cells

This group stands for three main elements: platelets, white cells and red blood cells. The first two will be briefly commented as, according to , their concentration, volume and effect on the overall blood flow induced with a magnetic static field will be negligible compared to the RBCs.

- **Platelets or thrombocytes**, in the strict sense, are not considered as cells as they are irregularly-shaped cellular fragments that generally do not possess any nucleus. Their diameter -even though is difficult to be measured- is approximately between 2 and 4 μm , and its concentration is about $1500\text{-}4000 \cdot 10^9$ platelets per litre [7]. Their main functionality is the hemorrhage protection and control, acting similarly as a patch or shield. This behaviour will prevent plasma from leaving the conduct.
- **White Blood Cells or leukocytes** are approximately 10 times bigger than red blood cells [6] however their small concentration in blood ($4 \sim 10 \cdot 10^9$ units/l) shows their little contribution to the flow behaviour. Their main role is the protection against invasive microorganisms and inflammatory processes. With the process known as

2. Theory fundamentals

diapadesis [7] they are able to pass through the capillary walls and penetrate in the tissue they are required. At the same time, basind on the characteristics of the cells and actions to carry out, theu can be divided into granulocytes, monocytes and lymphocytes.

- Finally, the **Red Blood Cells or erythrocytes** are the most numerous cell type in the blood, with a concentration of $4.6\text{--}6.5 \cdot 10^{12} / \text{L}$. Similarly, the percentage of volume occupied by RBCs of the total fluid is known as hematocrit, which is averaged with 0.47 or 47 % but not definitely constant as it will be seen. Interestingly enough, the diameter of these disk-shaped cells is approximately $7\text{--}8 \mu\text{m}$, however their flexibility allows them to travel through capillars of even smaller diameter. The main role done by RBCs is the transportation of O_2 and CO_2 gases throughout the whole body.

The principal component of erythrocytes is the hemoglobin protein, which is detailed in the following image (Figure 2.1).

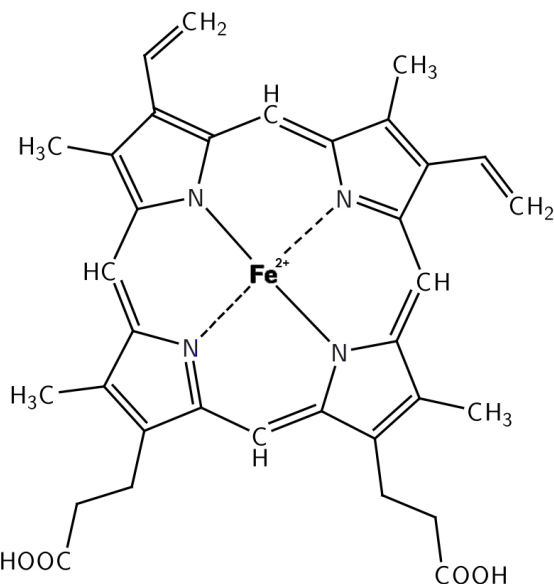


Figure 2.1: Chemical formulation of Hemoglobin

The nucleus of the protein presents Fe^{2+} ions that will logically introduce polarization to the cell and will therefore provide electric and magnetic susceptibility to the haematocrit and to the total flow. This feature, along with the mineral salts and charged proteins of the plasma, will haul the FHD and MHD contributions in the Fluid Mechanics of the blood flow.

2. Theory fundamentals

2.2.2 Blood Plasma

As it has been introduced, plasma is a bio-fluid liquid in which blood cells, mineral salts, glucose, ions and proteins are found in suspension. It is made up by a 95% rate by water and in terms of blood volume it constitutes a 54% of the total [6]. The presence of ions and charged proteins will introduce conductivity and magnetic susceptibility to this component, thus, the blood motion will clearly be notoriously affected in the presence of magneto-static and electric fields. A similar behaviour has been described in the RBCs as a result of the hemoglobin's Fe^{2+} ion nucleus.

- In terms of the **ionic constituents**, the most present is sodium ion, followed by chloride, potassium, magnesium, phosphates, sulfates and other minority ions.
- Plasma proteins will also introduce charged elements, and they contribute with a 7-9% of plasma's volume. Albumin is probably (with approximately a 56% of protein percentage [7]) the predominant component, whose functionality is the transport of lipids, steroids and osmotic pressure regulation. As experimental studies reveal, they are charged proteins. Similarly, globulins are present with almost a 40 % of protein's wage, which equally carry vitamins and lipids throughout the whole circulatory system. Finally, in a significantly less rate, fibrinogens (up to a 4%) will play an important role in blood coagulation processes.

The detailed description of the blood components has been significantly important to remark the need of considering FHD and MHD effects when electric and magnetic field sources are proximate to the analyzed blood flow. Another interesting aspect would be the success of implementing those both theories with multi-phase hemodynamics, which would clearly entail a more accurate approach to the real blood flow. Both ideas have not successfully found any common point yet their purpose remains the same: to represent with reliability and detail the blood flow under different geometries and scenarios.

Another important trait of the blood is the analysis of its rheology. The Non-Newtonian behaviour noted in blood experimental research [14], specially considerable at low shear rates. In the branch of Non-Newtonian flows, it is classified into the shear-thinning subgroup, id est, the viscous term of the Navier-Stokes equations has less influence as shear strain evolves. It is a consequence of two general motions noted: the Brownian movement in which the RBC particles show a randomized time and spatial evolution, whilst the second one is the tendency of the flow to orient these particles into streamlines following the highest axis (normally expressed as the x axis). Whilst the first behaviour entails an increasing effective viscosity, the second one is more notorious and will incur in the opposite result, therefore blood will acquire the shear-thinning feature. In the other hand, Newtonian flows assume constant dynamic viscosity μ and totally independent of

2. Theory fundamentals

the flow rate. Therefore, it will be important to consider and evaluate Non-Newtonian Flow models in order to accurately predict the blood motion, and compare the results with experimental data available [13].

2.3 FHD/ MHD approach

The first effect of the above explained that will be reviewed will be the sensitivity of the blood flow to external electric and magnetic fields. Thus, FHD/MHD formulation tries to account for the electrodynamic effects that do take place for a conductive flow.

Their contribution will result in the coupling of the Maxwell Laws with the Momentum and Energy Equations of Flow Mechanics.

2.3.1 Magnetohydrodynamic Effect (MHD)

The Magnetohydrodynamic behaviour was firstly described by [11]. The purpose of this mathematical development aimed to increase the accuracy and understanding of the Solar ferromagnetic flow and its respective waves. Nonetheless, the same principle can be applied for the most important bio-magnetic fluid -blood- as a main consequence of the iron ion (Fe^{+2}) that are located in the centre of the hemoglobin protein, the most important component of erythrocytes or Red Blood Cells.

MHD will develop its formulation by assuming that the polarization and magnetization effects (FHD) do not take place in the flow or are negligible. As it is considered to be a magnetized and polarized particle, and hence the blood is assumed to be conductive, its influence along a magnetic field will redound in the creation of electromagnetic force regarding the effect of a moving particle with electric charge inside a magnetic field.

The main contribution of the magneto-hydrodynamic effect is the inclusion of the Lorentz force in the momentum equations and hence its corresponding dissipation term in the energy equation.

$$f_{MHD} = f_L = q(E + v \times B) = J \times B \quad (2.6)$$

which, according to the Maxwell Law can be equally expressed with the volumetric current density J by using the Generalized Ohm's Law:

$$J = \sigma(E + v \times B) \quad (2.7)$$

, hence,

$$f_{MHD} = \sigma(E + v \times B) \times B \quad (2.8)$$

2. Theory fundamentals

The vectorial math derivation component-by-component is straight-forward and will be derived in the following sections.

It must be said that the most of the publications reviewed in this thesis upon blood numerical modelling have neglected the electric field due to the predominance of the magnetic field ($E \approx 0$). Hence, under this assumption, the contribution of the magnetohydrodynamic source effect can be reduced to:

$$f_{MHD} = \sigma(v \times B) \times B \quad (2.9)$$

2.3.2 Ferro-hydrodynamic Effect (FHD)

The ferro-hydrodynamic contribution stands for mathematically modelling the polarization forces and energy dissipation that takes place between existent particles.

Even though these effects have been described over the last century with great detail [9], it was not applied for medical purposes until Haik et al realized that the blood showed particular reaction to external magnetic static fields and hence could be studied under the same principles. This is how the branch of bio-magnetic fluid dynamics was created in the publication [10], even though their equations are inherited from ferrohydrodynamics. The big difference it yields with the MHD, is that the environment must not be necessarily conductive. As it has been stated in [12] the iron ion (Fe^{+2}) that are located in the centre of the hemoglobin protein, the most important component of erythrocytes or Red Blood Cells, get polarized and oriented as a result of the action of the external field. The Magnetization of these will remain as the main effect of the external forces. Therefore, from equation (ref) the magnetization parameter (M) will be studied and set as the predominant in the equation. The mathematical modelling of M is not easy to be set as it has shown , at the same time, great dependency of the magnetic field intensity (H) and of the temperature (T) so that $M=M(H,T)$.

Several attempts have been made to derive closure expressions that trustworthy represent the behaviour of the clearly non-linear magnetization. In order to achieve so, non-linear regression equations are derived from magnetization curves or hysteresis of the experimental results by comparing the dependency of both variables. An example of it is the following illustration from [3].

2. Theory fundamentals

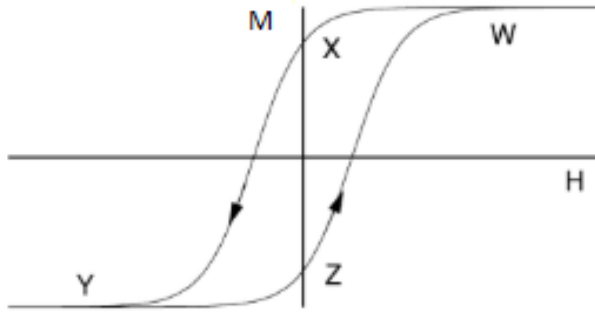


Figure 2.2: Typical hysteresis -or magnetization- curve (M against H) for a ferrofluid.
Source: [3]

The points W and Y indicated in the plot represent the stage where the material gets magnetized, while X and Z describe the residual magnetization present in the core even though $H=0$. Besides, the intermediate area beneath both As it can be perceived the main region of the slope appears to be quasi-linear and hence the following equation known as the linear equation of state, can be assumed for weak fields:

$$M = KH(T_c - T) \quad (2.10)$$

where K is a constant (the pyromagnetic coefficient), and T_c the Curie temperature, which corresponds to the temperature in which the material loses its ability to magnetize, or saturates (points W and Y) -turning its behaviour into paramagnetic. This last expression has been completed in [40] and [30] where they are stated as -respectively-

$$M(H, T) = \chi(H) - K_M(T - T_0), \quad (2.11)$$

$$M(H, T) = M_0 + \chi(H - H_0) - K_M(T_c - T). \quad (2.12)$$

However, many publications assume the validity to use the isothermal consideration, reducing the expressions of the terms M,H to:

$$M = \chi H \quad (2.13)$$

where χ stands for the volumetric magnetic susceptibility. According to, this parameter will vary depending on the concentration of oxygen in the blood (and in minor rate on the concentrations of hematocrit and charged proteins in the blood) hence the following values have been obtained by experimental means.

2. Theory fundamentals

- On the one hand, for the case that blood is *oxigenated*, the magnetic susceptibility will take the value of $\chi = -6.6 \cdot 10^{-7}$ revealing the diamagnetic behaviour of the blood that has been already commented.
- On the other hand, the magnetic susceptibility for the *de-oxygenated* blood showed values of approximately $\chi = 3.5 \cdot 10^{-6}$ in which the flow clearly yields the paramagnetic trait.

The derivation of the magnetic field intensity H and the Magnetisation M , for the isothermal assumption, is directly obtained:

$$H = \frac{1}{\mu(1+\chi)}B \quad (2.14)$$

and consequently

$$M = \frac{\chi}{\mu(1+\chi)}B \quad (2.15)$$

Even though this approach is widely used for simplicity and is able to "accurately" characterize the magnetization linear curve, it might not be enough. As it has been stated by Tzirtzilakis in [12], the human body shows extremely sensitivity to the blood flow temperature, where variations of 1-2°C can incur in different functioning of the organs. Besides, to exceed 41°C would be fatal as a result of the destruction of plasma proteins (in a high rate decomposition of albumina), hence the isothermal approach is not appropriate. Another interesting aspect to consider is the medical use of hypothermic or hyperthermic treatments (of up to a 3°C deviation from the standard 36°C temperature) in order to face diseases such as cancer [18]. The most complex yet reliable expression relating the magnetization of blood flow with temperature is given by the Lagenvin equation [64].

$$M = mN \left[\coth \left(\frac{\mu_0 m H}{\kappa T} \right) - \frac{\kappa T}{\mu_0 m H} \right] \quad (2.16)$$

where N is the number of particles per volume, m the individual particle magnetization, T the temperature and κ the Boltzmann number. However, for simplicity, it is rarely used in flow simulations due to the fact that the complexity overpasses the benefits of using it instead of the approaches already seen. This is why, in this document the non-isothermal relationship from (2.10) will be prioritized.

Once determined the mathematical description of the Magnetization M , we must account for the derivation of the forces and energy dissipation terms that result from it. According to [9], [10] the magnetization force derives from the gradient of a magnetic field tensor so

2. Theory fundamentals

that:

$$f_{FHD} = \nabla \cdot \underline{T} = \nabla \cdot \left[- \left[\mu_0 \int_0^H \frac{\partial(vM)}{\partial v} dH + \frac{1}{2} \mu_0 H^2 \right] + B_i H_j \right] \simeq {}^1 \mu_0 (M \cdot \nabla) H. \quad (2.17)$$

Once stated that the magnetization M will be computed using the non-isothermal linear expression from (2.10), the vectorial analysis together with the Maxwell Law entities will be applied to relate the FHD contribution with the external magnetic field B

$$\begin{aligned} f_{FHD} &\simeq \mu_0 (M \cdot \nabla) H = \mu_0 (KH(T_c - T) \cdot \nabla) H = {}^2 \frac{K(T_c - T)}{\mu_0(1 + (T_c - T)^2)} (B \cdot \nabla) B = \\ &\alpha(T)(B \cdot \nabla) B = \alpha(T) \cdot \left[\frac{1}{2} \nabla B^2 - \underbrace{B \times (\nabla \times B)}_{=0} \right] = \alpha(T) \frac{1}{2} \nabla B^2 \end{aligned} \quad (2.18)$$

2.4 Coupled Flow Mechanics Equations with the MHD and FHD contribution

The effects of both phenomena will not introduce any change in the principle of mass conservation, which is here known as continuity equation, then the equation from 2.1 will be recalled:

$$\nabla \cdot v = 0, \quad (2.19)$$

which is also known as the incompressibility constraint.

2.4.1 Coupled Momentum Equation

Additionally, as it has been stated in the previous section, in the momentum equation, $f_{Maxwell}$ that models the inclusion of both MHD and FHD effects so that

$$f_{Maxwell} = f_{FHD} + f_{MHD}. \quad (2.20)$$

Thus, its is just a matter of considering both terms derived previously: the Lorentz force motivated by the MHD effect and the magnetization force caused by the FHD. The total momentum equation will be hence here presented:

$$\rho \frac{\partial v}{\partial t} + \rho v \cdot (\nabla \otimes v) = \rho f_m - \nabla p + \underbrace{\nabla \underline{\tau}}_{MHD} + \underbrace{\sigma(u \times B) \times B}_{FHD} + \mu_0 (M \cdot \nabla) H \quad (2.21)$$

¹First term neglection by [10]

2. Theory fundamentals

which, if the derivations from 2.18 and the relationship expressed in ??:

$$\rho \frac{\partial v}{\partial t} + \rho v \cdot (\nabla \otimes v) = \rho f_m - \nabla p + \underbrace{\sigma(u \times B) \times B}_{MHD} + \underbrace{\alpha \frac{1}{2} \nabla B^2}_{FHD} \quad (2.22)$$

2.4.2 Coupled Energy Equation

As it has been explained, the assumption of isothermal flow is not considered given the huge importance of temperature in the circulatory system: slight variations entail in significative changes of the motion and in the organs' functioning. The, the total energy equation from 2.4 will be recovered showing the inclusion of the FHD and MHD dissipation terms. The same considerations (incompressible, monophase, homogeneous, steady-state) followed in the whole document will remain equally applied.

$$\rho c_p v \cdot \nabla T = k \Delta T + \underline{\tau} : (\nabla \otimes v) + \underbrace{\frac{J^2}{\sigma}}_{MHD} - \underbrace{\mu_0 T \frac{\partial M}{\partial T} (v \cdot \nabla H)}_{FHD} \quad (2.23)$$

The left hand side (LHS) entails the heat convective term, while in the RHS the contributions of the: Fourier Conduction Law, viscous stress dissipation, the Joule effect from MHD and magnetocaloric effect derived from the FHD momentum term are respectively representing the energy fluxes throughout the control volume. As it can be perceived, in both momentum and energy equations, the stress tensor is not defined as either Newtonian (with the Navier-Poisson Law) or Non-Newtonian formulation, as blood is consistently Non-Newtonian for low shear rates but is considered as Newtonian in many publications.

2.5 Bénard-Rayleigh Convective Instability

This convection instability takes place due to the contrarotatory convection vortices that if the temperatures of the boundaries are not equal and specially the lower wall owns the highest temperature. This phenomena, as it will be seen, is specially critical if perturbations are introducec in the inlet flow, misleading the fluid into an unstable and erratic behaviour. For simplicity, we will make use of a 2-D channel diagram in order to explain the motivation and consequences of this thermal instability. Imagine the geometry represented in Figure 2.3.

2. Theory fundamentals

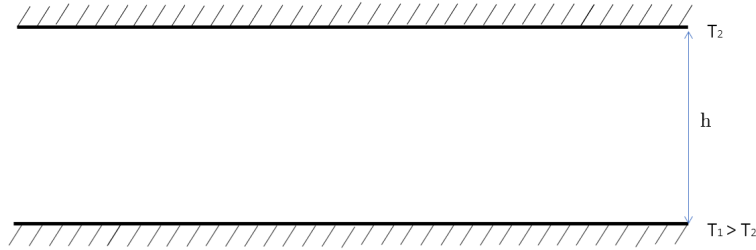


Figure 2.3: Flow in a channel heated in both superior and inferior impermeable walls

The principle behind this effect is relatively simple. If a moving fluid is being heated from below, its density will decrease and therefore it will move upwards due to the Archimedes force. However, in the proximity of the upper wall, it is cooled as this BC possesses lower temperature. This fact will motivate a descendent motion of the nearby fluid. As it can be derived, a pattern of contrarotative rolls will appear in the fluid. The presence and magnitude of them is normally estimated with the parameter known as the Rayleigh number (Ra), which relates the massic forces with the viscous stress tensor.

$$Ra \simeq \frac{\alpha \Delta T g h^3}{\nu a} \quad (2.24)$$

where α stands for the thermal expansion coefficient, ΔT does not represent the Laplacian operator of temperature this time as it yields for the variation of t between $T_1 - T_2$, g is gravity, h is the height of the channel, and ν the kinematic viscosity.

Normally, it is accepted that the critical Rayleigh number in order to consider the Rayleigh-Bénard notorious is above $Ra > 1707$, however, the geometry, boundary conditions and flow regime have a strong influence on it.

The stability analysis regarding the Rayleigh number will be now derived. Particularly, the Rayleigh-Bénard Linear Instability study is a particular case of the Orr-Sommerfeld theory, in which special analytical solutions are available. This trait is rarely achieved, as the eigenfunctions and eigenvalues from Orr-Sommerfeld theory are not considered as closed-form hence closure particular expression are needed. When the difference of temperature drives a buoyancy force -first by conduction but then by convection- that opposes the gravity term, at a certain point, the flow develops instability and tries to overcome this state by driving a subsequent convective flow. This is where the convective patterns are sighted.

Knowing that this instability is mainly caused by the adverse temperature gradient, the

2. Theory fundamentals

flow variables will be expressed in dependence of this term. One that can be defined simply is density, which in the buoyancy development suffers from small variations due to temperature such that,

$$\rho = \rho_0 + \rho', \quad (2.25)$$

being the small fluctuation ρ' function of temperature, α expansion coefficient

$$\rho' = \rho_0 \alpha (T - T_0). \quad (2.26)$$

This term, as it has been stated, is particularly low, and will only entail a noticeable effect in the buoyancy forces in the momentum equation. Hence, in the continuity term, even though the real derivation for a compressible flow should be

$$\frac{\partial \rho}{\partial t} + \nabla(\rho v) * = \frac{\partial \rho}{\partial t} + v \cdot \nabla \rho \quad (2.27)$$

in where * we have imposed the incompressibility constraint $\nabla \cdot v = 0$, the assumption that the continuity equation is directly described by the incompressible constraint is here valid. Hence, we will only consider the density variation from 2.25, 2.26 in the buoyancy term in the momentum equation, which is actually known as the Boussinesq approach. For the temperature field, we will simply advance the time and spatial solution with an advective/diffusive wave function so that, being a the thermal diffusivity and Δ the Laplacian Operator (∇^2):

$$\frac{\partial T}{\partial t} + u \frac{\partial T}{\partial x} = a \Delta T \quad (2.28)$$

Given this, now, the respective continuity, momentum and energy equations can be simplified to:

$$\begin{aligned} \nabla \cdot v &= 0 \\ \frac{\partial v}{\partial t} + v \frac{\partial v}{\partial x} &= -\nabla \left[\frac{P}{\rho_0} + gz - \alpha g(T_1 - T_2)z - \frac{1}{2}g \frac{T_1 - T_2}{h} \right] + \frac{\mu}{\rho} \Delta v \quad (2.29) \\ \frac{\partial T}{\partial t} &= -\frac{T_1 - T_2}{h} + \frac{k}{\rho_0 c_v} \Delta T \end{aligned}$$

where it is assumed that the pressure, mass and thermal forces derive from a scalar potential Φ so that its negative gradient will invoke this 3-D forces.

In an initially non-perturbed base state where the thermal equilibrium is imposed, the laplacian of the temperature is equal to zero.

$$\nabla^2 T = \Delta T = 0, \quad (2.30)$$

2. Theory fundamentals

so that the solutions of a two-dimensional domain (x,z) provide the temperature field $T = T_0 + K_1 x + K_2 z$, being A and B integration constants that satisfy the Laplace Partial Derivative Equation. Now, a linear decreasing gradient is applied in the z-axis so that 2.5 turns to be $T = T_0 - K_2 z$ where logically K_1 turns to be null.

The density field will react to this gradient in the following manner:

$$\rho = \rho_0(1 + \alpha K_2 z) \quad (2.31)$$

Now, the last term left to describe the initial state is the pressure equation, which substituting 2.31 into the z and z coordinate momentum equations and setting them to zero, one achieves:

$$\begin{aligned} \frac{\partial p}{\partial x} &= 0; \\ \frac{\partial p}{\partial z} &= -\rho_0(1 + \alpha K_2 z). \end{aligned} \quad (2.32)$$

The solution of the set of PDE from above is trivial, the pressure field will be initially predicted by:

$$p = -\rho g(z + \frac{1}{2} \alpha K_2 z^2). \quad (2.33)$$

When we evolve the flow variable field, creating ascendant and descendent flows on u and w, it is found that, at a certain moment in time, the instability is onset. This instant will be studied as a linear perturbation of the state equations from above. Regarding this, the velocity and temperature fields will now include the perturbation as a variation of their values:

$$u = u' , w = w' , \quad T = T_0 - k_2 z + T' \quad (2.34)$$

and the development of this -considerer small- perturbations can be accounted by linearizing the equations such that

$$\begin{aligned} \frac{\partial u}{\partial t} &= -\frac{\partial}{\partial x}\left(\frac{p'}{\rho}\right) + v \nabla^2 u, \\ \frac{\partial w}{\partial t} &= -\frac{\partial}{\partial z}\left(\frac{\alpha g T'}{\rho}\right) + v \nabla^2 w, \\ \frac{\partial u}{\partial x} &= 0, \\ \frac{\partial T'}{\partial t} &= K_2 w + k \nabla^2 T. \end{aligned} \quad (2.35)$$

2. Theory fundamentals

If we combine the momentum eqs in x and z axis, one obtains

$$\frac{\partial}{\partial t} \left(\frac{\partial u}{\partial z} - \frac{\partial w}{\partial x} \right) = -\alpha g \frac{\partial T'}{\partial x} + v \nabla^2 \left(\frac{\partial u}{\partial z} - \frac{\partial w}{\partial x} \right)$$

and then it is derived in the x direction

$$\frac{\partial}{\partial t} \left(\frac{\partial^2 u}{\partial x \partial z} - \frac{\partial^2 w}{\partial x^2} \right) = -\alpha g \frac{\partial^2 T'}{\partial x^2} + v \nabla^2 \left(\frac{\partial^2 u}{\partial x \partial z} - \frac{\partial^2 w}{\partial x^2} \right)$$

The incompressibility constraint is recalled so that $\frac{\partial u}{\partial x} + \frac{\partial w}{\partial z} = 0$, hence

$$\frac{\partial}{\partial t} \left(-\frac{\partial^2 w}{\partial z^2} - \frac{\partial^2 w}{\partial x^2} \right) = -\alpha g \frac{\partial^2 T'}{\partial x^2} + v \nabla^2 \left(-\frac{\partial^2 w}{\partial z^2} - \frac{\partial^2 w}{\partial x^2} \right)$$

which is simplified, by using the nabla notation with the Laplacian operator Δ :

$$\frac{\partial}{\partial t} \Delta(w) = g \alpha \frac{\partial^2 T'}{\partial x^2} + v \Delta^2 w \quad (2.36)$$

and equally accompanied by the temperature heat transfer perturbation PDE:

$$\frac{\partial T'}{\partial t} = w K_2 + \alpha \nabla^2 T' \quad (2.37)$$

To solve thus problem, we must impose the non-slip conditions at the boundaries but also thermal Dirichlet conditions along with the perturbation-free constraint order to integrate

$$BC : \begin{cases} z = 0 \Rightarrow u, w = 0, T' = 0, \frac{\partial u}{\partial x} = 0, \frac{\partial w}{\partial z} = 0, \\ z = h \Rightarrow u, w = 0, T' = 0, \frac{\partial u}{\partial x} = 0, \frac{\partial w}{\partial z} = 0, \end{cases}$$

Now, we will advance the state with a linear wave with wave number k so that :

$$\begin{aligned} w &= e^{\lambda t + j k x} \Psi(z) \\ T' &= e^{\lambda t + j k x} \theta(z) \end{aligned} \quad (2.38)$$

and this normal-mode propagated solutions are now introduced into the coupled system of momentum and energy PDEs from 2.36 and 2.37.

$$\begin{aligned} \lambda (H^2 - k_2^2) \Psi &= v (H^2 - k_1^2) \Psi - g \alpha k^2 \theta \\ \lambda \theta &= -k_1^2 \Psi + a (H^2 - k^2) \theta \end{aligned} \quad (2.39)$$

By scaling the previous equations, transformin them into non-dimensional and using the

2. Theory fundamentals

Prandtl number $Pr = \frac{\nu}{k}$, the characteristic length d, and $\sigma = \frac{\lambda d^2}{\nu}$ one reaches:

$$\begin{aligned} (H^2 - (kd)^2 - \sigma Pr)\theta &= \frac{-k_2 d^2}{a} \Psi \\ (H^2 - (kd)^2)(H^2 - k^2 - \sigma)\theta &= \frac{g \alpha d^2}{\nu} k^2 \theta \end{aligned} \quad (2.40)$$

Now both expressions are coupled and the Rayleigh number is introduced into the final form of a single PDE:

$$(H^2 - (kd)^2 - \sigma Pr)(H^2 - (kd)^2 - \sigma)(H^2 - (kd)^2)\Psi = Ra(kd)^2 \Psi \quad (2.41)$$

The eigenvalue problem that emerges from the previous equations needs the imposal of 6 BCs in order to converge to a determined solution. Both eigenfunction Ψ and its perturbed state are null at the boundaries of the domain, then two additional closure expression remain to achieve a determined problem. These, regarding the previous expression is that, the eigenvalue $\sigma = 0$ on the boundaries forces the left hand side to be equally 0. Hence, the eigenfunction problem is now ready to be numerically solved.

From linear theory exposed in Chandrasekhar [28] one knows that the stability threshold of the problem will be given by the curve at which $\sigma = 0$. Hence, the aim of the following steps will be to obtain the neutral curve regardinf the variables of our problem (Ra,Pr and k). Imposing $\sigma = 0$, expression 2.41 leads to

$$(H^2 - k^2)^3 \Psi = Rak^2 \Psi \quad (2.42)$$

Considering the coordinate reference in the axis symmetry so that the domain edges are now located at $+\pm\frac{z}{2}$. The mode solution now, for the eigenfunction Ψ is imposed.

$$\Psi = e^{+-\psi z} \quad (2.43)$$

Thus, and considering a proportional parameter γ

$$Rak^2 = \gamma k^6 \Rightarrow \gamma = \frac{Ra^{1/3}}{k^4} \quad (2.44)$$

Therefore,

$$(\psi^2 - k^2)^3 = \gamma^3 k^6 \Rightarrow \psi^2 = k^2 + (-1)^{1/3} \gamma k^2 \quad (2.45)$$

Solutions emerge from the previous expression. However, it requires the use of hyperbolic Fourier series for the even problem and also for the odd problem. If the previous function is explicitly solved by numerical means considering the dependence between the Rayleigh number Ra and the wave number k, one describes the neutral curve. If it is graphically

2. Theory fundamentals

plotted, the following image is obtained.

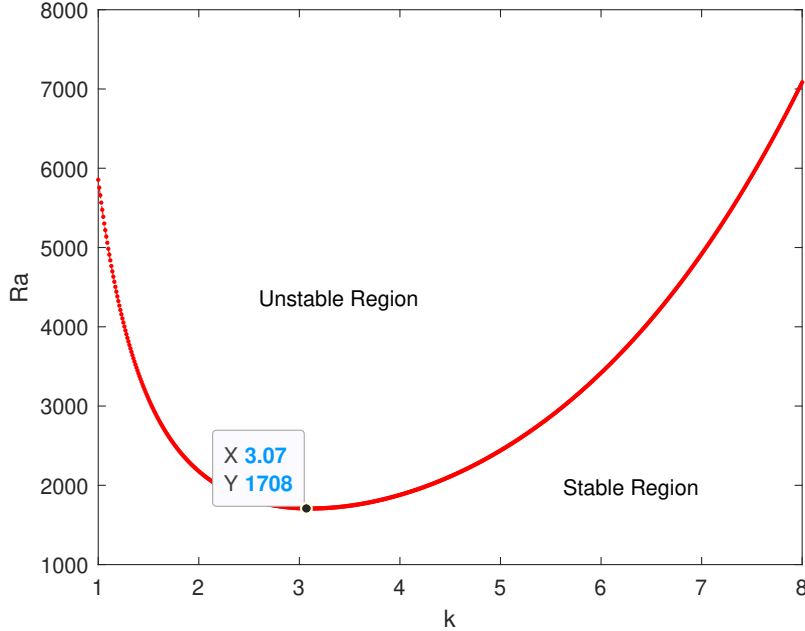


Figure 2.4: Rayleigh-Benard Stability Threshold, Neutral Curve.

Figure 2.4 will provide the critical values of $\text{Ra}=1707.762$ and the parameter $k_c=3.117$. However, different model setups and stability analysis have been carried out such as the one presented [30], [65] and [28] where different formulations and minor differences are exposed.

2.6 Non-Newtonian Flows

Generally, most of the flows are studied under the assumption of the viscous term of the momentum equation can be described with the Navier-Poisson equation, in which the kinematic viscosity μ is constant. However, even though blood simulation have been performed under these assumption, experimental evaluations demonstrate the shear-thinning viscosity of the blood. In other words, the higher the motion of the flow, the less viscosity is demonstrated. From the general formulation of viscosity, the shear stress tensor is related to the dynamic viscosity and shear rate by:

$$\underline{\tau} = 2\mu(\dot{\gamma})\dot{\gamma}(v), \quad (2.46)$$

where μ is the dynamic viscosity and γ the shear-rate tensor, given by the expression:

2. Theory fundamentals

$$\underline{\dot{\gamma}}(v) = \frac{1}{2} [\nabla \otimes v + (\nabla \otimes v)^T] \quad (2.47)$$

2.6.1 Non-Newtonian Models

Numerical and experimental results have demonstrated the necessity of developing a model which describes both Newtonian and Non-Newtonian flows in order to provide a smooth transition between both when the regimes behave in these manners. Here, several non-newtonian models will be detailed, implemented and evaluated in the following pages.

2.6.1.1 Simple and Generalized Power Law

The shear-thinning (in which blood can be classified, newtonian, and shear-thickening strongly suggests using a power-law in order to account for the shear stress. Logically, if the shear-rate is powered to a parameter n , if n is <1 we will model shear-thinning behaviour, if $n=1$ a Newtonian flow will be obtained, and if $n>1$ it will acquire a shear-thickening behaviour. Given this, the Simple Power-Law is modelled with:

$$\underline{\tau} = k\underline{\dot{\gamma}}^n \quad (2.48)$$

where k represents the consistency index and n the Non-Newtonian index. Even though it ideally demonstrates accurate description of the Non-Newtonian behaviour, it is the simplest and less reliable Non-Newtonian model to implement. Hence, as most of the steps carried out in the numerical flow dynamics, it yields a compromise solution between accuracy aimed and computational cost/problem complexity to be invested.

From the work of Shibeshi et al [66], the corresponding parameters of several Non-Newtonian models have been adjusted for the standard blood flow. By evaluating experimental results and using an adjustment of least squares, the values of $k=0.017$ and $n=0.708$ have been obtained. Given this, a deviation of the non newtonian exponent of almost a 30 % has been observed.

The addition of other parameters to the equations based on empirical results may improve the limited accuracy of this method. An example of it is the Generalized Power-Law [67], in which the most accurate results for these Power-Law family models are predicted. The

2. Theory fundamentals

mathematical formulation for the Generalized Power Law is the following:

$$\begin{aligned} \underline{\tau} &= k(\dot{\gamma}) \dot{\gamma}^{n(\dot{\gamma})} \text{ so that} \\ k(\dot{\gamma}) &= \tau_\infty + \Delta\tau \cdot \exp \left[-\left(1 + \frac{\dot{\gamma}}{a} \right) \exp \left(\frac{-b}{\dot{\gamma}} \right) \right] \\ n(\dot{\gamma}) &= n_\infty + \Delta n \cdot \exp \left[-\left(1 + \frac{\dot{\gamma}}{c} \right) \exp \left(\frac{-d}{\dot{\gamma}} \right) \right] \end{aligned} \quad (2.49)$$

The experimental parameters, by using a regression of Experimental Blood fluid in [68], provide the values of $\tau_\infty = 0.0345$, $\Delta\tau = 0.25$, $n_\infty = 1$, $\Delta n = 0.45$, $a=50$, $b=3$, $c=50$ and $d=4$. One must notice that probably the main drawback of this method, even though its simplicity and its quasi-inexistent possibilities to diverge, is the fact that Power-Law models will not consider yield stress effects [69]. This is why artificial results can be easily obtained when implementing this method.

Regarding [13], once they analized the Power-law family of models for modelling the blood flow in an Aorta CAD, only acceptable results will be obtained in medium shear rates for the simple formulation. Thus, when low and high shear rates, their mathematical description tends to fail. This is why, generalized an modified power law models try to extend the validity of this original idea without incurring in excessive changes to the morphology, being usually valid for low and high regimes. The improvements introduced will be combining Newtonian and Non-Newtonian traits or including yield stresses at both regimes.

2.6.1.2 Casson

Power-law-type results but also the ones obtained with the Carreau model -which is not described in this publication- evidence the need of another formulation to represent a more gradual transition from the newtonian regime to the yield region. This is why, in [70], the Simple Casson model was firstly derived and entailed a promising application in the study of viscoelastic fluids. In fact, according to [13], this model is the one that fits better the behaviour curve of blood against shear stress. Actually, it is meant as this family of models, since the basic formulation might introduce divergence problems but also will not consider several important traits. The basic form of the model is given by the expression:

$$\eta(\dot{\gamma}) = (\sqrt{\eta_c} + \sqrt{\tau_c/\dot{\gamma}})^2 \quad (2.50)$$

where η is the effective or apparent viscosity, τ_c the yield stress and quantified approximately as 0.0038 Pa in [71], and η_c the value of the Newtonian-ish viscosity then the shear

2. Theory fundamentals

rate tends to inf, being this value 0.0035 calculated in [72].

These values are not arbitrary or just phenomenological since they entail an explanation in them, which has been given in [4]. Knowing the dependence of the effective viscosity and the shear stress, it might be more easily visualized if we express the anterior formula 2.50 in terms of shear stress such that:

$$\begin{aligned}\tau(\dot{\gamma}) &= (\sqrt{\tau_0} + \sqrt{k_0 \cdot \dot{\gamma}})^2, \text{ where} \\ \tau_0 &= c[(1 - \phi)^{-q/2} - 1] \text{ and} \\ k_0 &= \mu_f(1 - \phi)^{-q}.\end{aligned}\quad (2.51)$$

The hematocrit independent blood viscosity μ_f is a consequence of the attraction between adjacent red blood cells, therefore the aggregation and rouleaux effect is induced. This effect can be minorized or even disabled by the application of shearing stress. Also, parameter k_0 depends on μ_f but also in the haematocrit or equivalently the erythrocyte volume fraction of the blood (ϕ), which is normally set to 0.45 for healthy values. τ_0 accounts for the interactions between the fibrinogen and erythrocytes as explained in [4], and it is subsequently sensitive to the morphology of the aggregation particles (modelled with c) and also the haematocrit ϕ .

The characteristic curve of the Casson model, which is one of the most solid shear-thinning viscosity models, is visually graphed in Figure 2.5. In it, an adjustment to the blood rheology has been made. As it can be seen, for low shear rates the description possesses an evident deviation to the Newtonian model, but as it is increased, this difference is rapidly lowered.

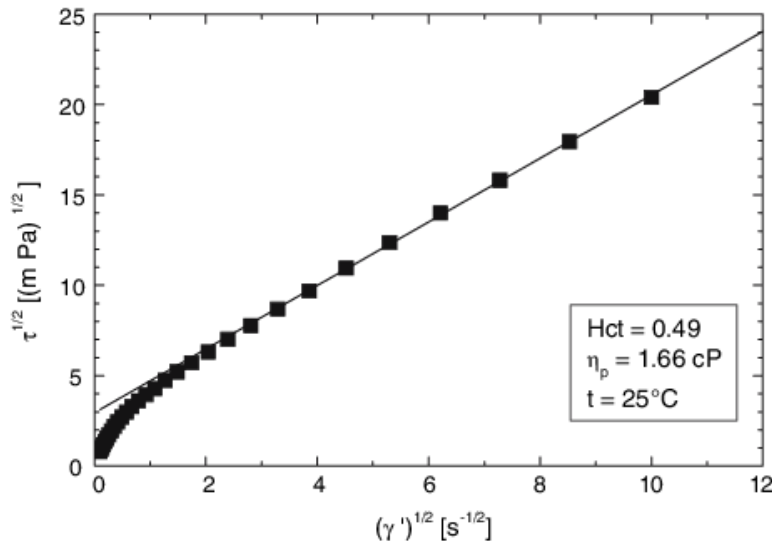


Figure 2.5: Shear stress vs shear rate typical curve for the Casson model. Source: [4]

2. Theory fundamentals

Regarding the evaluation of experimental data, it has been noted that Casson curve is not fully capable to describe the whole shear stress scope, this is why 3 equations or adjustements of it are simultaneously usually employed for having great accuracy on the behaviour of blood for the three different regimes of $\dot{\gamma}$. This weakness and some probability of driving divergence on the solution for really low shear rates has led to the enhancement and extension of the Casson model such as the sub-models that will be presented immediately.

2.6.1.3 Casson-type K-L

The K-L model Casson-type was firstly proposed by Luo and Kuang in [73] and considers an additional shear rate modifier, with the aim of providing a more accurate description of the shear-thinning non-newtonian behaviour in comparison with the existent Casson or either the Newtonian approach. This idea was later proven by Zhang et al in [74] as it showed less deviation from the experimental data. Knowing this, the K-L model is the following three parameter constitutive equation.

$$\eta(\dot{\gamma}) = \frac{1}{\dot{\gamma}} [\tau_c + \eta_c (\alpha_1 \dot{\gamma} + \alpha_2 \sqrt{\dot{\gamma}})] \quad (2.52)$$

Where, differently to the Casson standard model from [70], $\tau_c = 0.005$, $\eta_c = 0.0035$ and the blending parameters α_1 and α_2 are set to 1 and 1.19523 respectively.

According to [13], in the comparison of the different Non-Newtonian models, this was the one that achieved best results, even in front of the modified Casson. However, in this publication the Quemada model -which will be also accounted in our investigation - was not considered.

2.6.1.4 Modified Casson

The Modified Casson, similarly to the K-L Model, tries to extend the range of application of the Standard Casson without the requirement of using the three curves. It also uses three parameters: η_c , τ_c and λ , being this last term derived from the Carreau model and being known as the relaxation time constant (unit=seconds). One of the first evidences of using this model is the paper from Buchanan et al [75], even though it is not known if it was firstly derived there.

The expression used for this model, which will give the effective viscosity, is the following

$$\eta(\dot{\gamma}) = \left(\sqrt{\eta_c} + \frac{\sqrt{\tau_c}}{\sqrt{\dot{\gamma}} + \sqrt{\lambda}} \right)^2 \quad (2.53)$$

2. Theory fundamentals

As it can be seen, it is a crossed equation with the morphology of the Casson expression from 2.50 but considering the additive effect of the relaxation time such as the term in the Cross (Carreau-Bird) model.

The parameters are obtained by LSS fitting to the experimental data and will result - according to [76]- in $\eta_c=0.002982$, $\tau_c=0.02876$ and $\lambda = 4.020$.

In comparison with the K-L model, as it has been reported in [13], it entails an artificial overprediction of the shear stress at high shear rates whilst underpredicted in low shear rates as it has been demonstrated in [77]. Nonetheless, both models, but specially the Modified Casson -introduced by the relaxation time in the fraction- have the advantage of not allowing the solution diverge when the shear rate ($\dot{\gamma}$) tends to the null value.

2.6.1.5 Quemada model

This shear-thinning model was firstly proposed by Dr. Quemada in [78]. It is considered to be the most complex of the evaluated here but probably the most interesting as it employs 5 parameters to describe the shear-thinning behaviour of the blood. This fact, even though it adds complexity to its fit to the experimental data by LSS means, gives versatility to describe a wide variety of shear-thinning fluids along the whole scope of shear rate. The expression of the effective viscosity regarding the Quemada model is described as the following:

$$\eta(\dot{\gamma}) = \mu_f \left(1 - \frac{1}{2} \frac{k_0 + k_\infty \sqrt{\gamma/\gamma_c}}{1 + \sqrt{\gamma/\gamma_c}} \phi \right)^{-2} \quad (2.54)$$

One should notice that this model includes the previous Casson models if several transformation or equivalences are set to the parameters. For instance, if $\lambda = \gamma_c \left[\frac{1 - \frac{1}{2} k_0 \phi}{1 - \frac{1}{2} k_\infty \phi} \right]$ the Modified Casson from 2.53 is obtained. Similarly, the other Casson expressions can be derived from this model as well.

Regarding the phenomenology signification of the parameters introduced, the term that multiplies the hematocrit ϕ is known as the intrinsic viscosity of erythrocytes, and is sometimes represented with the parameter k_q [4] [79]. The plasma viscosity is represented by the parameter μ_f as it has been already seen in the previous models. The shear rate demonstrates additional dependency of RBC shape variation and aggregation phenomena. In the other hand, k_0 and k_∞ will account for the shear rate values when it tends to 0 and

2. Theory fundamentals

infinity respectively. As it has been seen, γ_c will establish the relationship between rouleaux formation and RBC aggregation. The three last parameters described, k_0 , k_∞ and γ_c are usually simplified and considered as functions of particles. Once described, the values corresponding to blood flow, according to [79] are the following: $\mu_f = 0.0012$, $\phi=0.45$, $\gamma_c=1.88\text{s}$, $k_0=4.33$ and $k_\infty=2.07$.

The fact that the Quemada model indeed considers "multiphase" phenomena even though it is simulated here with monophase flow adds physical relevance to the problem and to the model. Regarding the results, [4] states that it is the best model of the here evaluated. A similar scenario is also described by [79], [80]. However, results also demonstrate that the prediction of the flow variables, including the velocity magnitude, might be slightly greater than the obtained by the other Non-Newtonian models, and some times, the blunt velocity profile expected in thick vessels is more sharp and parabolic.

2. Theory fundamentals

2.7 Multiphase Hemodynamics

The real blood flow, which has been briefly commented in Section 2.2, consist of a complex mixture of different elements: plasma-layer on its majority, which indeed includes charged proteins (with albumin being the most numerous) and salt ions that travel through the blood, then erythrocytes, which can nearly reach 45 % of the fluid volume, and some other cells (leukocytes and platelets) and other wide amount of minor components which do not have relevant impact on the flow. Even though many investigations such as [1], [18] and even this document considers the blood as a homogeneous phase, many other attempt to describe with higher fidelity but also complexity the real blood flow by introducing one additional phase such as in [45], [47] or by considering the discretized element-particle physics such as micropolar fluids in [30] suspended in the plasma layer.

The latest models and investigations on multiphase hemodynamics primarily consider two phases of the blood flow due to their concentration predominance: the plasma layer and an haematocrit core. Experimental investigations reveal that both components are not forming a discrete pattern when flowing through vessels, they act as in-miscible, and the core of the vessel is usually occupied by a torrent of red blood cells surrounded by a cell-free plasma layer, which is confined by the vessel walls and innerly by the haematocrit flow. Serve the following image as a quick idea of the the two-phase model flow.

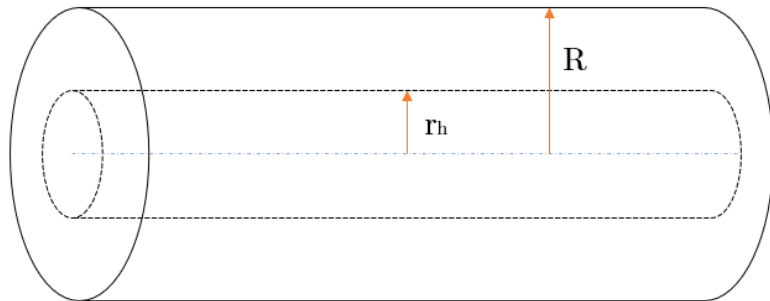


Figure 2.6: Two-Phase Scheme of the Blood Flow

In both sections, a Poiseuille profile is inferred. The inter-phase actually entails some complexity to describe it accurately, however, the most widely-used assumptions consider discontinuity of the dynamic viscosity μ , but continuity of velocity and shear-stress. Most of times, the model must be closed by using semi-empirical or empirical laws to enforce results to be accurate.

2. Theory fundamentals

Another interesting trait to bare is the model of each of the phases. Whilst commonly most of investigations defend the Newtonian approach for both, depending on the geometry and its dimensions, but also on the shear rates, the Non-Newtonian model to describe the shear behaviour may be more convenient. [47] places a threshold of $300 \mu\text{m}$ in vessels size to place where newtonian and non-newtonian models should be used.

The importance of the multi-phase hemodynamics is not only to have slighter more accurate results on the blood flow. By experimental means, some significant effects have been noted and that impossibly cannot be described with the traditional mono-phase assumption. This is why, when these effects want to be considered, the use of multi-phase hemodynamics is indeed irremediable. Find, in the following section, the most remarkable multi-phase phenomena noted by experimental means and that require this last modelling.

2.7.1 Effects

2.7.1.1 Roleaux - Smoluchowski effect

Roleaux, the plural name for roleau, and refer to blood coagules caused by the aggregation of Red Blood Cells, specially motivated when plasmatic protein is relatively high. Consequently, an increment of the Erythrocyte Sedimentation Velocity is induced. This excessive sedimentation is commonly caused by an underlying disease, but it is not the only cause of the roleaux effect. Albumin, the most present plasmatic protein, acts as inhibitor of this phenomenon. The coagulation dynamics have been described by the Smoluchowsky equation [81], which predicts the evolution in time of RBC aggregations by statistical means. The equation is the following one:

$$\frac{\partial n(x,t)}{\partial t} = \frac{1}{2} \int_0^\infty K(x-y,y) n(x-y,t) n(y,t) dy - \int_0^\infty K(x,y) n(x,t) n(y,t) dy \quad (2.55)$$

where n is the variation of particle size, and K , the kernel coagulation parameter, which represents the speed at which different size particles interact. It is commonly defined by a complex function, dependant on the brownian motion of particles. As it can be seen, the Smoluchowsky expression 2.55 is not but a particularization of the Fokker-Planck equation.

Definitely further learning of this effect can be acquired from the thorough investigation carried out by [82].

2. Theory fundamentals

2.7.1.2 Fahraeus effect

This experimental phenomenological law describes the dependency or proportionality of the concentration of RBC in the general blood flow to the diameter of capillaries or vessels. This is why, in thin capillars smaller volume rates or haematocrit is witnessed in contrast with large arteries or veins. The considerably best semi-empirical equation has been obtained, using non-linear regression and curve fitting, by Pries et al [46], relating the tube hematocrit with the discharge hematocrit and diameter.

$$\frac{H_t}{H_d} = H_d + (1 - H_d)(1 + 1.7e^{-0.415D} - 0.6e^{-0.0011D}) \quad (2.56)$$

being H_t the tube hematocrit, H_d the discharge hematocrit and D the diameter in μm .

2.7.1.3 Fahraeus-Lindqvist effect

The Fahraeus-Lindqvist effect is indeed direct consequence of the Fahraeus effect but is also influenced by other flow traits. This phenomenon describes the dependence of the apparent viscosity on the tube diameter. The reason behind this causality is the fact that the RBCs apparently flow in the inner core of the vessel while the plasma cell-free fluid layer tries to surround it. As it has been seen, the hematocrit is dependent on the vessel diameter, and since viscosity of plasma and hematocrit is logically different, the apparent viscosity of the overall fluid is derivedly dependent on the vessel diameter as well. However, the mathematical description of this phenomenological effect is indeed challenging and a theoretical model named "cell-free marginal layer" has been developed to yield for this effect. Again, in a different publication, Pries et al [83] have obtained, by regression and connection with Fahraeus equation, a complex function that describes the empirical results, relating the apparent viscosity with the discharge hematocrit H_d and the vessel diameter D.

2.7.1.4 Additional Effects

Other effects non-named after their investigations, with less impact in the solution, have been reported as well. One of them, which is present in the 3 effects but was initially the first noticed, is the existence of a cell-free layer of plasma in the proximity of the boundaries. Another interesting trait is the blunter velocity profile than the theoretical parabolic from the Poiseuille flow. Finally, in bifurcations, a disproportional and chaotic time-variating of concentrations of plasma and blood cells are witnessed as well. All the previously summarized phenomena are the most relevant in terms of multi-phase flows so that it require its formulation and implementation to achieve high-fidelity results.

Chapter 3

Methodology

3.1 Problem Description

3.1.1 Physical Application. 2-D Turbulent biomagnetic fluid flow in a rectangular channel, localized magnetic field

The benchmark problem has been described and fully solved in [1], therefore this publication will serve as the reference data to compare our results. The configuration of the problem consists in a rectangular duct geometry, of length L and height h , in which there's a flow of a determined fluid: homogeneous blood. In a particular region of the domain -defined by the coordinates x_{M1} and x_{M2} , there's a constant magnetic field applied, with its subsequent effect in +Y direction with intensity H_0 . Our purpose is to analyze its influence to the blood through the FHD and MHD modelled contributions.

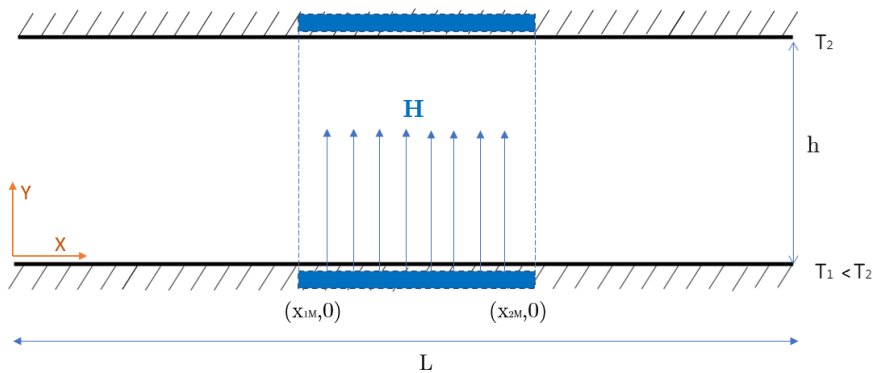


Figure 3.1: Flow Geometry Scheme

Regarding the boundaries of the problem, we have 2 non-slip walls in which temperature is not equal ($T_1 \neq T_2$) and in which the velocity profile (u, v) will be consequently set

3. Methodology

to 0. The only two remain regions that limit the problem are the inlet and outlet. Inlet is characterized with the Poiseouille velocity profile, whilst the outlet will logically describe the outflow conditions in which the derivatives of the fluid variables will be set to 0.

Since the magnetization force, in this case, will be certainly parallel to the field intensity H , the FHD term can be written as in 2.18, and in conjunction with the Maxwell Law relating the flux current density with the field intensity $J = \nabla \times H$, the FHD term can be finally expressed as:

$$\mu_0(M \cdot \nabla H) = \mu_0|M|\nabla|H| + \frac{|M|}{|H|}(J \times B) \quad (3.1)$$

As it can be seen in [12], the relationship between the modulus of magnetization ($|M|$) and field intensity ($|H|$) can be approximated with the isothermal magnetic susceptibility χ . Hence,

$$f_{Maxwell} = \mu_0|M|\nabla|H| + (1 + \chi)(J \times B), \quad (3.2)$$

where χ will indeed vary depending if blood is oxygenated or not as it has been detailed in prior sections.

By analyzing the magnetic field B , it will be similarly expressed vectorially as it will only posses value in the $+y$ direction so that $B = (0, B_y, 0)$. Now, the total component-by-component equations for this problem will be derived, assuming the Boussinesq approach and Newtonian stress tensor:

- Continuity

$$\frac{\partial u}{\partial x} + \frac{\partial v}{\partial y} = 0 \quad (3.3)$$

- Momentum, x-axis :

$$\rho \left(u \cdot \frac{\partial u}{\partial x} + v \frac{\partial u}{\partial y} \right) - \frac{\partial p}{\partial x} + \mu \left(\frac{\partial^2 u}{\partial x^2} + \frac{\partial^2 u}{\partial y^2} \right) + \mu_0 M_y \frac{\partial H_y}{\partial x} - \sigma B_y^2 \cdot u \quad (3.4)$$

- Momentum, y-axis :

$$\rho \left(u \cdot \frac{\partial v}{\partial x} + v \frac{\partial v}{\partial y} \right) - \frac{\partial p}{\partial y} + \mu \left(\frac{\partial^2 v}{\partial x^2} + \frac{\partial^2 v}{\partial y^2} \right) \quad (3.5)$$

3. Methodology

- Energy

$$\begin{aligned} \rho c_p \left(u \cdot \frac{\partial T}{\partial x} + v \frac{\partial T}{\partial y} \right) = & k \left(\frac{\partial^2 T}{\partial x^2} + \frac{\partial^2 T}{\partial y^2} \right) + \mu [(\nabla \times u) : (\nabla \times u) + (\nabla \times u)^T : (\nabla \times u)] \\ & + \mu_0 KTH \left(u \cdot \frac{\partial H_y}{\partial x} + v \cdot \frac{\partial H_y}{\partial y} \right) + \sigma B_y^2 u^2 \end{aligned} \quad (3.6)$$

The magnetic field here will be approached through a finite-gradient mathematical expression which will imply a simple but effective and realistic approach of the magnetic field behaviour. The reason behind this approach is the numerical difficulties that take place for strong -or purely-defined - gradients where variables such as the magnetization and susceptibility take quasi-infinite values. The magnetic field formula that will provide a smooth transition to the localized vertical magnetic field will be the following:

$$H(x, y) = \frac{H_0}{2} [\tanh(a_1(x - x_1)) - \tanh(a_2(x - x_2))], \quad (3.7)$$

where x_1 and x_2 coordinates represent the magnetic field location and a_1, a_2 weighting parameters will define the strength of the gradient.

The boundary conditions to be applied will be the following:

- Inlet: ($x=0, 0 \leq y \leq h$) $\Rightarrow u = u(y), v = 0, T = T(y)$
 - Outlet: ($x=L, 0 \leq y \leq h$) $\Rightarrow \partial u / \partial x = 0$
 - Lower Wall: ($y=0, 0 \leq x \leq L$) $\Rightarrow u, v = 0, T = T_1$
 - Upper Wall: ($y=h, 0 \leq x \leq L$) $\Rightarrow u, v = 0, T = T_2$

For simplicity and in order to run a parametric study, we will work in a dimension-less frame and hence the prior equations will be described with non-dimensional parameters. By doing this, the change of the MHD and FHD contributions along with the blood susceptibility to it will be straightforward. First, we will introduce the commonly-used non-dimensional numbers that will appear in the equations:

$$\begin{aligned} Re &= \frac{\rho u_r h}{\mu} & Pr &= \frac{c_p \mu}{\kappa} \\ E_c &= \frac{u_r^2}{c_p(T_2 - T_1)} & Ra &= \frac{\alpha \rho_0 g h^3 (T_2 - T_1)}{a \mu} \end{aligned}$$

where Re is the Reynolds number (convective forces against viscous term), Pr the Prandtl number (viscous diffusion term against thermal diffusivity), E_c the Eckert number (kinetic

3. Methodology

energy vs boundary layer enthalpy) and additionally the non-dimensional temperature number $\theta = \frac{T_1}{T_2 - T_1}$ will be used. As it can be seen, the Reynolds number in here is defined different to the Reynolds number from Tzirtzilakis [12], [1], where it is referred to the mean velocity instead if the maximum. Consequently, in order to achieve the same results for the same case than in [1], given the difference in the Reynolds number definition, the Re must be doubled.

Now, the last two terms to define are Mn_F and Mn_M which will account for the MHD and FHD contribution. Their value will be obtained with their dimension-less form of:

$$Mn_F = \frac{\mu K H_0 (T_1 - T_2)}{\rho u_r^2}, \quad Mn_M = \frac{\mu_0 \sigma H_0 h^2}{\mu}$$

Once the non-dimensional set of Navier-Stokes equations are presented including the FHD and MHD contributions and the parameters of the equations defined, a benchmark validation and a parametric study will be applied to this geometry as the first initial results to verify the code implementation. The results must be consistent with [1], even though as it has been commented their model can be further improved.

3.1.2 Geometry and Mesh

The geometry which will be simulated throughout the whole document will be based on the 2-D rectangular duct introduced in [1] however similar results would emerge in a 3-D case as it will be seen. Depending on the magnitude of this geometry, the onset of the instabilities and vortexes will logically depend, however the conclusions that will be derived can be scaled accordingly to the expressions and equations provided. This rectangular duct, as Figure 3.2 reveals, is made up by a pipe with the dimensions of length 0.9 m and height 0.05 m.

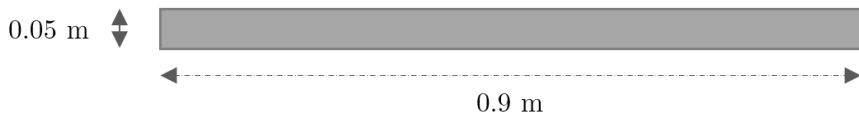


Figure 3.2: 2-D Blood Flow Geometry Scheme

From this configuration, a structured mesh with quadrilateral elements is generated so as to model the blood flow, the inflow, outflow and the two upper and lower walls which will act as boundaries. Specially these two last, will play an important role when the Rayleigh-Bénard instability of a blood flow will be evaluated in the Results section.

3. Methodology

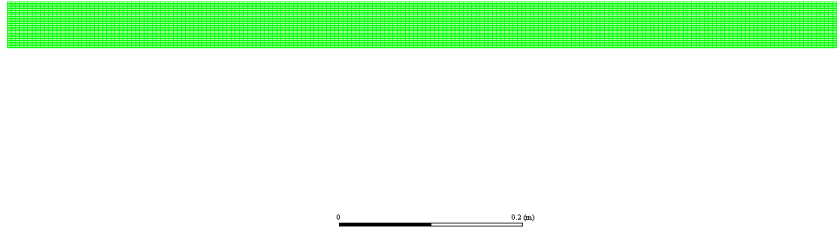


Figure 3.3: 2-D Blood Flow Mesh

The mesh created in Figure 3.3 consists of 8000 cells, 16240 faces and 8241 nodes. Even though it could be indeed finer, the resolution has proven to be accurate enough to predict all the expected behaviours and instability phenomena hence it is assumed to be satisfactory. As future work or even for the evaluation of micro-scale applications or more relevant non-linear effects, a refinement and grid convergence study could be further applied. More information about the Mesh quality can be found in Table 3.1. As it can be witnessed, values demonstrate high accuracy to use the mesh in the upcoming simulations.

• Volume Statistics	
minimum volume	5.62496 e-06
maximum volume	5.625 e-06
total volume	4.5 e-02
• Face Area Statistics	
minimum	1.24999 e-03
maximum	4.5 e-03

Table 3.1: Additional mesh quality information

3.2 Numerical Setup

3.2.1 SIMPLE Algorithm

The algorithm known as SIMPLE (Semi-Implicit Method for Pressure-Linked Equations) was firstly developed by Patankar and Spalding in [84]. It is known as an engineer-type solver due to the fact that it recurs to iterative procedures in order to achieve a fast, simple but accurate solution. The application of this solver algorithm is limited to Incompressible

3. Methodology

Flows, where density is assumed constant in most cases, the incompressibility is applied and pressure is totally independent of density. The equation of state is no longer valid in this regime.

The procedure regarding this method, in contrast with Boundary-Layer Theory implementation imperant in Academia, will redound in the simplicity of the algorithm and less computational expense. This is why, this method is rather used in industrial and company applications than for investigation purposes, where more detail and particularly more accuracy regarding some flow variables might be needed. The novelty of the method, is, as it is being advanced, the consideration of the 3-D elliptic flow as parabolic 2-D flow where corrections on pressure are made to hold the accuracy and stability of the solution.

Firstly, the method departs from an “estimated” pressure in the boundary region, to then introduce these values in the Navier-Stokes Momentum equation and obtain the velocity field dependent of these estimated values. It is logically derived that the convergence of the results will strongly depend on the deviation of this initial guess from the real pressure field. However, the velocity field obtained through this initial guess will not now satisfy the Continuity Equation, which has been in fact reduced to the so-called “incompressibility constraint”. Consequently, in this stage the velocity distribution will be now called or known as intermediate velocity field.

Now, an correction can be applied to intermediate this velocity , will be equally expressed as the pressure field to satisfy in the end the continuity equation. This stage will be applied iterative until a determined and accepted accuracy is set regarding both momentum and continuity equations. Hence, following Patankar’s derivation and notation from [84], the pressure field will be now conformed by the intermediate pressure field and the corrective contribution:

$$p = p^* + p' \quad (3.8)$$

being p^* the intermediate velocity field and p' the corrective term. Actually, experience in numerical procedures demonstrates the need of an under-relaxation parameter ω - logically between 0 and 1- is needed to prevent the residuals divergence due to non-linearity. Normally, it is accepted that the 0.6 value may be the most successful. Hence, 3.8 is better described - according to performance issues- as:

$$p = p^* + \omega p' \quad (3.9)$$

Besides, if flow is unsteady as it will be here, the Poisson equation must be satisfied.

$$\nabla^2 p = \frac{\rho}{\Delta t} \cdot (\nabla \cdot u) \quad (3.10)$$

3. Methodology

By repeating this iterative and corrective methodology, residuals will decrease until the convergence threshold is satisfied. This will be the point in which the solution will be considered to satisfy all the equations at the same time. This method, even though can be initially esteemed as simple (not related with its name), in fact it is one of the most used in industrial applications as a result of its high performance and fast convergence of results. However, if high-resolution and detailed phenomena (such as non-linear waves) are aimed, some other procedures in which boundary layer procedures and closure equations are used may be more suitable. These methods are subsequently preferred in Academia and high standard investigations.

The application of this method is already implemented in the ANSYS-FLUENT software, which will be used to carry out all the CFD simulations. As blood flow is considered to be incompressible -it is a dense liquid similar to water- and it indeed moves at $M<0.24$, the use of this algorithm is fully suitable for the blood model.

3.2.2 Turbulence Modelling

According to one of the most important physicists of the last century, Richard Feynman, turbulence mathematical description is the last problem of classic mechanics to be solved. Unfortunately, even though several accurate methods -which are known as models- have been developed over the last decades with promising results, an analytical expression that fits all the scenarios has not been yet obtained. And it seems that -unfortunately- it will remain still unknown in the near future.

Turbulent flows are known to entail a relatively low diffusion of the momentum term, strong convection and sudden and strong variation of the flow variables. The hostility of this nature is subsequently due to the strong non-linearity of the equations. Unpredictability, fluctuation, randomness, boundary layer separation, multi-scale apparition, diffusion and mixing phenomena are commonly used nouns to describe this characteristic motion. Accordingly, energetic vortical structures are prone to develop within turbulent flows.

The quantification of how turbulent a flow is, is normally determined by using the Reynolds number, which relates the convective term with viscosity forces. If this number is in the order of magnitude of 10^3 or higher, a turbulent flow is probably onset. In the contrary, if it is beyond this theoretical threshold value, flow can be assumed to be laminar.

The fundamentals of the theoretical background of Turbulence Flows are assumed to be known by the reader. Nonetheless, if not, publications such as [17] and [85] do describe this phenomenon with great clarity. Special attention must be paid to the contributions

3. Methodology

and ideas proposed by Reynolds, Landau and Kolmogorov, whose principles have served as a strong basis of the later development.

In the present document, cases of laminar and turbulent flows regarding the blood motion will be investigated. In order to simulate the turbulent flow accurately, the realizable k- ε model will be employed due to its high accuracy demonstrated in both mean and close-to-boundary regions.

3.2.2.1 Realizable k- ε turbulence model

The choice of the k- ε realizable model has been done as a result of its robustness and accuracy in not too-complex geometries. Along with the Shear Stress Transport k- ω turbulence model, it is assumed to be one of the most solid and reliable, hence its wide application in the CFD community. As its name reveals, it derives from the standard k- ε standard model from [86] [87] but developing an enhancement in the prediction of flows with axysymmetry, jet, vortexes, rotations and boundary later treatment. This improvement is mainly due to the change introduced to the turbulent viscosity, which now is not assumed to be constant. Nonetheless, as its main drawback, some artificial turbulent viscosities can be noted in regions where strong vortexes and stagnation points are present.

The realizable k- ε model operates with two transport equations which define the variables k (specific dissipation rate) and ε (turbulent kinetic energy). These are accordingly described with, first the specific dissipation rate equation and then followed with the turbulent kinetic energy closure expression

$$\frac{\partial}{\partial t}(\rho k) + \frac{\partial}{\partial x_j}(\rho k u_j) = \frac{\partial}{\partial x_j}\left[(\mu + \frac{\mu_t}{\sigma_k})\frac{\partial k}{\partial x_j}\right] + G_k + G_b - \rho \varepsilon - Y_M + S_k \quad (3.11)$$

and

$$\frac{\partial}{\partial t}(\rho \varepsilon) + \frac{\partial}{\partial x_j}(\rho \varepsilon u_j) = \frac{\partial}{\partial x_j}\left[(\mu + \frac{\mu_t}{\sigma_\varepsilon})\frac{\partial \varepsilon}{\partial x_j}\right] + \rho C_1 S_\varepsilon - \rho C_2 \frac{\varepsilon^2}{k + \sqrt{v\varepsilon}} + C_{1\varepsilon} \frac{\varepsilon}{k} C_{3\varepsilon} G_b + S_\varepsilon \quad (3.12)$$

The terms represented with the letter C are known as constants of the method, while σ yields the specific Prandtl numbers, Y_m a function of dilatation, G_b and G_k turbulent energy produced respectively by buoyancy and velocity variations ans lastly the additional parameters of $C_1 = \max(0.43, \frac{\eta}{\eta+5})$, $\eta = S_\varepsilon^k$, $S = \sqrt{2S_{ij}S_{ij}}$ have been also included. Furthermore, optional source terms in this closure equations can be introduced by the author hence the use of the variables S_k and S_ε

Chapter 4

Results

4.1 Validation Case

4.1.1 Turbulent 2-D Rectangular duct with Localized Constant Magnetic Field

The geometrical setup and problem definition has been already explained in the Section 3.1.1. Here the parametric study and validation of the UDF code and setup with the results from [1] will be discussed.

As a Validation Case, the same conditions from [1] will be used. For the Turbulence regime, the realizable k- ε turbulence model will be employed due to its high ability to describe the mean flow yet also in the proximity of the boundaries.

As it has been seen, the dimensional equations have been turned into dimension-less in order to smoothly display a parametric study in this section but also to simplify the implementation of the MHD and FHD flow contributions in the momentum equation (Lorentz Force, Magnetization Force) and the subsequent dissipation of energy with the magnetocaloric term and the Joule which inherently derive from the momentum terms.

The density of the blood, due to the fact that it will be considered as mono-phase, will be $\rho = 1050 \frac{\text{kg}}{\text{m}^3}$ accorded as an average standard value in most of all the other publications. Health care usually sets as normal conditions between 1040 and 1070 values overall, even though in blood tests the blood is usually analyzed through the different components isolated. The Blood is assumed to be Newtonian in this case, thence the dynamic viscosity μ is set to constant with the value of ($\mu = 3.2 \cdot 10^{-3} \frac{\text{kg}}{\text{m}\cdot\text{s}}$). In a similar manner, Tzirtzilakis [1] defines the values -for the blood model- of $c_p = 14.283 \frac{\text{J}}{\text{kg}\cdot\text{K}}$ and $k = 1.832 \cdot 10^{-3} \frac{\text{J}}{\text{m}\cdot\text{s}\cdot\text{K}}$.

4. Results

According to [88], the averaged electric conductivity is set to $\sigma = 0.7 \frac{s}{m}$ for the stationary case, however this measuring is sometimes too conservative. In reality, this number depends logically on the shear stress and on the hematocrit concentration, therefore, an increment up to a 10 % should be expected regarding [89]. Thus, here the value $\sigma = 0.8 \frac{s}{m}$ will be here assumed.

The flow inlet will use an averaged normalized velocity $u_r = 3.2 \cdot 10^{-3}$, yet it will simplify the systole-diastole cycles pumped by the heart contraction. The temperatures in the boundaries will also be set to: $T_u = 315K$ and $T_l = 283.5K$ and as it can be proofed no convection instabilities will take place here.

Finally, the dimension-less numbers or parameters are left to be define and fully characterize the flow. The Prandtl and Eckert numbers will take the values of, respectively, $Pr= 25$ and $Ec= 3.3 \cdot 10^{-7}$. Regarding the relationship between convective and viscous forces, what is known as the Reynolds number, in the Tzirtzilakis paper [1] is modelled with the magnitude of $Re=200$, however, it is defined to the average value and not to the maximum as it has been done in our UDF, thence, here the case of $Re=400$ should be evaluated in order to compare the same scenario. Additionally, the conditions of $Re=200$ and $Re=600$ will be equally studied.

All the previous data explained for the setup of the simulation can be gathered and summarized as Table 4.1

Variable	Value
ρ	1050 kg/m^3
u_r	0.0016 m/s
Re	400
μ	Power Law, $k=0.017$, $b= 0.708$
c_p	14.286 J/kgK
k	$1.832 \cdot 10^{-3} \text{ J/msK}$
L	0.9 m
h	0.05 m
T_u	313.15 K
T_l	283.65 K
Pr, Ec	$25, 3.3 \cdot 10^{-7}$

Table 4.1: Conditions evaluated in Turbulent 2-D Rectangular duct with Localized Constant Magnetic Field

In the publication of Tzirtzilakis, 5 cases regarding different localized magneto-static fields and magnetization flow parameters Mn_F and Mn_M gathered in Table 4.2 that will be definitely studied in this validation case.

4. Results

Case	B (T)	Mn_M	Mn_F
1	2	2.50	512.7
2	4	10	1025.39
3	6	22.5	1538.09
4	8	40	2050.78
5	10	62.5	2563.48

Table 4.2: Localized magnetic field induction and magnetization flow parameters to be studied

Overall, the magnetic fields evaluated will have different induced magnetic field B but its generalized shape, quantified with the gradient of magnetization will denote the region in which the flow will be severely affected by the FHD and MHD terms.

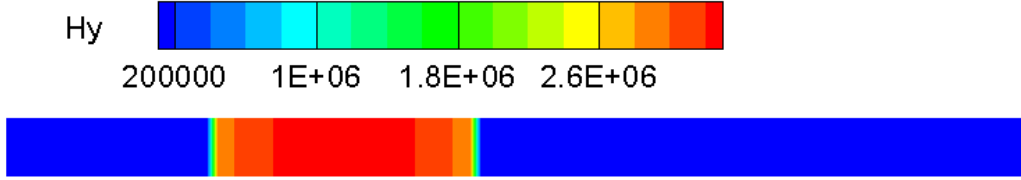


Figure 4.1: Application of the magnetic field with initial and final transition, and subsequent magnetization of the fluid

Figure 4.1 plainly shows the smooth gradient applied, given by the expression 3.7 is clearly sighted. Now, the results obtained with the code provided and the simulations from Tzirtzikakis [1] will be compared. Following the usual derivation, subfigures throughout the whole document are ordered from the weakest magnetic field applied (Case 1, B=2T) to the strongest (Case 5, B=10T).

· Stationary solution for Reynolds=400, Turbulent Case

The velocity magnitude contours for all the cases will be displayed in the following Figure 4.2, which will be logically accompanied by the X-Velocity and Y-Velocity plots in Figures 4.3, 4.4.

Regarding the velocity magnitude contours from plot 4.2, they evidence the proportional sensitivity of the present modelled blood to the localized magnetic field. The action of the MHD term is translated as a curvature in the blood flow whereas the FHD term does only

4. Results

take place due to the magnetic field gradient or transition (the finite expression detailed in 3.7). If the Hartmann flow was evaluated instead of the localized magnetic field problem, where the magnetic field is constant and uniformly distributed along the wole domain, the FHD contribution would logically not exist. The proofs of this statement, which are revealed by the equations in the previous pages, can be checked in literature [12], [18]. Moreover, Figure 4.2, apart from the proportional effect of B in the blood flow, does also introduce a perception which will be conveniently demonstrated in the following plots: vorticities will be onset and will also depend on B . They are direct consequence of the FHD contribution, thus, will be located at the regions in which the transition or gradient of the magnetic field intensity is present.

4. Results

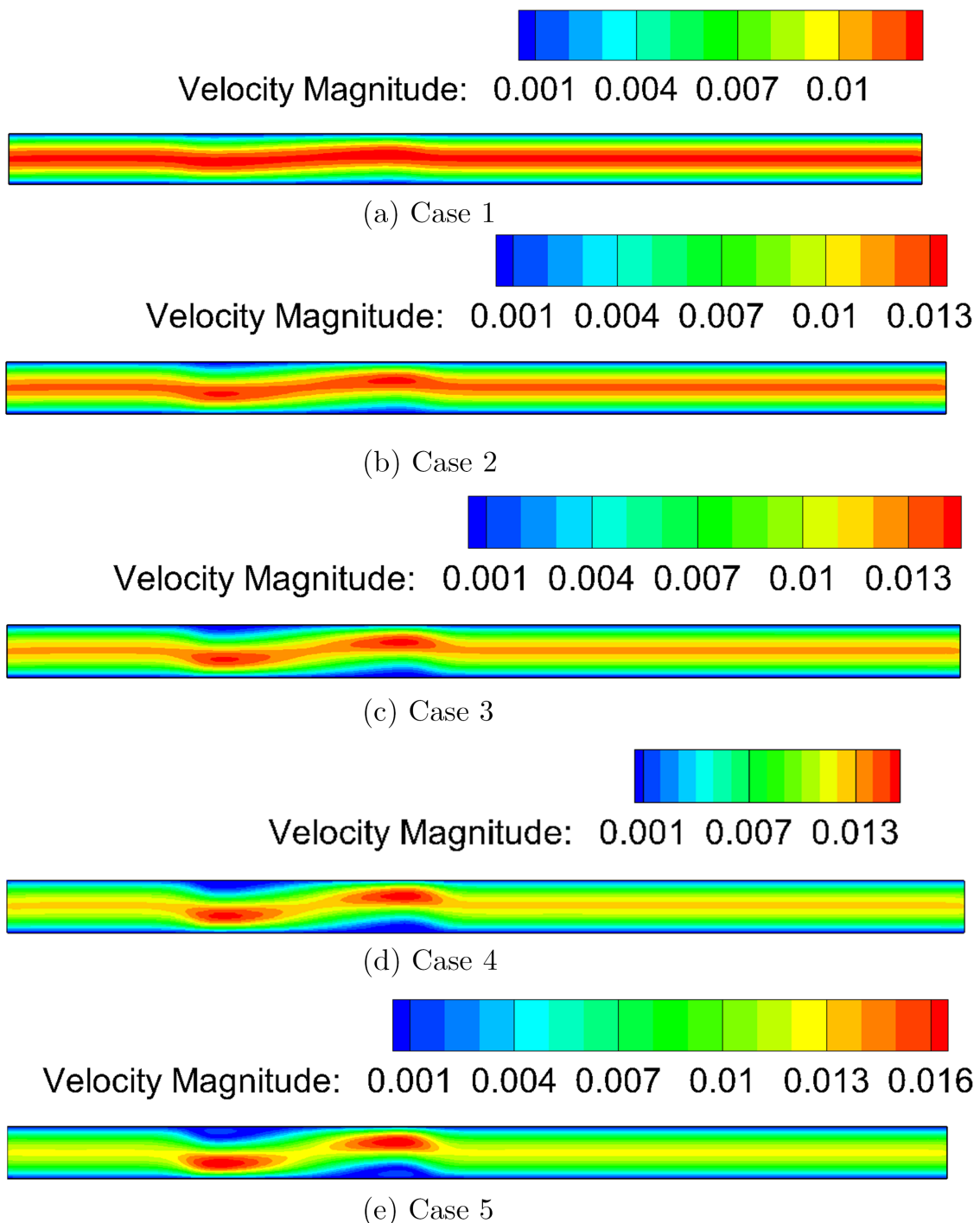


Figure 4.2: Velocity Results for different magnetic fields and Mn_M , Mn_F parameters, Re=400, Turbulent Case

4. Results

One must notice that the local extrema for all the cases are not set in the same scale, as they increase as the magnetic field is also increased. Whilst overall, as it has been reported by [12], the application of the constant magnetic field seems to reduce the axial velocity, in the magnetic transitions there's a significant acceleration that the blood flow suffers when it directly faces the two main vortexes. The first one, which will rotate counter-clockwise, will subsequently accelerate the flow in the proximity of the lower wall and, if it is strong enough such as in Case 5, will create a reverse flow are nearby to the upper wall (which, as it should be vectorially noted, can be sighted in Figure 4.3). Understandably, the second vortex will have the opposing effect: it will rotate in the contrary direction (clockwise), will accelerate the blood flow in the upper wall whilst will create a secondary reverse-flow - specially noticeable in case 5 - in the vicinity of the lower wall.

Even though all the results displayed result from a steady-state simulation, a transient simulations has been also carried out. The aim of it was to demonstrate that flow achieved a steady configuration as soon as the magnetic field was switched on. And consequently, this guess was confirmed. A transitory state from the inlet parabolic profile to the manners of the graphics displayed here did take place for a shorter period of time than a second, hence these steady results are correct. The author will be willing to provide these video files to anyone that would like to assess it.

The graphics of the velocity magnitudes in Figure 4.2 are backed up by the axis decomposition of the velocity in Figures 4.3 and 4.4. They serve to confirm all the statements gathered in this report. Besides, the X-velocity contour will evidence the apparition of a secondary reverse flow - in fact, two reverse flow zones- which is proportional to the magnetic field strength. This is why it is barely noted in Cases 4 and 5. Moreover, the Y-velocity contours of Figure 4.4 will show the response of the flow to the +Y - axis localized magnetic field. After the initial transition in which blood experiences a magnetization curve and in which the FHD throws the flow downwards, it follows the magnetic field induced direction as a result of the MHD behaviour. The values of it are almost 10 times lower that the x-axis flow, which is directly motivated by the Poiseuille parabolic profile in the inlet.

The Energy equation is at the same time solved along with the continuity and momentum equation, as the three equations are indeed coupled. The effects of the FHD and MHD momentum terms, when they are vectorially multiplied with the velocity in order to obtain the energy dissipation terms, are known as the Magneto-caloric effect and Joule effect. The evaluation of the intensive temperature value will evidence the contribution of these effects but also will introduce further slight details on the vortical structures predicted.

4. Results

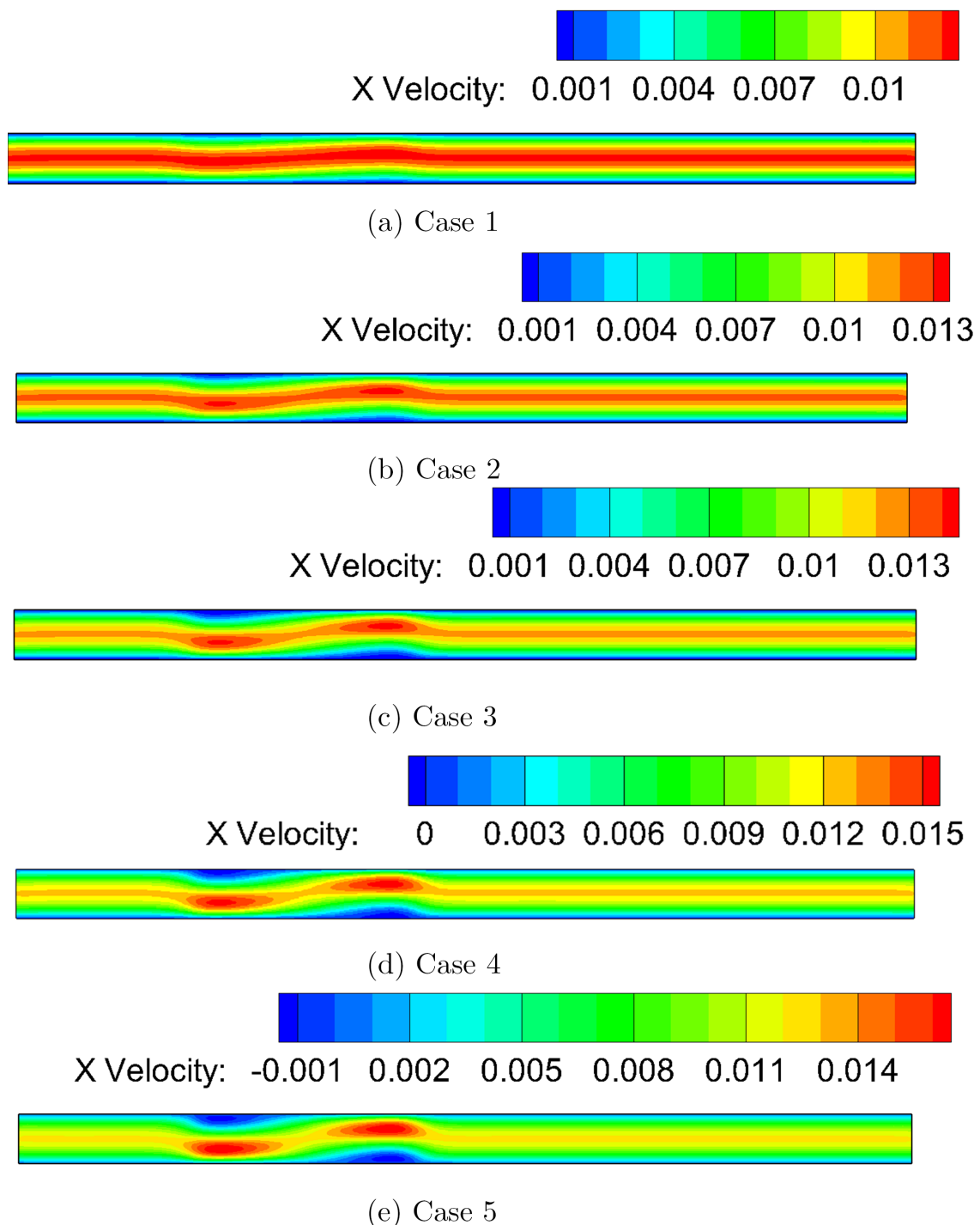


Figure 4.3: x-Velocity Results for different magnetic fields and Mn_M , Mn_F parameters, Re=400, Turbulent Case

4. Results

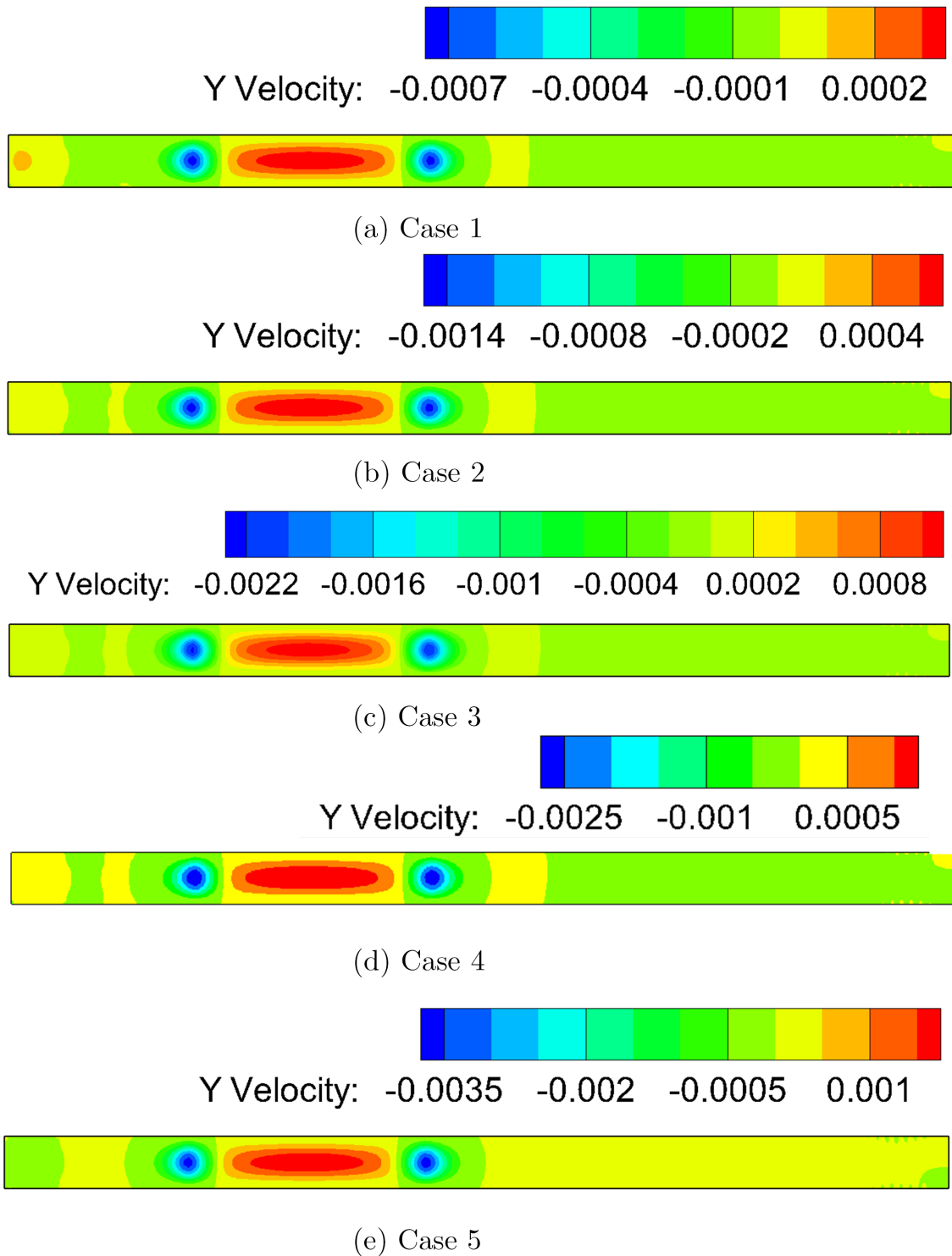


Figure 4.4: Y-Velocity Results for different magnetic fields and Mn_M , Mn_F parameters, $Re=400$, Turbulent Case

4. Results

Figure 4.5 reveals the Temperature contours of the blood flow for each of the cases. The magnetic field effect is evidenced as the greater value of it, the greater swirl is noted in the initialized gradient of temperatures. It must be said that, in this simulation, similarly to [1], the temperature field is decoupled from the velocity and they are not solved at the same time. This is why this graph could exhibit a linearized contour which might not take place in real simulations, but now we are indeed validating the code used. This phenomena will be further improved in the following sections. Also, the gradient present from the upper wall to the lower will facilitate to trigger the two vortices perceived, but will not imply an instability. The convective instability, which is known as the Rayleigh-Bénard problem, will only take place if the pipe is heated from below so that buoyancy forces and gravitational-viscous effects balance their contribution. This effect will be one of the strong evaluations of the present thesis.

The mixing phenomena which could definitely take place can be shyly sighted in the Case 5, where the induced magnetic field is about $B= 10T$. Even though in the outflow a linearized-ish profile is obtained, the maximum and minimum values induced by the boundary conditions in the upper and lower plates are not present. Due to this, an initial stage of mixing and diffusion is perceived. Conduction or convection seems not to be predominant enough against this effect, which carries the perturbation down stream. As a future work, the analysis of the propagation of the temperature field along larger sections of duct could be examined along with the parametric study of the influence of the height/length relationship.

So far, the results displayed in Figures 4.2, 4.3, 4.4, and 4.5 exhibit great consistence with the work of Tzirtilakis in [1] but also with the thesis of Kontantinou [90] and Adkins [91] from Cranfield University. The initial point to demonstrate was the impact of the electromagnetic static fields on blood but also to propose a more accurate model of its real-life nature, accounting for the MHD and FHD effects. Their influence is, as was expected, proportional to the magnetic field intensity but also on its gradient and on the gradient of temperature.

4. Results

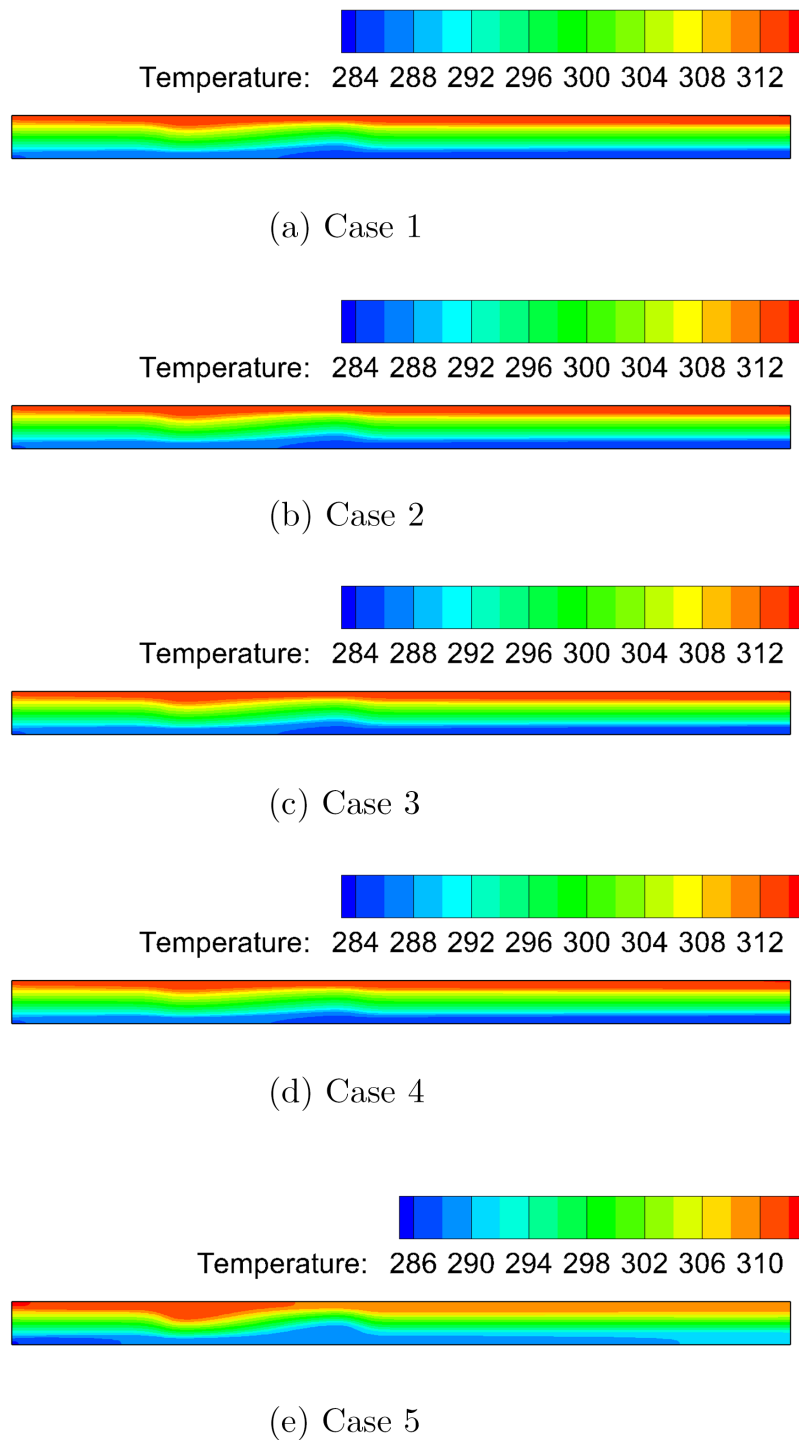


Figure 4.5: Temperature Contours for different magnetic fields and Mn_M , Mn_F parameters, $Re=400$, Turbulent Case

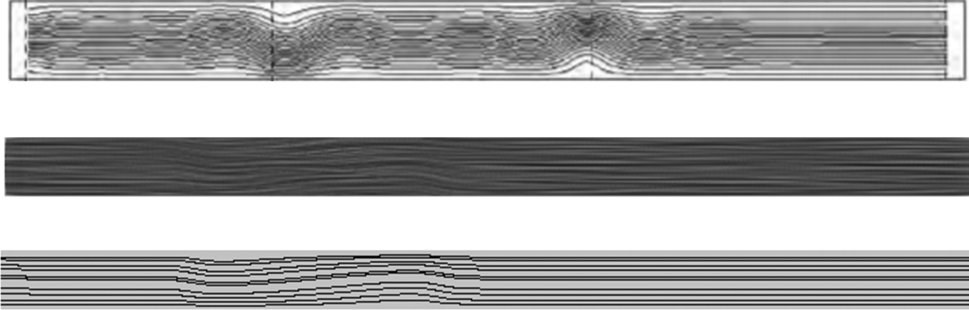
4. Results

The vorticities expected will be finally displayed in Figure 4.6 where only the weakest and strongest magnetic fields applied ($B=2T$, $B=10T$) are considered for simplicity. The intermediate cases do not redundant information as their results exhibit intermediate stages between both.

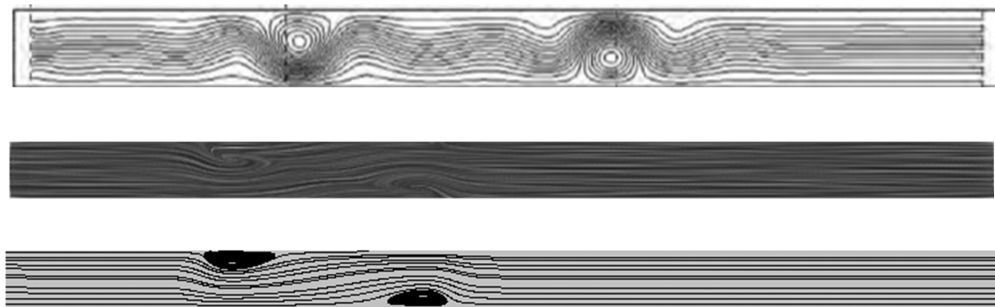
As it can be seen, by computing the streamlines or equivalently the stream function contours, the two vortices or "recirculation zones" are notoriously depicted. Their appearance is, as it has been described by Konstantinou, a consequence of the FHD term but also logically, with minor contribution- of the temperature gradient, which increases its magnitude. Their position is in the point of the magnetic field application and in the end of it, where gradients do take place. Z-axis vorticity is certainly proofing to be scaling with the intensity of the magnetic field applied. However, some differences in the morphology of the vorticities obtained in [1] and in our study have been reported. It is in fact due to the "L.L.I.M" algorithm , widely known as "line-by-line" applied by Tzirtzilakis, which calculates the solution for a streamline and then moves it upwards in the spatial domain. This approach is indeed weak in terms of reliability and does commit some imprecision in the prediction. Such methodology provides with a nicely-rounded vortexes but they lack of accuracy to real ones, which should be better represented by our graphs. The fact that these vortices are not considered as strong -which is due to the limited magnetization curve of "homogeneous" mono-phase blood-, their shape is conditioned by the inlet velocity thence their elongated shape.

The choice of presenting the results obtained through two different contours - one achieved by using the Post-Processing ParaView Software and the other graphed with Tecplot- is because of the different traits that they simultaneously demonstrate. Even though the Tecplot streamlines evidence with higher strength the two vortexes obtained - and actually is the main program used to withdraw the flow variable contours presented - the ParaView result confirms the rotatory direction of the recirculations. Hence, with two different methodologies, we have confirmed and presented the same phenomena.

4. Results



(a) Case 1 ($B=2T$). Upper image: Results from [12]. 2nd and 3rd image: streamlines obtained respectively through ParaView and Tecplot.



(b) Case 1 ($B=2T$). Upper image: Results from [12]. 2nd and 3rd image: streamlines obtained respectively through ParaView and Tecplot.

Figure 4.6: Streamlines comparison with Tzirtzilakis [1] for Cases 1 and 5

As it has been demonstrated, the results presented in this validation case are in good agreement with what has been documented in [1], [90] and [91]. Basically, the blood mathematically modelled shows a special sensitivity to the external static magnetic field, being this influence proportional to the value of the magnetic field. Due to the existence of the magnetic field, the MHD term does exists and will curve the flow in the same direction of the magnetic field applied, but also by slightly diminishing the axial velocity. However, if the magnetic field is not present in the whole domain (which is the Hartmann problem) and it is localized, a finite gradient of the magnetic field will be present in the beginning and end of the magnetic field. Ferromagnetic flow -such as blood due to the presence of erythrocytes and charged ions- will react to this phenomena by introducing two contrarotatory recirculation zones or vortices in those transitions or gradients. Therefore, flow will suffer an acceleration in those points. These vortices, which are not considered energetically strong, will be more easily triggered if a gradient of temperatures is also present, which has been our case. Given these traits, the conclusion of the validation case

4. Results

is satisfactory and hence the methodology developed in this study is totally accurate.

These have been the main flow characteristics noted and summarized in this short paragraph. But it could imply some additional consequences in the health field where steady magnetic fields are used in techniques such as in MRI devices or Magnetic Drug Targetting. As it can be derived, even though the investigation has been totally mono-phase, blood is formed by a wide variety of elements, and therefore some additional effects take place in real experiments. The vortices disturb the parabolic inflow creating recirculations and stagnation points. These effects of changing velocities, is critical as due to the blood density, the roleaux effect can be onset and derive in blood clots, which are prone to cause fatalities when they are delivered to the brain. These effect will be sensitive to the magnetic field applied but also in the blood parameters, being the most relevant its density, the Reynolds number, the height of the vein/artery but also in the haematocrit and LDL/HDL concentration. Knowing this, and being aware that 0.2 T to 5 T are normally applied in MRI devices, but they can reach 15 T usually employed in animal investigation and testing, the use of such devices when flow conditions are not optimal entail an evident health threat.

4. Results

4.2 Non-Newtonian Model Investigation

Blood, as it has been reported in experimental investigations but also thoroughly detailed throughout the whole document, possesses a clear shear-thinning behaviour especially notorious at low shear regimes and small vessels. In previous chapters we have stated the need of simulating with Non-Newtonian models, which have been the ones selected to be simulate the 2-D channel duct and the reasons behind this choice. Moreover, in the appropriate section, a complete description and mathematical formulation for each of the models has been provided.

The first corner stone in which Non-Newtonian models differ and that inherently affects the solution is in the definition of the effective viscosity. In Newtonian models, it is assumed to be constant and represented by the dynamic viscosity μ , which, in case of blood [14] is set to $3.2 \cdot 10^{-3}$ N s/m². Thus, for the Newtonian case the effective and dynamic viscosity will be considered the same. The other Non-Newtonian Models will have a different definition of the effective (or apparent) viscosity depending on its parameters. This is why, in Figure 4.7 we will represent for each of the models the curve of the effective viscosity against the shear rate. As it can be perceived, low, medium and "high" shear rates have been represented so as to see their performance through different regimes.

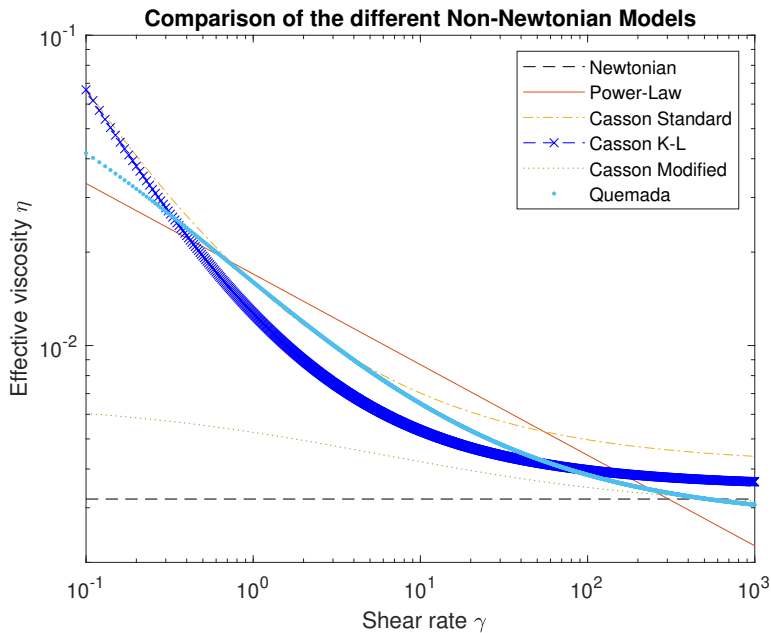


Figure 4.7: Comparison of effective viscosity against shear rate for the Non-Newtonian Models

4. Results

Figure 4.7 demonstrates each of the Non-Newtonian model's effective viscosity response to the shear rate. The format of the picture is vectorial ("eps") so that any desired zoom can be made without loosing any apex of sharpness. All the model's slope, even Power-Law are curved and asymptotic-ish to the Newtonian value when the shear rate tends to infinite. This is why, it is stated that the Newtonian approach is sufficient enough to describe blood flows at high shear rates. The apparent impression of the fact that Power-Law is a simple straight line comes from the fact that both X and Y axis are represented logarithmically, hence the logarithm of a "constant" power-law implies this visual effect. One should notice that Casson-type, Power-Law and Quemada emerge similarly at low shear rates, whilst the Modified Casson has a sharper proximity to the Newtonian model. This is due to the introduction of the relaxation time parameter (λ), hence one should try to use this method for higher shear rates.

In the medium range of shear-rates, Casson and Casson-KL models behave practically with the same shape and inclination, but Quemada and specially Power Law has more conservative slopes, which could be barely described with a linear function. In this same Regime, the Casson-Modified is still located in between these models and the Newtonian, being in the same deviation from the Casson-type that actually the Power-Law is, which represents the higher effective viscosity values of the set.

In the late and high shear rates, they all tend to the Newtonian model, with some special deviation noted in the Casson Standard, but which was expected and consistent with what [4] reported. On the other hand, the effective viscosity is totally under-predicted by the Power-Law model, which is logical on its simple form as it is detailed in the Theory Fundamentals. Power-Law does not possess a mechanism to stop the descendent rate of viscosity for high shear rates and make it tend to the Newtonian constant value. This is why, certainly, one should try to avoid this model for simulating in high shear rates.

Once the effective viscosity behaviour definition is compared, the results predicted by each of the Non-Newtonian Models will be presented in the following pages. The same operating and boundary conditions employed at the Validation case in the previous section will be simulated (whose results were obtained using Power-Law), but now only the Case 5 in which the magnetic field applied $B=10T$ will be considered. This is why, it is recommended to revisit the setup from 4.1. However, for this case it has been essential to solve the temperature and velocity field coupled, hence we had to perform some minor changes in the UDF. Otherwise, artificial results were achieved. First, the velocity magnitudes and components for the Newtonian Case will be plotted, but will also be accompanied by the contours of temperature, vorticity in Z-Axis and by the

4. Results

streamlines which will evidence the presence and shape of the vortices. The rest of the Non-Newtonian models will follow this case with the same structure of plots.

4.2.1 Newtonian

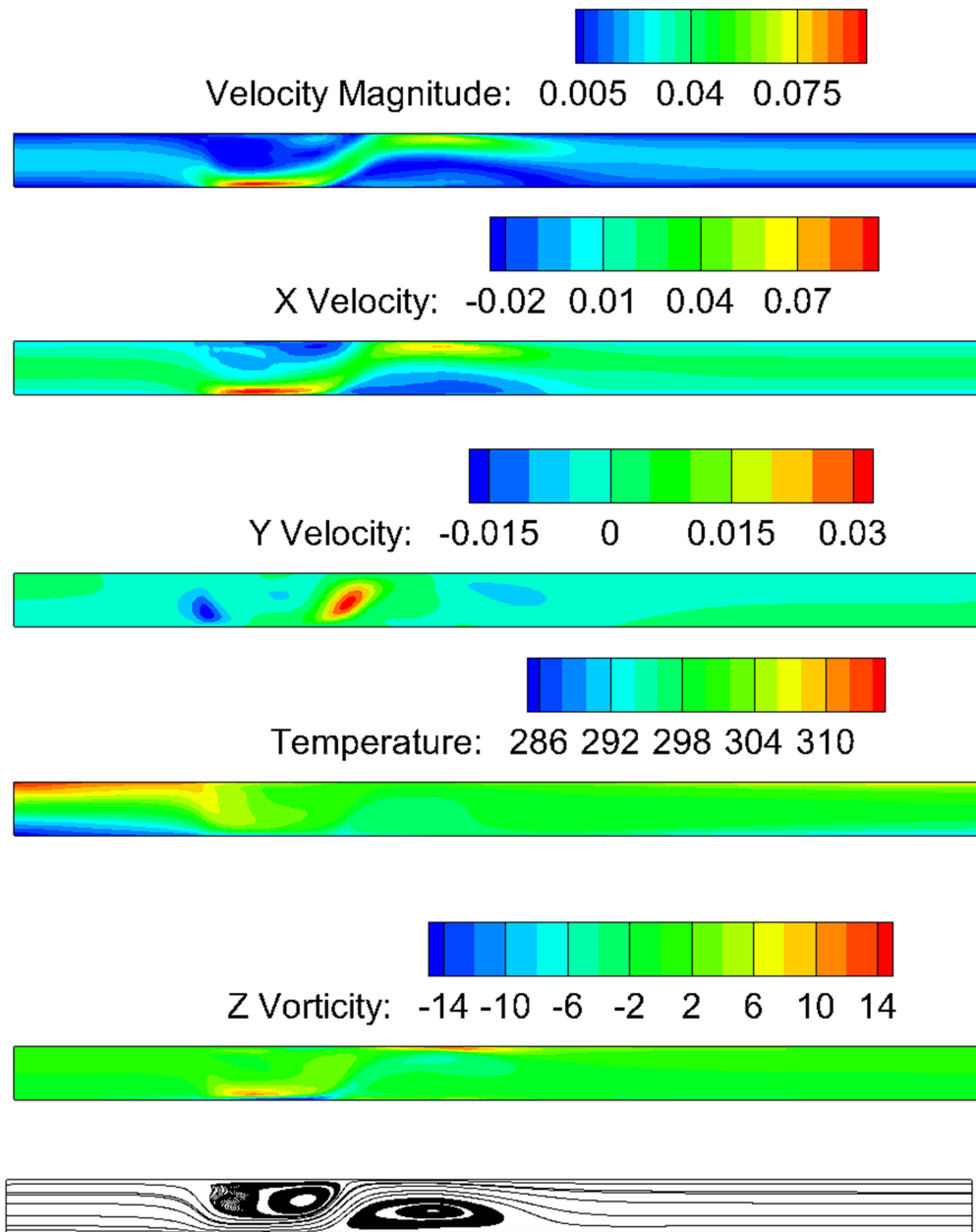


Figure 4.8: Results for the Newtonian Model, $B=10\text{ T}$

4. Results

4.2.2 Casson

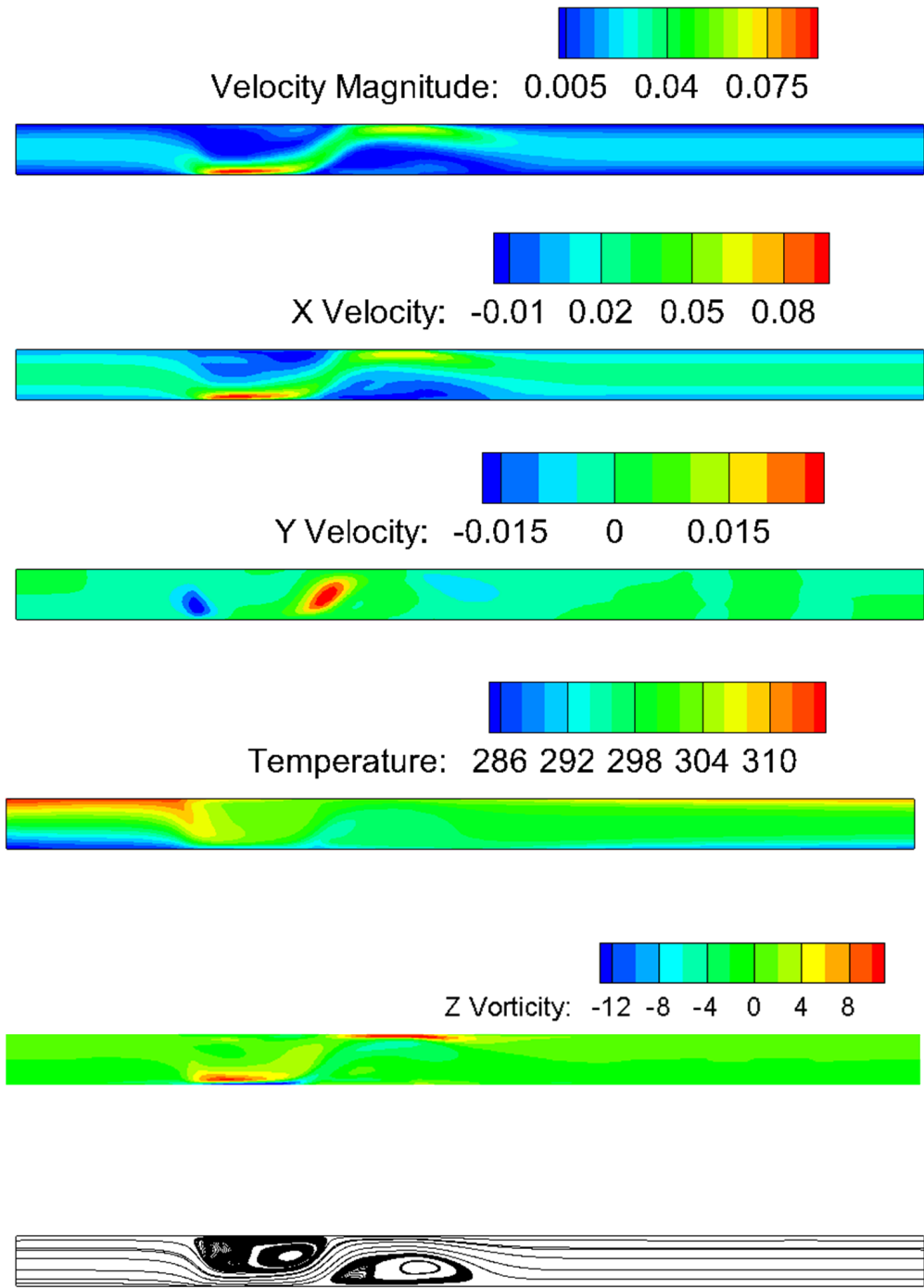


Figure 4.9: Results for the Casson Model, $B=10$ T

4. Results

4.2.3 Modified Casson

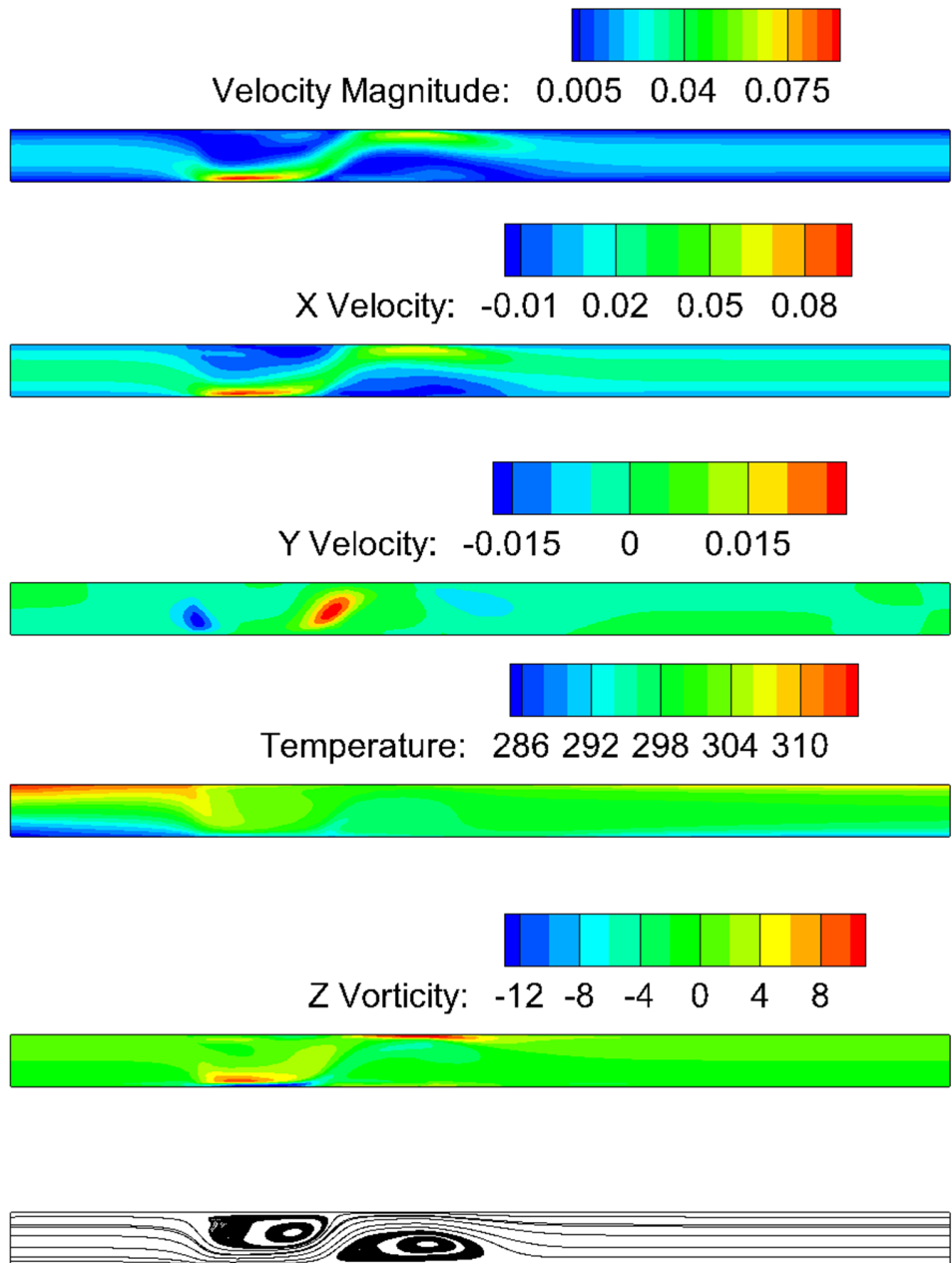


Figure 4.10: Results for the Modified Casson Model, $B=10$ T

4. Results

4.2.4 Casson-type K-L

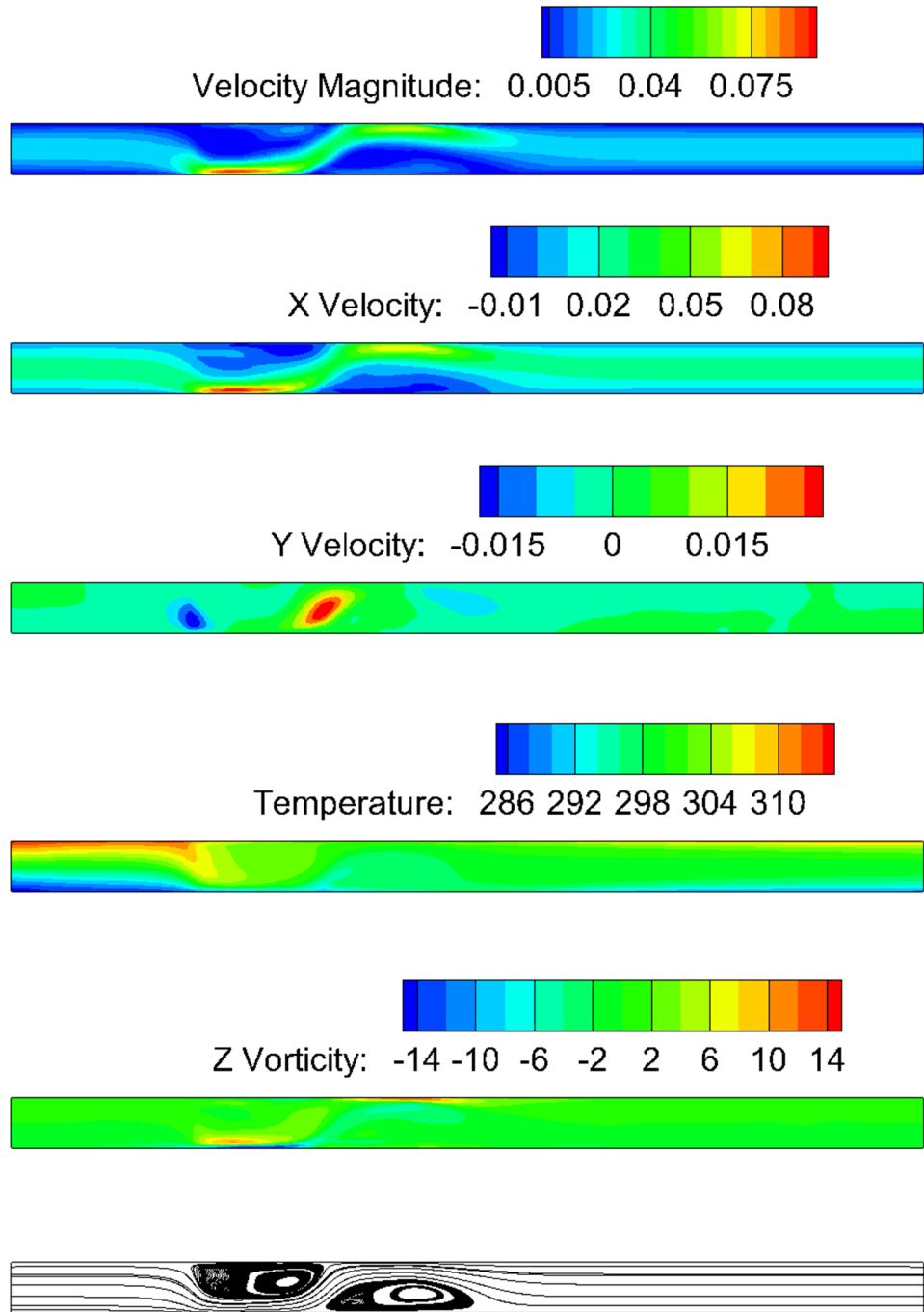


Figure 4.11: Results for the K-L Casson-type Model, $B=10$ T

4. Results

4.2.5 Quemada

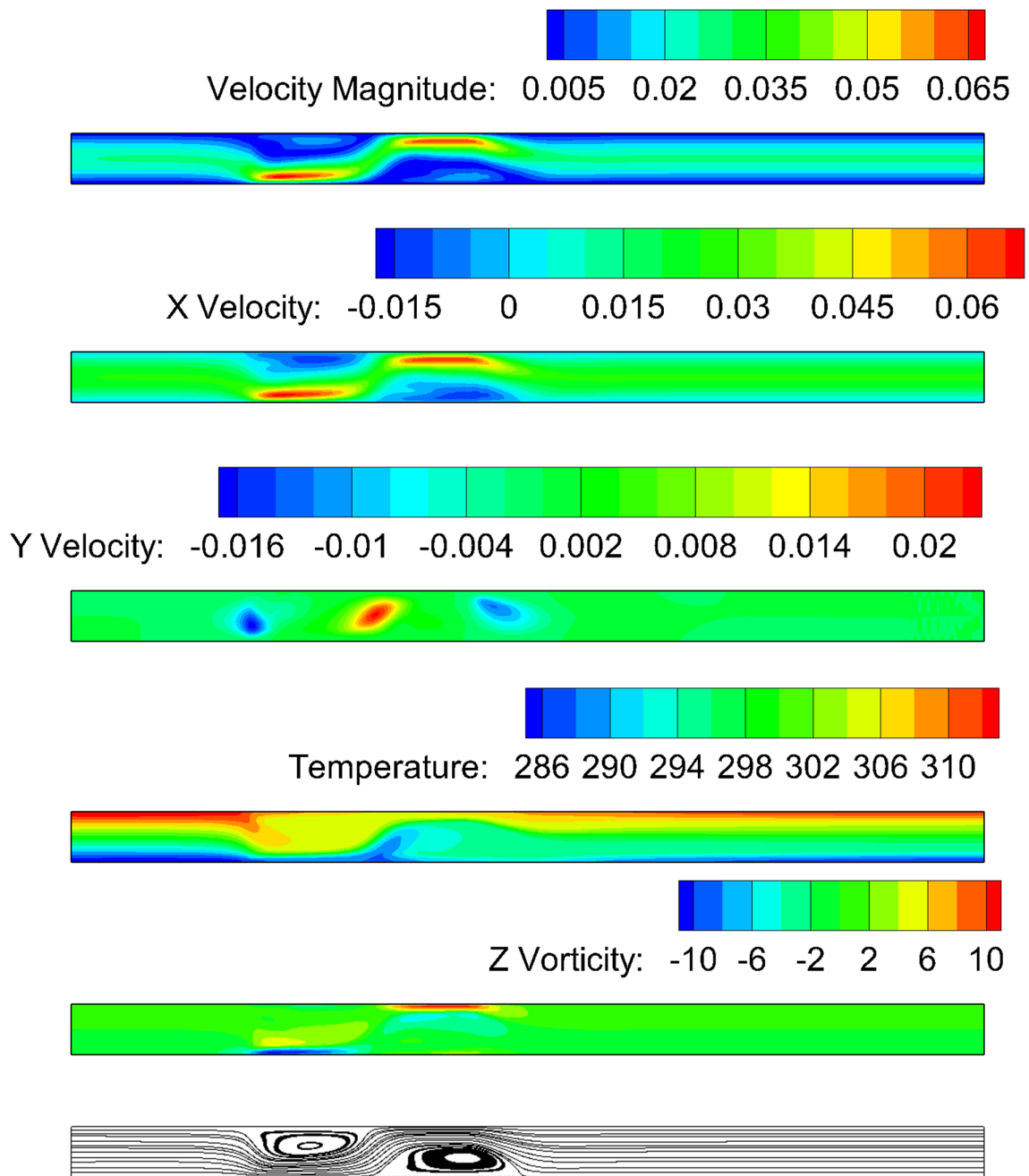


Figure 4.12: Results for the K-L Quemada Model, $B=10$ T

4. Results

Overall, except from the Quemada model, the Newtonian and Casson family of Non-Newtonian model (Normal, K-L and modified) demonstrate particularly similar contours. At the same time, they demonstrate some common traits with the results from the Validation Case in which the Power-Law was used (Figures 4.2-4.6) but with different values and with not so symmetric and "good looking" consequences. However, given the deductions made on Figure 4.7, the bad performance of Power-Law given by [13] and [4] and the fact that these "reliable models" show small deviations from one another, one should consider wisely these last plots. Also, the coupled velocity and temperature field provides reliability and solidity to the solution.

In all the results -even though in the Quemada model it is not so intense- a clearly mixing phenomena takes place. It is more evidenced in the temperature plot, where conduction and convection after the first vortex do not seem to have great impact: the temperature field is practically homogeneous. As it has been said, the results of Figure 4.12 are not that homogeneous and a "linearized" temperature profile is starting to develop due to heat transfer largely after the two vortexes perturbation (region of localized magnetic field).

Some minor differences can be also devised in the contours of the velocity magnitude, as Newtonian and Casson-type Models predict higher acceleration of the fluid in the core of the first vortex while the effects on the 2nd are smoother. This concrete conclusion is not shared by the Quemada model, which determines that the influence and strength of both vortices is approximately the same. Regarding the results, the Quemada model seems to be located as a middle solution between the Power-Law behaviour and the rest of the models. Nonetheless, this prediction is caused by the bigger X-Velocity profile considered by the model, since for the Y-Velocity all the plots look considerably alike. This trait of the velocity profiles will be reviewed in the following pages, particularly at Figure 4.13 and its posterior discussion of results.

Regarding the vorticity plot for all the models, it seems that values are relatively equal, however, the gradient is slightly bigger in the case of the Quemada model. This will logically introduce higher Shear Stress on the walls, which is known by the variable acronym WSS.

The structure of the vortices evidenced in the streamline plots describe the same shape, location and intensity of the vortices due to the FHD effect, which is consistent with what was obtained in the Validation Case. Now, once consistent results have been achieved and the flow variables predicted have been generally commented, additional insights such as Velocity Contours at particular sections and WSS will be further analyzed.

4. Results

4.2.6 Comparison of the Velocity and WSS Contours

The axial velocity profiles, which are a consequence of the spatial advance of the inlet parabolic "Poiseouille" function, have been obtained at the strategic locations of $x/h = 3, 3.5, 4, 5, 7, 8$ and 13 in order to visually determine - with more efficiency- the effects of the Non-Newtonian models. As it can be seen, these locations will imply the regions: before the first vortex, inside the first, immediately after, then between both vortexes, a more detailed slope of the 2nd vortex and the flow facing the outlet.

The representation of all these "slices" and subsequent velocity profiles has been graphed in Figure 4.13 in the following page. Overall, the shapes of the velocity profiles for all the sections is consistent and accordant. However, important deviations with the Power-Law model have been noted, while some minor with the Quemada model at certain x/h locations are also present.

The difference with the Simple Power-Law is due to the inaccuracy of this model to describe the shear-thinning behaviour of the blood flow, as it has been detailed in previous explanations, even though the idea regarding this model is simple and original. This is why, enhancements of this model have been done resulting in the Generalized Power-Law expression given in 2.49. Overall, Simple Power-Law Model predicts less intensity of the flow in the Axial direction and less remarkable influence of the recirculation zones or vortexes. Additionally, it exhibits an additional resistance to change the parabolic-flow shape introduced in the inlet, or to be perturbed. Thus, it will imply the largest deviation from the other models, which show almost in-existent differences from one another.

On the other hand, some minor variations have also been noticed in the Quemada model, which considers some bigger values on the X-axis velocity. Besides, for the inlet and outlet velocity, the profile is less blunt than the other models, which is somehow a little bit contradictory with what one could expect with a model which shares more traits than the others with blood multi-phasic properties. As it has been reported in [45] one of the most characteristic effect of the multi-phase flow is the blunt velocity profile. However, we understand that this minor disparities do usually take place. Given this reason, the effects of the vortices will not be so extended in the Y direction as the other Newtonian and Casson models describe. Apart from this little differences noted, the overall performance is correct and the results are all consistent.

4. Results

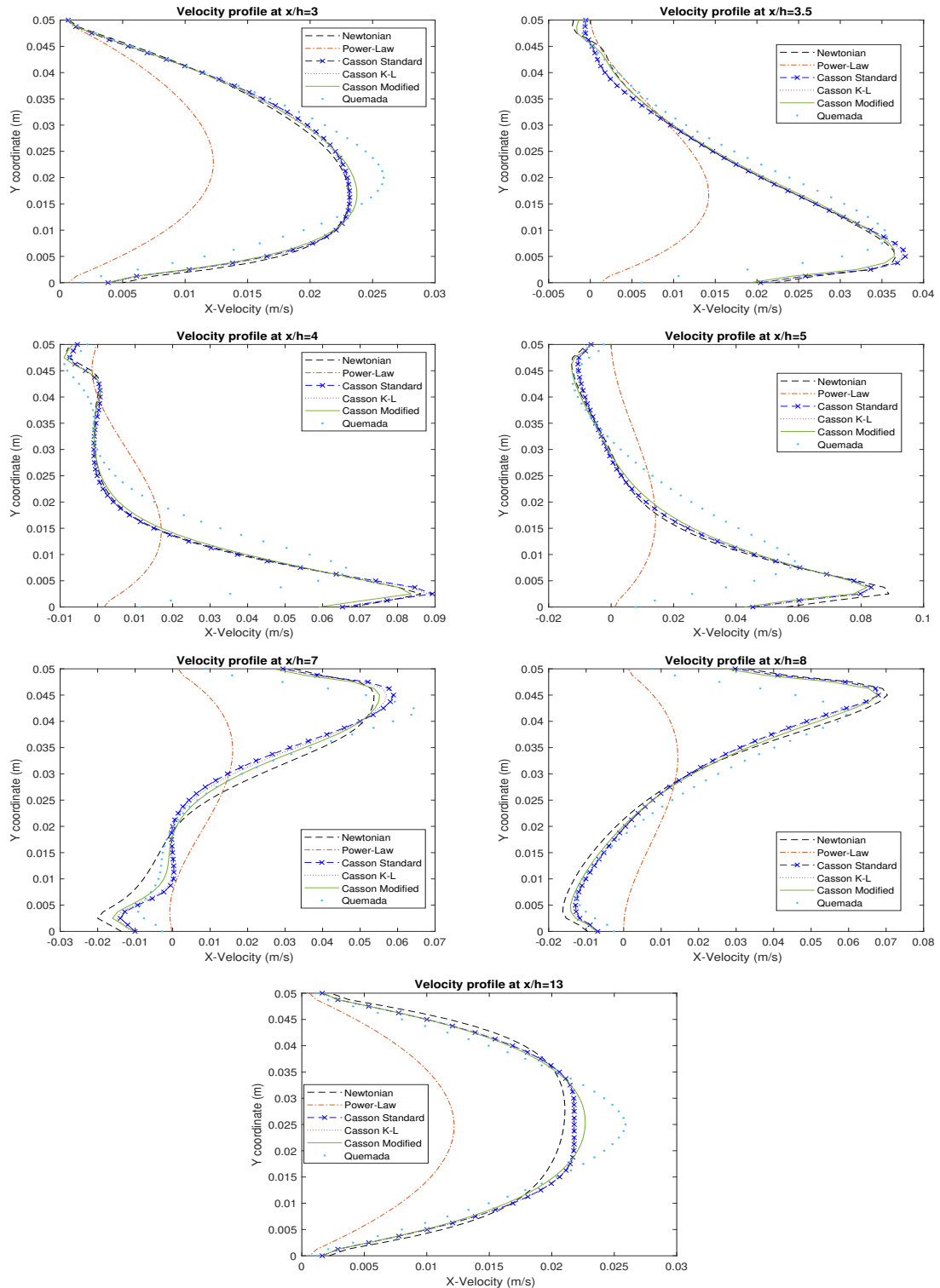


Figure 4.13: Velocity profiles for the different Newtonian and Non-Newtonian Models, at different sections along the x axis

4. Results

Regarding a practically indistinguishable trait perceived in the plots -specially focusing in $x/h=7$ - Casson-type models show more sensitivity of the fluid to the non-linear phenomena, adopting more curvature at certain points. The model in which this trait is more notorious, from the 3 that practically are equal to the Newtonian model (Casson, Modified Casson, and K-L) is the KL model. Apart from this, it is surprising that the Modified Casson model, even though its performance noted in 4.7 for medium and low shear rates- is practically equal to the other Casson-type. Consequently, one could think that we are currently operating in high shear-rate regimes.

Moreover, an statistical error study on the velocity magnitude is intended at certain strategic locations. These have been $x/h = 3$, $x/h=7$ and $x/h=13$. Since we do not own an analytical, experimental or "correct" result from which we compute the errors through the compact L Norms, we will calculate the deviations from the Newtonian model. Please note the importance of using the "deviations" word instead of errors.

Variable	Norm 1	Norm 2	Norm Inf
Power Law	0.007985	8.0754 e-05	0.0136
Casson	4.56 e-04	3.68 e-07	0.0015
Modified Casson	5.21 e-04	4.44 e-07	0.0017
Casson KL	3.74 e-04	2.44 e-07	0.0012
Quemada	0.002085	7.413 e-06	0.0062

Table 4.3: Non-Newtonian Deviations from the Newtonian Model at $x/h=3$

Variable	Norm 1	Norm 2	Norm Inf
Power Law	0.0183	5.2347 e-4	0.0456
Casson	0.0051	3.292 e-5	0.0095
Modified Casson	0.0031	1.2916 e-5	0.0056
Casson KL	0.0042	2.344 e-5	0.0080
Quemada	0.0061	7.0545 e-5	0.0239

Table 4.4: Non-Newtonian Deviations from the Newtonian Model at $x/h=7$

4. Results

Variable	Norm 1	Norm 2	Norm Inf
Power Law	0.0080	6.91293 e-05	0.0101
Casson	9.4 e-04	1.0784 e-6	0.0018
Modified Casson	0.0011	1.5996 e-6	0.0019
Casson KL	8.7 e-4	9.224 e-7	0.0016
Quemada	0.0026	8.5240 e-6	0.0049

Table 4.5: Non-Newtonian Deviations from the Newtonian Model at $x/h=13$

Overall, Tables 4.3, 4.4 and 4.5 demonstrate quantitatively what we already know: the model which shows bigger deviation from the Newtonian model is the Power-Law and then, by approximately 1/4 of this difference, the Quemada Model. The two models that have shown less difference to the reference have been the normal Casson and the Casson K-L, fitting one best at a certain point whils the other does it for a different x/h . The insignificant values from Norm 2 imply the fact that deviation occurs in rather little points than systematically distributed along the whole domain, as in this case the quadratic deviation would be bigger than Norm 1. At last, Norm Inf shows the maximum deviation present in the samples between the reference Newtonian model and the analyzed one. Besides, apart from the region where vortices occur which demonstrates the biggest disparity, the "outlet" selected region seems to slightly imply less deviations rather than the inlet. This effect could be caused by the mixing smooth region depicted specially in the temperature plots.

An idea that [92] remarked was the importance of evaluating the WSS contours at different moments if a transient study did take place in order to detect in advance the aparition of underlying medical conditions such as the fatal atherosclerosis. This is why, the WSS in the top and low duct walls will be included in Figures 4.14, 4.16 and 4.15 .

Figure 4.14 demonstrates, for the Newtonian Case and magnetic field applied ($B=10T$), the different wall shear stress slopes for the Upper Wall (Red) and Lower Wall (Blue). As it has been deduced from Figure 4.8 the lower wall presents a more intense vortex core hence the subsequent WSS will be higher. The axial position (measured along the x-axis) of both peaks from both slopes is consistent as well with the effect and position of the vortexes. Even the influence of the contrary and far vortex is sighted.

Now, in graphs 4.15 and 4.16 the effects of the Non-Newtonian models will bw compared.

4. Results

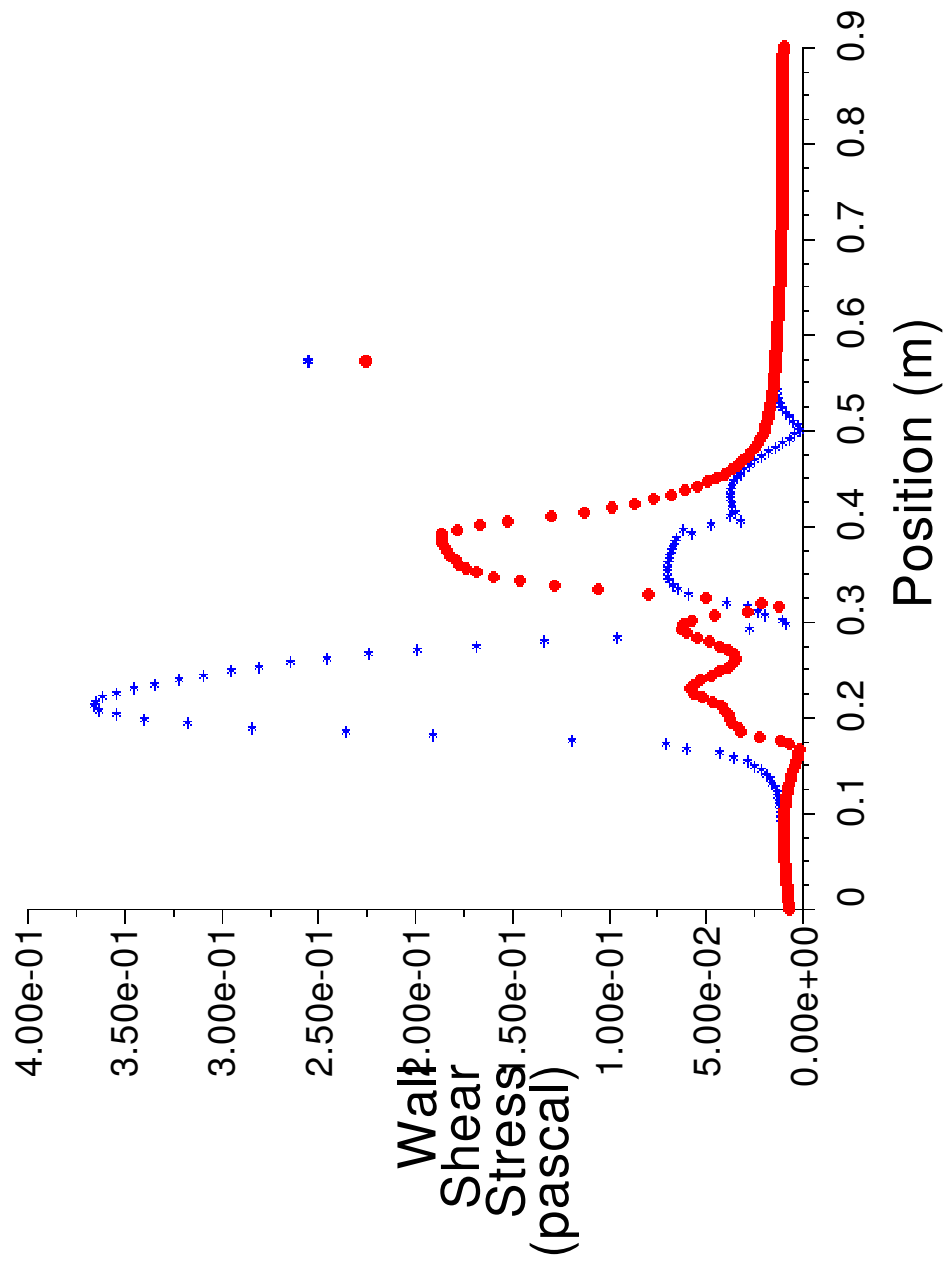


Figure 4.14: WSS Curves for the Newtonian Case, $B=10T$. Red: Upper Wall, Blue: Lower Wall

4. Results

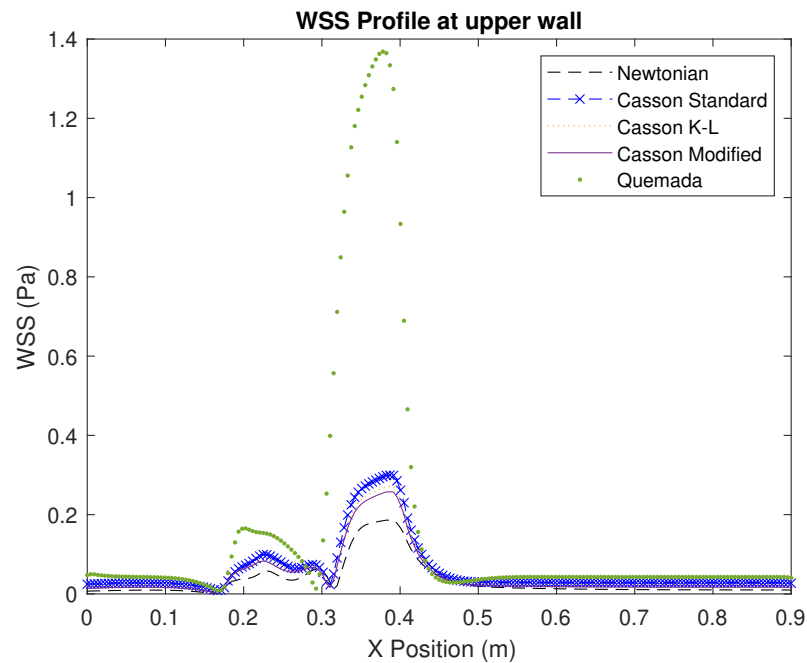


Figure 4.15: WSS Distribution in the Upper Wall for the Non-Newtonian Models, B=10T

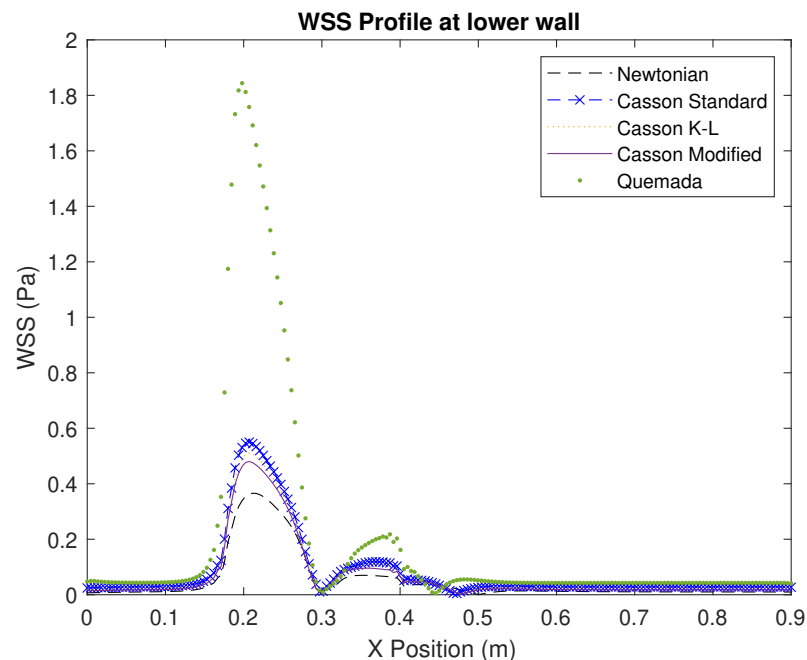


Figure 4.16: WSS Distribution in the Lower Wall for the Non-Newtonian Models, B=10T

4. Results

Both figures withdraw apparently the same conclusions hence they will be commented in general. The Newtonian model accounts for the lowest WSS prediction, whilst the Casson-type are practically grouped around the same values which are slightly higher than the Newtonian (with a maximum deviation of 150 % of the Newtonian in the peak). In the other hand, the Quemada model triples the values of the Casson model at its peak, where the maximum deviation is perceived, having consequently a stronger and notorious deviation in the WSS curve. This difference, for high-shear rates, is normal given the differences of the Non-Newtonian models and one should not worry about it, as the WSS is directly proportional to the viscosity. The Non-Newtonian models, thus, should normally deviate remarkably from the Newtonian slope. It is curious to notice this graph and the less difference noted in the velocity plots seen in previous pages, manifesting the need of analyzing and comparing the relevant flow parameters completely.

4. Results

4.3 Magnetoviscous Contribution

The presence of a magnetic field introduces a change on the RBC: they get polarly oriented with a particular angle regarding its normal ("perpendicular") flow and the magnetic field direction. This effect is translated as an additive viscosity to the base-line viscosity, as it is evidenced in [2]. Logically, the impact or effect of this phenomenon will be proportional to the magnetic field intensity but also on the RBC velocity and acceleration.

Tzirakis et al, in [18] derives a semi-empirical expression to model the magnetoviscous contribution. Knowing that the relationship between B, H and M parameters can be simplified by using the α parameter which is

$$\alpha = \frac{1}{\mu_0} \frac{\chi}{(1 + \chi)^2}, \quad (4.1)$$

then, the apparent viscosity can be calculated with the expression of:

$$\eta_{app} = \mu [\alpha + \beta H + (1 - \alpha)e^H] \quad (4.2)$$

where H is the magnetic field intensity, and beta an experimental parameter that will accompany α . The similarities between 4.2 and 2.12 are not merely casual as the expression above is derived semi-empirically. Results from [2] obtain the numeric values of $\alpha = 0.9986$ and $\beta = 0.01425$. They conclude that up to a 11.5 % variation can be perceived depending on the flow regime, which is approximately the same condition reached by Tzirtzikis et al.

The study of the contribution in our flow case will be applied, considering μ as constant (Newtonian Model). The same conditions from 4.2 will be evaluated, with a localized magnetic field induced of $B=10T$ in the usual position. If the effective viscosity without the additional term is plotted, one obtains the following graph.

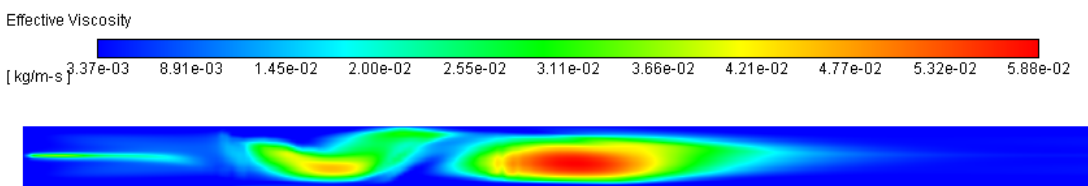


Figure 4.17: Effective Viscosity for the Newtonian Case, $B=10T$

Afterwards, the UDF code has been modified in order to consider 4.2 with the values of H_y . The results obtained after initializing the solution with the inlet Poiseuille velocity

4. Results

profile and including the magnetoviscous additive term or real effective viscosity provide Figure 4.18.

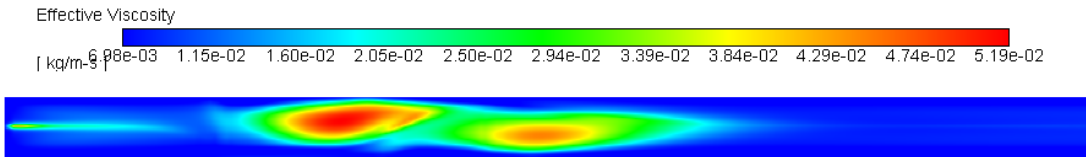


Figure 4.18: Effective Viscosity with the Magnetoviscous Contribution, $B=10T$

An evident difference between both Figures 4.17 and 4.18 is perceived in the prediction of the viscous term contours. Whilst in the Newtonian Case a stronger effective viscosity is detected in the second vortex, with the additional magnetoviscous contribution both vortexes have a more balanced strength, which was totally expected. In fact, a slight higher influence is recognized on the first vortex core of Figure 4.18. This could be explained if one realizes that once the effective viscosity is perturbed the gradient to create a higher change should be higher, not constant as it is, thence the stronger impact of the first vortex.

Besides, a generalized change in the local values is also devised. Even though there's a sensitive change in the localized minimum extrema (of about 43 %) with greater values when the magnetoviscous contribution is switched on, the local maximum extrema is surprisingly higher in the Newtonian case by almost a 11.5 %. Hence, some deviations of around 10 % of the values have been obtained depending on the coordinates of the flow, which is consistent with [18].

Now, the Wall Shear Stress Contours in both Upper and Lower Walls will be plotted in Figures 4.19 and 4.20 due to the curious phenomena that they present. Even though, in most of the flow variables the effect of this magnetoviscous term is barely witnessed, in the WSS distribution there's a difference of almost a 50 % with the Newtonian model. Although the mean values predicted are slightly higher, the effect of the vortex is underestimated in contrast with what is obtained in the Newtonian Model. This is mainly due to the difference in the maximum values shown in the previous figures where the effective viscosity was analyzed, where up to approximately 13 % of variation between each models was witnessed. The lack of WSS experimental research publications with Non-Newtonian flows under FHD-MHD effects similar to the here simulated hardens the process of validating results and also to establish extremely solid deductions.

4. Results

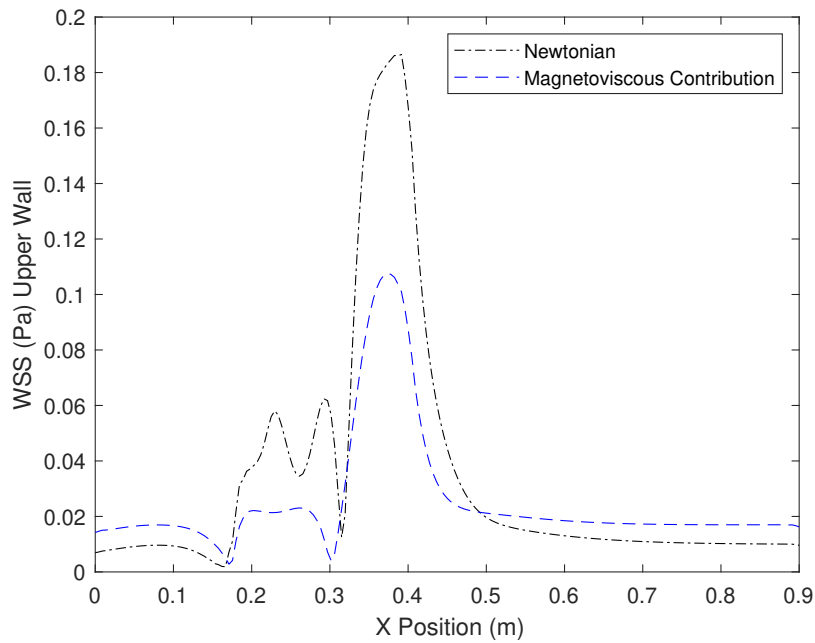


Figure 4.19: WSS Contour along the Upper Wall for the Newtonian and the Model with the Magnetoviscous* Additional Contribution

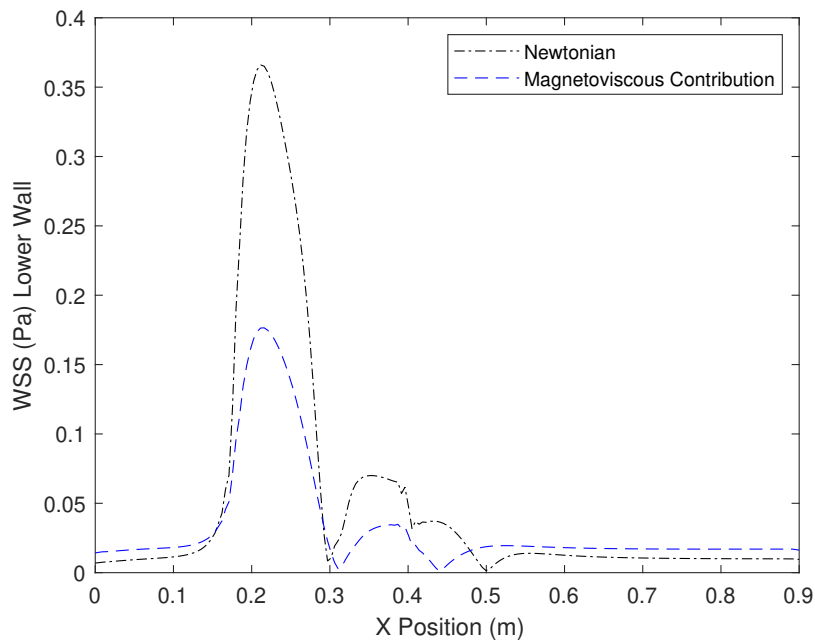


Figure 4.20: WSS Contour along the Lower Wall for the Newtonian and the Model with the Magnetoviscous* Additional Contribution

4. Results

By considering the values of the deviations presented, similar conclusions might be withdrawn from the Tzirakis did run a study of a pulsatile blood flow while the approach used here is considering a constant parabolic velocity profile inlet, which could provide remarkable differences depending on the systole-diastole cycle. However, one should attend that the erythrocytes instant orientation will also vary depending on this inlet cycle thence the model 4.2 would not be longer solid. Due to this, given the scope of this thesis, it is left as a future work to carry out: the effect of the additive magnetoviscous contribution with pulsatile flows by improving the expression 4.2.

4. Results

4.4 Pulsatile Velocity Inlet

In the previous sections, the velocity inlet is assumed to be spatially distributed parabolic flow where the maximum velocity is located in the center of the duct, which is actually known as a parabolic flow. The details on the inlet have been already provided. However, if the time domain is yielded, it is assumed to be constant. Depending on the geometry: vein or artery, their physical dimensions and location in the human body, the velocity inlet will vary in time as a result of the heart pump. This period is known as the systole-diastole cycle. In the systole phase, the heart muscle is contracted in order to pump blood to the aorta and pulmonary artery, while diastole represents the relaxation of the heart and will allow the blood coming from cave and pulmonary veins get introduced in the cardiac chambers. This is why, in the Systole movement or stage the maximum pressure (120mm Hg as reference value) is achieved albeit in the diastole phase the minimum will be reached (80 mm Hg).

Even though this conditions could be implemented as pressure inlet BC, they can be equivalently treated in terms of velocity. This is why, here the pulsatile blood flow will be implemented via UDF as the velocity inlet. The shape of the cycle can be simplifiedly described by using sinusoidal functions such as in [18], However, in this present document a more detailed and trustworthy detailed is aimed.

In order to obtain the high-fidelity model, the shape of a real electrocardiogram in the aorta is used and represented in 4.21.

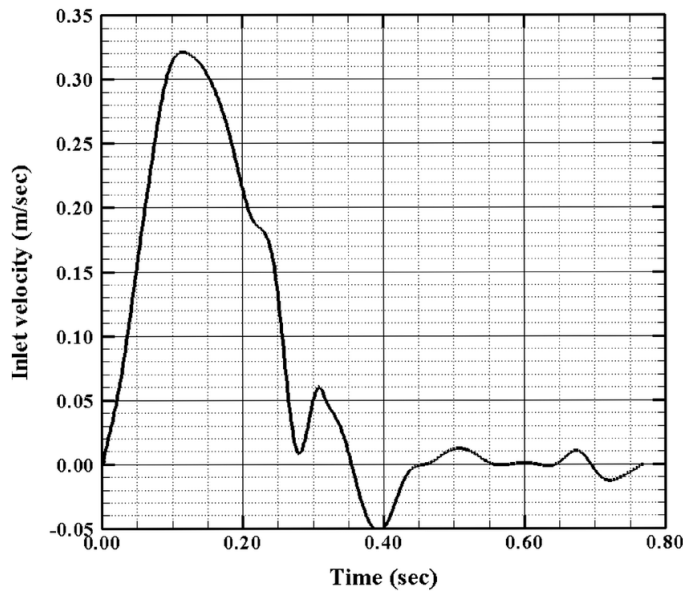


Figure 4.21: Velocity Waveform in the Aorta. Source: [5]

4. Results

Strategic points from this graph are extracted using Digitizer Software and then a polynomial regression function of 50th order is computed in order to force the expression to pass through all the strategic points. With this function, one could model the aorta model, however, using so many terms is not efficient and not solid in terms of numerical instabilities. This is why, this polynomial function is used to create further points that do describe the plot perfectly, to then run a proper Fourier Analysis and obtain the harmonics that perfectly fit -in terms of series- the velocity waveform in the Aorta. In fact, many harmonics have been devised so then an optimized study by splitting the plot in pieces and then imposing continuity in their boundaries has been rather performed. In the end, a truly high-fidelity Aorta Inlet velocity model has been obtained such as it is demonstrated in Figure 4.22.

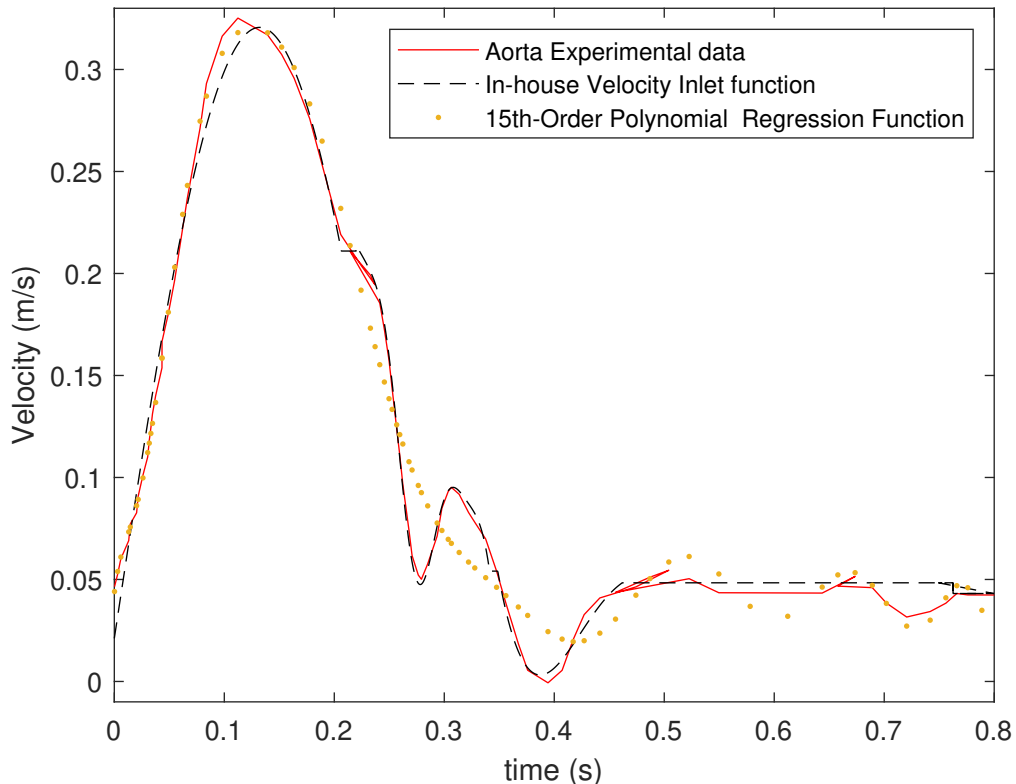


Figure 4.22: Pulsatile Velocity Inlet Model

It seems that, this function is far better descriptor of the Aorta waveform than the investigations reviewed so far and its formula will be attached in the Appendix Section for 2-D and 3-D cases for any researcher who would like to use it. Surprisingly enough, very little models have been publicly revealed in publications hence the author of this document releases its

4. Results

mathematical description.

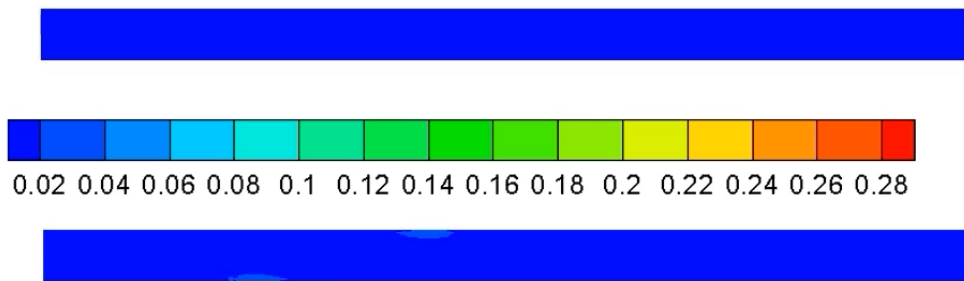
For terms of comparison, the Aorta Experimental Data is represented (red contour) along with the results from our model (black discontinuous curve) and a 15-th order polynomial regression obtained by LSS of the Experimental Data, which, even though it could be considered as high order enough to be reliable, results from Figure 4.22 demonstrate its relative inaccuracy to describe the waveform.

Once this model is successfully developed, it is implemented as velocity inlet and coupled with the 2-D spatial parabolic profile in order to represent the geometric and time evolution of the blood flow. Then, the blood flow is simulated with the same conditions from 4.2 with and without implementing the MHD/FHD source terms. By doing this, a more realistic simulation of the effect of this phenomena is described considering a vessel with relative spatial proximity to the Aorta. It is evident that some minor differences but also least velocity amplitude will be devised as much as we separate from this main artery.

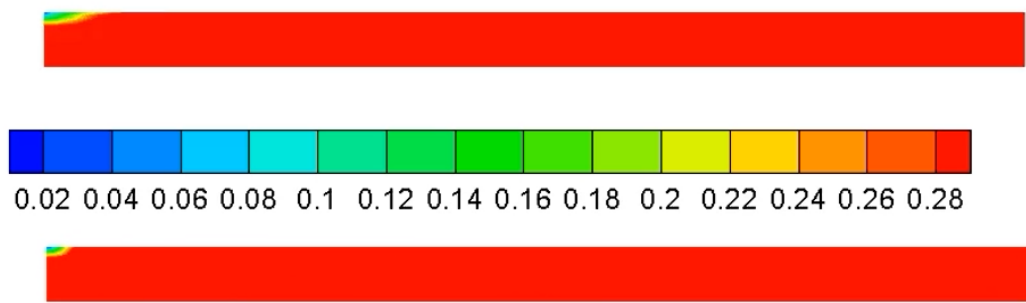
Now, in Figure 4.24 the velocity magnitude contours of the transient simulation will be represented at the static time steps of: initial time, systole peak (maximum), diastole peak (minimum), and relaxation time (between diastole and systole). For each time step, two images will be provided; in the upper figure the pure blood flow will be simulated while the lower image will consider the FHD/MHD contribution with a localized magnetic field of $B=10T$. Furthermore, an image after 3 periods will be also provided to determine if the evolution in time implies any remarkable effect in the blood flow.

Logically, the maximum velocity will be obtained in the systole peak, at a time $t=0.1s + 0.8*k s$, being k an integer number. No significant differences are noticed between both cases (pure blood flow and MHD/FHD), only a slightly less intense velocity magnitude region in the upper corner when the pure blood is simulated. However, it is not considered to be a remarkable merit. Such conclusion cannot be equally said in the diastole minimum point of the cycle ($t=0.4s + 0.8*k s$) as an important change in the velocity magnitude is noted. This trait noted is reasonable as the FHD term requires a minimum residence time to magnetize the blood flow and trigger the vortices. Its influence -as it could be thought- will be specially noted as much steady and "slow" the axial velocity is. Apart from this phenomenon, no major differences can be derived from both plots.

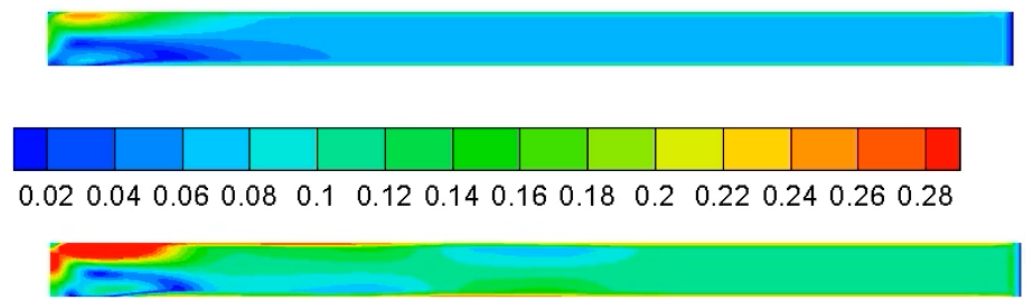
4. Results



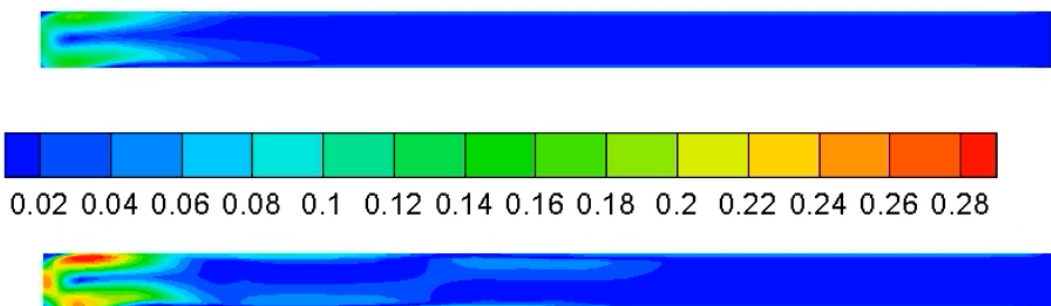
(a) Velocity Contours of Pulsatile Flow, $t=0$ s. Above: No Effects. Below: FHD/MHD, $B=10T$



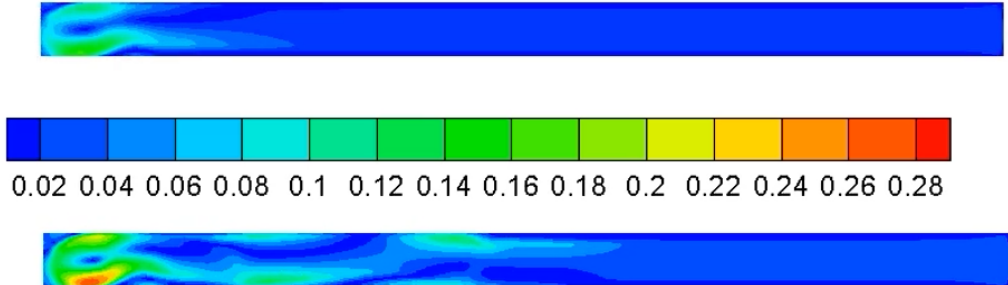
(b) Velocity Contours of Pulsatile Flow, $t = 0.1$ s. Above: No Effects. Below: FHD/MHD, $B=10T$



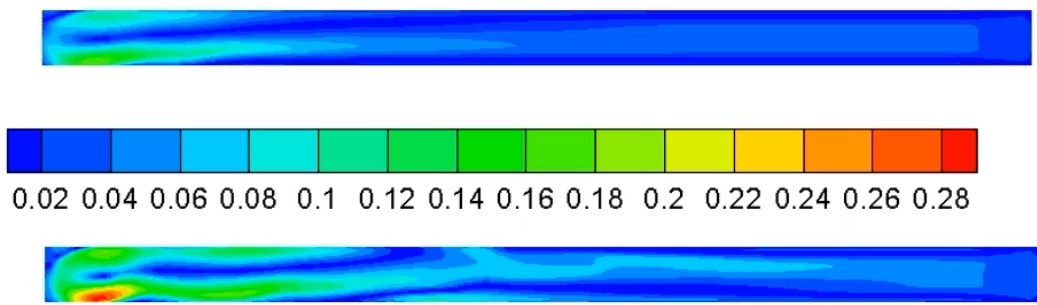
(c) Velocity Contours of Pulsatile Flow, $t = 0.4$ s. Above: No Effects. Below: FHD/MHD, $B=10T$



4. Results



(a) Velocity Contours of Pulsatile Flow, $t = 0.75$. Above: No Effects. Below: FHD/MHD, $B=10T$



(b) Velocity Contours of Pulsatile Flow, $t = 0.75$ s + 3 periods. Above: No Effects. Below: FHD/MHD, $B=10T$

Figure 4.24: Transient Simulation of Pulsatile Velocity Flow. Evaluation of the FHD/MHD effect

Following the Idea that the FHD term requires a "more or less" steady axial velocity to fully magnetize - see the hysteresis curve 2.2 - the erythrocytes, its contribution will be mainly noted in the relaxation time where velocity remains more or less constant. This range is located, according to Figure 4.22, between the late 0.45 and 0.8 s of each period. Interestingly enough, the FHD/MHD plots predicts higher values velocity magnitude values, with the formation of two tiny vortex cores. Initially, the upper vortex core is more energetic, but as time goes by, the dissipation acts on the blood flow and it feeds the second vortex, which gets indeed stronger until $t=0.8$ s, where the heart pump is triggered. The impact of the MHD and FHD events are less powerful than the ones noticed in the steady simulations seen before (Velocity inlet constant in time domain). This conclusion was expected since the velocity pulse variations completely sweeps the apparition of any vortex core in the rectangular duct (RBCs barely get magnetized). Hence, one could deduce that the greater the vessel and the higher its proximity to the heart (or subsequently to the aorta) the lower the FHD/MHD effect will be onset.

4. Results

Another interesting insight acknowledged is the time dependence of the blood flow: results are not strictly equal at each period. More than 12 continuous periods have been simulated and the difference in the velocity magnitude flow variable has been perceived. An example of the noted variations has been attached in Figure 4.24, where the flow at $t=0.8$ and at the same point after 3 periods has been illustrated. Apart from the variations that are indeed appreciable, the overall effect does not seem to keep developing: it slightly changes but with overall similar values. This difference of the values variating from one period to another, might be visible but it is not considered to be significant or strong enough.

A more in-depth investigation could be provided by analyzing the different flow variables such as in 4.3 where x-velocity, y-velocity, temperature, z-vorticity and streamlines were plotted yet also yielding the effects of B depending on its value and consequently the different non-dimensional parameters Mn_F and Mn_M were studied. The results from different Non-Newtonian Models such as in [13] and [18] could be also evaluated. And, obviously, the implementation of the additional magnetoviscous contribution is an interesting aspect to further review. However, given the limited time and resources of this investigation, this procedure is left to the future and here the overall effects of the pulsatile flows on the FHD/MHD implementation, regarding a closer study of the reality than [1] and [12] is performed.

4. Results

4.5 Rayleigh-Bénard Convective Instability

The Rayleigh-Bénard effect is a convective instability that takes place when buoyancy forces, as a result of the lower-layer heating and temperature difference between the two boundaries in which the fluid is confined, get stabilized with the gravity forces. An exchange between conduction and convection is setup as the main heat transfer mechanisms. When this convective instability is driven, the apparition of characteristic Convection (or also known as Bénard) cells in the whole domain -this feature is not strictly true since, as it will be seen, it will mainly depend on the temperature gradient- with contrarotatory spins from one another. Given the easiness to produce this result but also bearing the availability of a reasonably solid analytical solution that can be withdrawn from the linear stability analysis (and even a weak-non linear analysis such in recent investigations [30]), this effect is usually studied for a variety of flows and boundary onsets. This is why, a shear-thinning modelled fluid, specially blood, will be investigated under this special instability.

As an initial result, a simpler model of the blood than the ones studied above will be created and tested. The geometry to study is the same 2-D duct, with a Length of $L=0.9$ m and a height of $h=0.05$ m. Accordingly, $L \gg D$, which is one of the main assumptions to develop a R-B Convective Instability (from now on, RBI). It is important to mention the fact that, as it has been mentioned before, the instability is driven by the contrary effects of buoyancy and gravitational forces (triggered by temperature gradient) hence the gravitational force will be considered. Some publications argue that gravity is not strictly necessary for the onset of this instability, but then the Rayleigh control term would lose its meaning and a sensitively higher gradient of temperature would be therefore necessary. Consequently, the gravity acceleration of $g=-9.81$ m/s² in the Y-direction will be taken into account. The duct is assumed to be strictly perpendicular to the gravity force (hence perfectly horizontal), but if the vessel was vertical as the aorta or any other main arteries/veins, this contribution would logically have no impact on the RBI.

4.5.1 Tzirtzilakis Conditions

Now, the common and main values representing the condition of the blood flow will be gathered in Table 4.6. Two of the main values that directly dictate the onset of the instability, the temperatures of the upper and lower walls, will not be included as they will logically vary regarding each case studied (the convection will strongly depend on the dissipation, velocity inlet, and much other variables).

4. Results

Flow parameter	Value
ρ	1050 kg/m ³
g	-9.81 m/s ²
c_p	14.286 J/(kg K)
k	0.61 W/(m K)
μ	0.001003 Pa/s
Thermal expansion coefficient (α)	0.000257 (1/K)
thermal diffusivity (a)	$5.083 \cdot 10^{-6} \text{ m}^2/\text{s}$
T_{inlet}	250 K

Table 4.6: Flow Condition Values for the Simulations of Blood in a 2-D Rectangular Channel. Investigation of Rayleigh-Bénard Instability.

Once presented the common values for the blood flow setup, the specific conditions to be simulated under the Turbulent and Laminar cases will be described in the following lines.

4.5.1.1 Turbulent

A significant difference is noted in the morphology of the Bénard convection cells when turbulence contribution is introduced. Because of this, the non-linearity of the set of equations is predominant and chaotic structures evolving in time have been detected experimentally [93]. The analytical solution presented by [28] and the weak non-linear from [30] and [23] is not so far valid. Hence, the first thing to evaluate is the Laminar solution, whose scope is mathematically treatable. However, given the flow properties, here will be mainly noted as turbulent diffusion which will fade in time the instability onset. The turbulent model which has been is the k- ϵ realizable, being probably the most implemented model in CFD simulations due to its high performance in describing mean and boundary flow.

The velocity inlet cannot be set as high as it was for the normal blood flow as simulations have demonstrated that it totally sweeps out the convection effect. The time of residence of the fluid is so little that buoyancy forces do not have time to push the fluid upwards. Thence, the constant-in-time dimensionless velocity u/u_{max} from the inlet parabolic profile is set to 1/10 of its value, so that $U^* = 0.001$.

The difference of temperature between the upper and lower walls have been given the respective values of $T_u = 320K$ and $T_l = 390K$ so that it fully exceeds the theoretical Rayleigh number (Ra of the simulation is approximately 5.68E+05 while the theoretical critical Ra is about 1707.8) to ensure the convective instability. In fact, regarding the Ra formula, a difference of temperature smaller than 0.2105 K must be present between both

4. Results

plates in order to make $\text{Ra} < 1707.8$ and do not consequently trigger the instability. Once all this setup is done, a transient simulation is performed and the following structures in the flow variables have been obtained.

4. Results

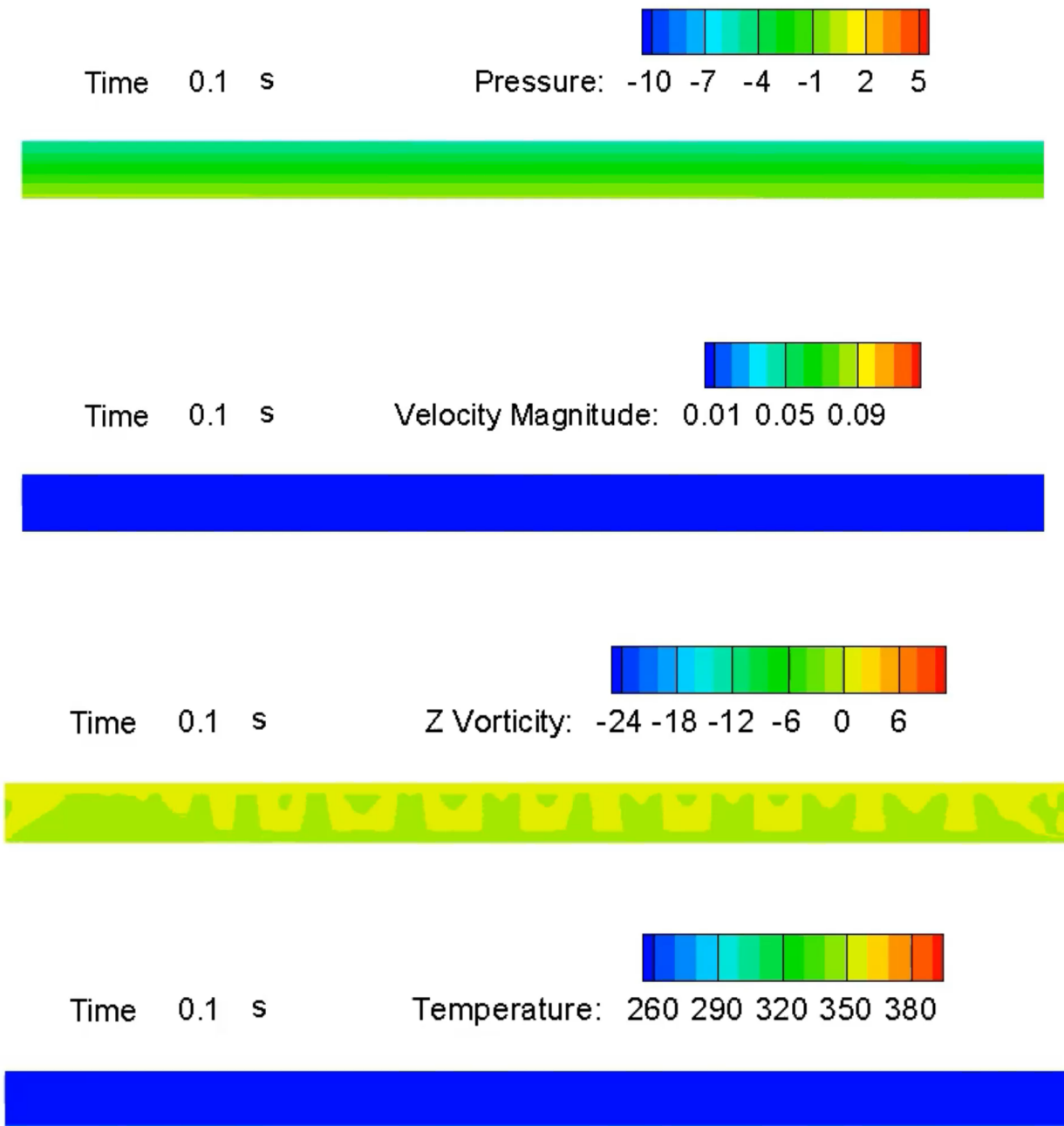


Figure 4.25: Transient Simulation of Rayleigh Bénard Instability, $t=0.1$ s. Laminar Case

4. Results

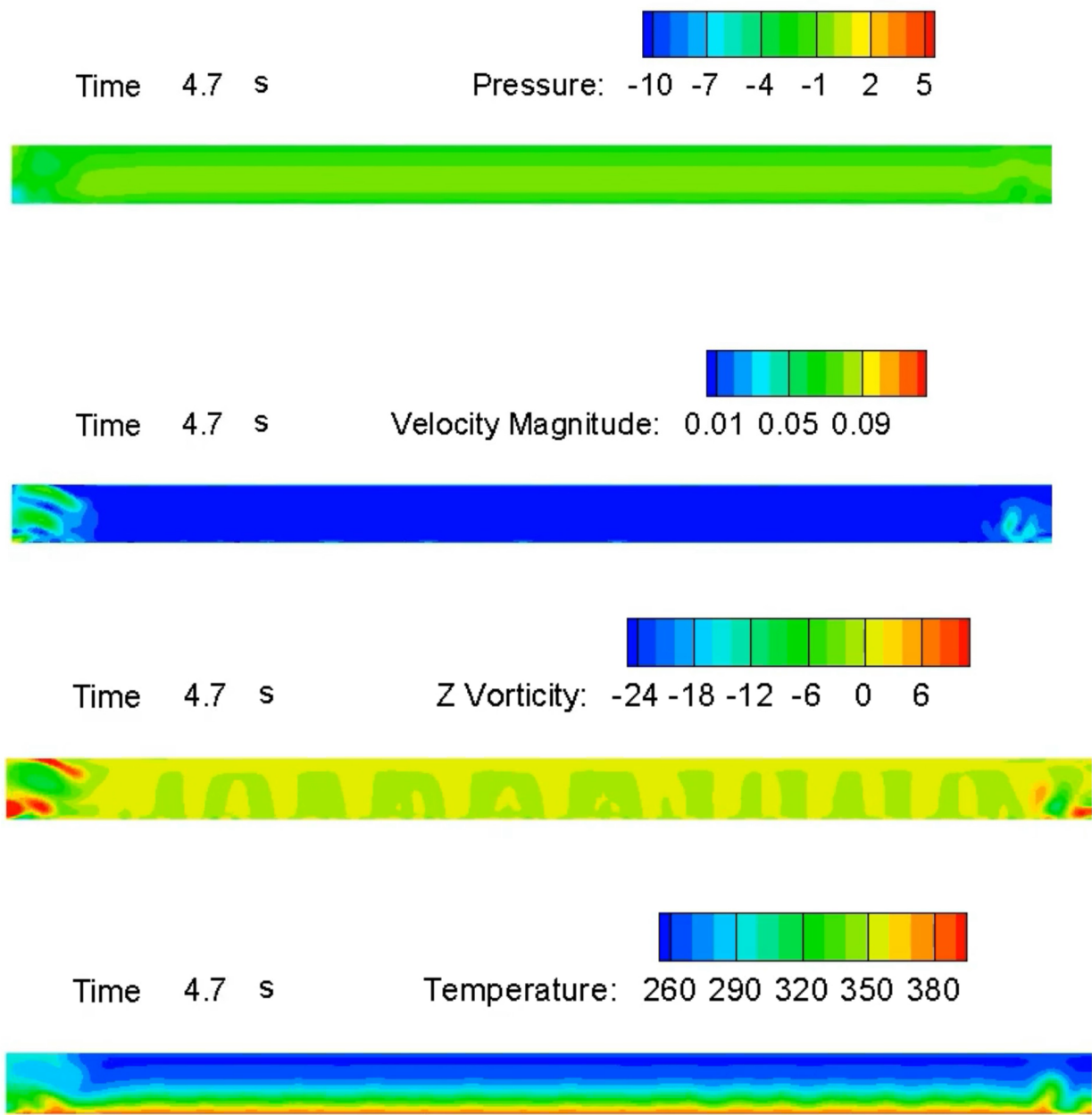


Figure 4.26: Transient Simulation of Rayleigh Bénard Instability, $t=4.7$ s. Laminar Case

4. Results

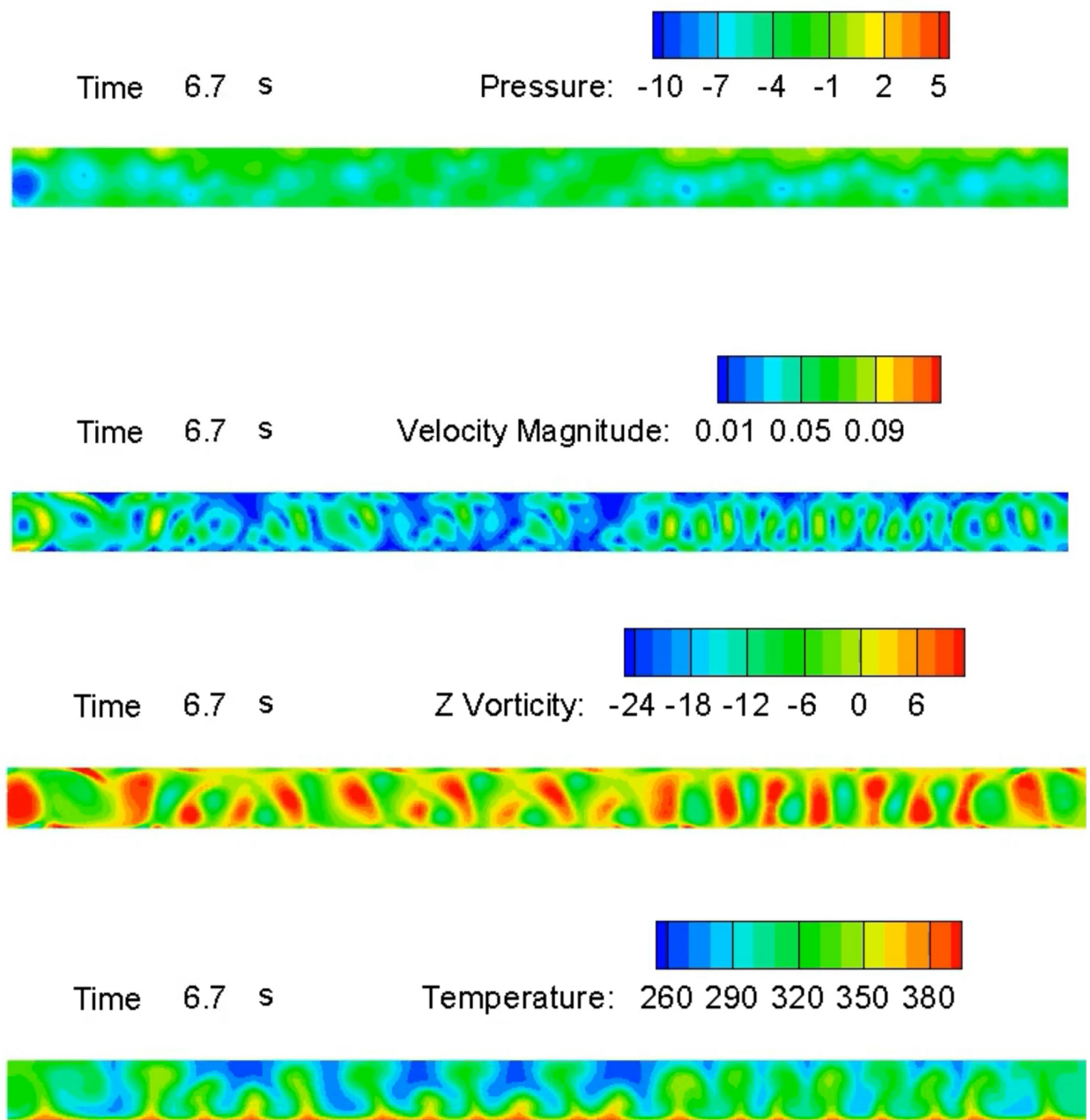


Figure 4.27: Transient Simulation of Rayleigh Bénard Instability, $t=6.7$ s. Laminar Case

4. Results

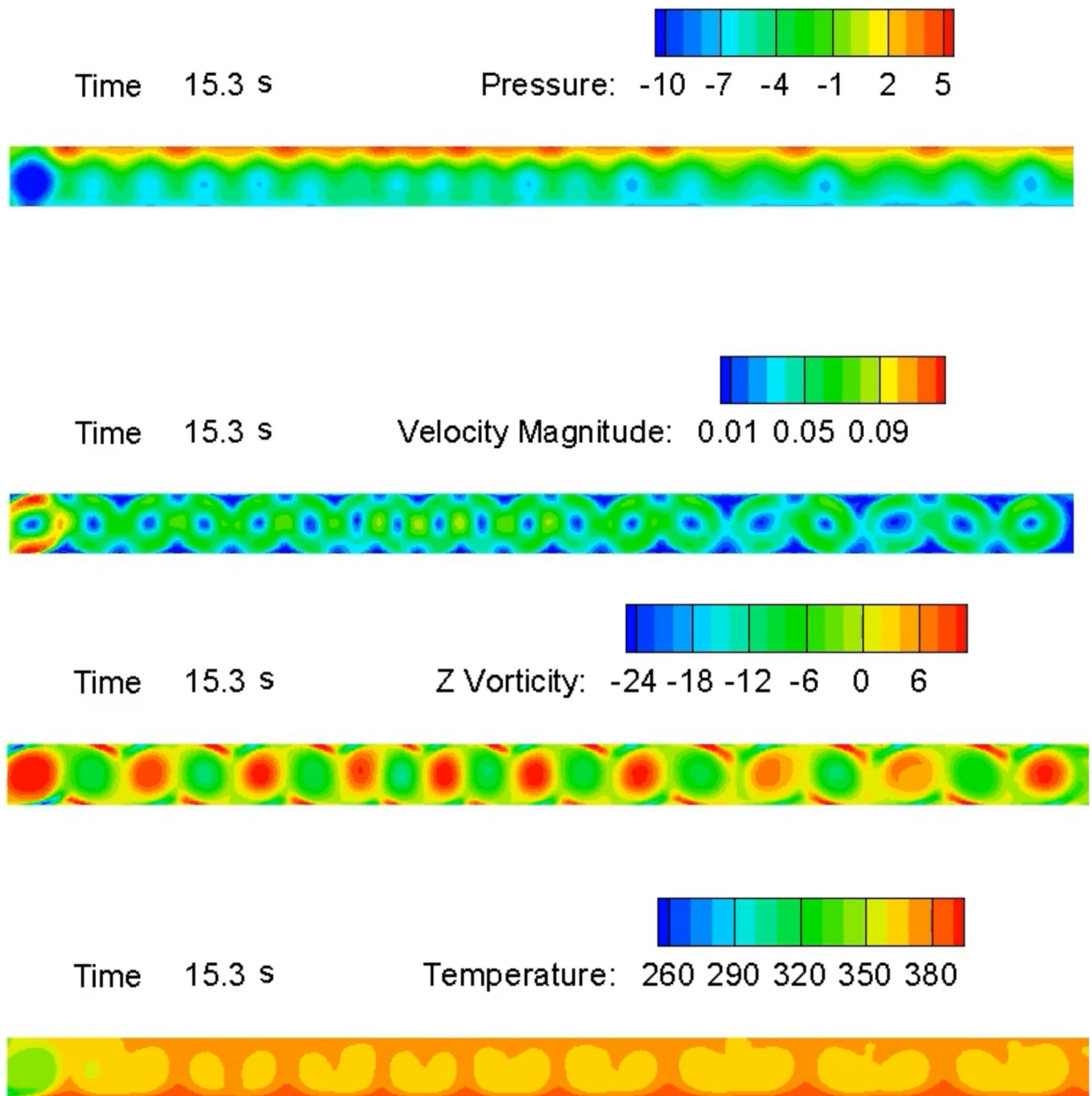


Figure 4.28: Transient Simulation of Rayleigh Bénard Instability, $t=15.3$ s. Laminar Case

4. Results

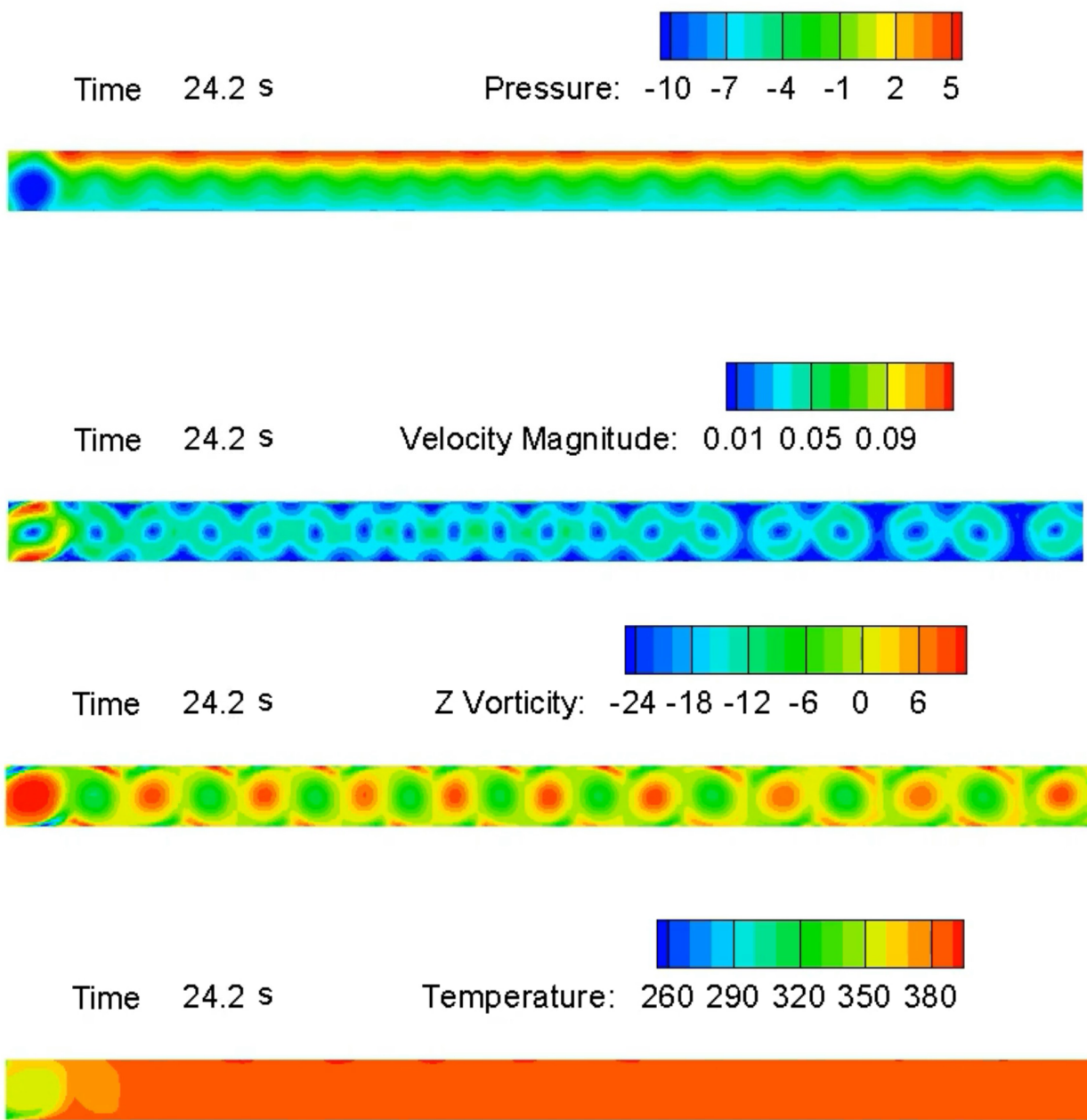


Figure 4.29: Transient Simulation of Rayleigh Bénard Instability, $t=24.2$ s. Laminar Case

4. Results

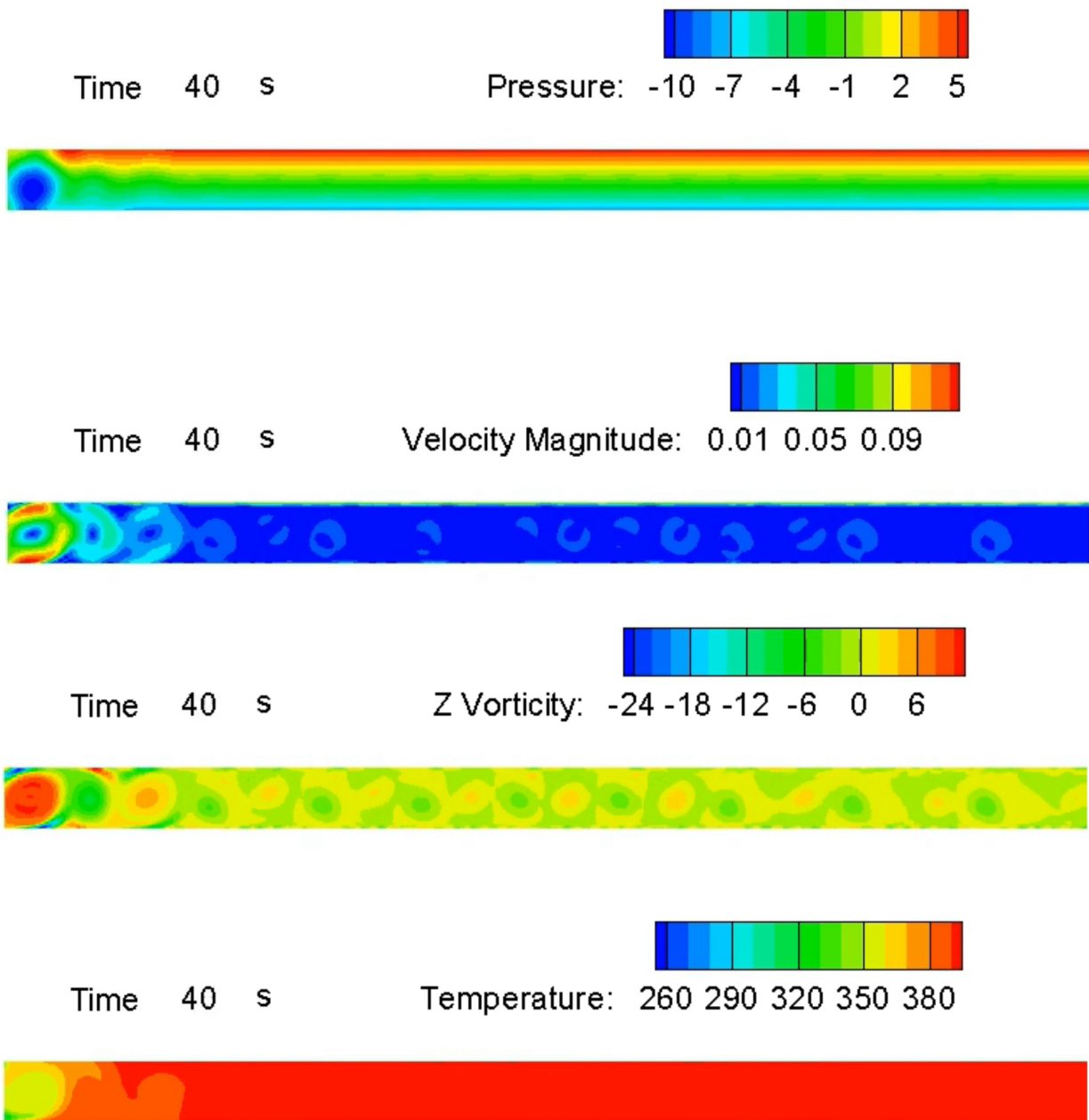


Figure 4.30: Transient Simulation of Rayleigh Bénard Instability, $t=40$ s. Laminar Case

4. Results

The initial stage of the flow variables, at $t=0.1$ s - Figure 4.25 is showed so as to provide proof that the instability onset is not instantaneous but also to evidence the initial values of the flow, which directly come from the inlet (as a result of the initialization).

Then, in Figure 4.26 the first step of the Rayleigh-Bénard convection is appreciated: a pattern is specially developed in the velocity magnitude and z-vorticity subplots. Some convective waves -remarkable in the temperature contours- start to be created in the inflow and outflow nearby regions while only vague shadows of the phenomenon are barely appreciated in the pressure field. Special curiosity is risen by the z-vorticity distribution, as the origin of a numerous set of contrarotatory vortexes is starting to develop.

The formation and consolidation of convective cells gets more visible in Figure 4.27, where the structure of the Bénard cells are about to acquire solidity in the whole domain. It is interesting to note that the region in which the instability is less developed is qualitatively at the center of the duct in the x-axis direction, which can be expressly noticed in the contours of the pressure pattern but also of the velocity magnitude, since values are relatively less intense in comparison with inflow and outflow vicinity. Clearly, at this time (6.7 s) one could ensure that both buoyancy and gravitational forces are reaching similar orders, so that they effect is not so distant in magnitude. This fact is triggered by the temperature gradient between both upper and lower plates, turning the conduction predominant heat transfer mechanism into convection. This fact can be easily seen in the temperature contours, where convection waves (with the usual "mushroom"-like shape) try to reduce the adverse temperature difference and attain a meta-stable equilibrium.

This steady pattern reaches its maximum strength and stability at $t = 15.3$ s, whose results are gathered at Figure 4.28. It is astonishing to observe the shape of the convective cells visually developed in the velocity magnitude, which interestingly, are not strictly equally shaped along the x-domain. The z-Vorticity plot also describes an amazing pattern of circular contrarotatory vortices with secondary ones in their corners, which was indeed theoretically expected but not so accurately with low-order schemes and definitely not with this mesh quality, which is totally brilliant and breathtaking. In fact, two vortices have still not found the steady configuration and they keep moving and evolving, and once they reach this state, the flow will loose its strength by diffusion. Overall, most vortexes have similar configurations except from the first one, which is the most strong and possesses the maximum contours of velocity. Once this configuration is achieved, it will start to loose gradually energy by diffusion such as it is seen in 4.29 until only the first vortex is appreciable in $t=40$ in 4.30, which will remain stationary for a long time until the difference of temperature between its upper and lower region tends to 0. As it

4. Results

has been seen, in the whole other domain, the thermal equilibrium state is reached, which indeed is another cause of why the vortices disappear. Now, the heat transfer will take place as conduction instead of convection.

4.5.1.2 Laminar

One should remember that the Rayleigh number for the just reviewed case was approximately 5.68E+05, and that the blood flow would be stable only if, with the same conditions, ΔT was less than 0.2105K between both plates. In the other hand, the Rayleigh number with ΔT is 8112.8 K, which is remarkably less than the previous flow but still nearly 5 times bigger than the critical Rayleigh number from which the flow turns into unstable. This is why, we will evaluate this unstable case but also a stable case from which the instability will never develop, with ΔT of 0.19 K and consequently $\text{Ra}=1541 < \text{Ra}_c$.

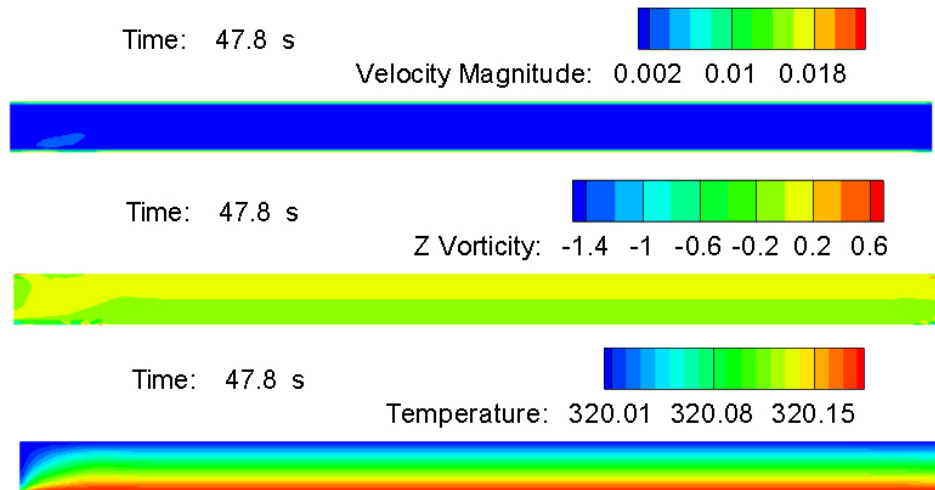


Figure 4.31: No Rayleigh-Bénard instability onset for ΔT of 0.19 K, $\text{Ra}=1541$

As it can be seen, in the previous Image 4.31, if the flow is stable the RBI will not be triggered. There's a minimum delta T to trigger the instability, or equally, a maximum delta T for which the flow is considerably stable. However, regarding the instability, ΔT does also play an important role in when the instability is onset, its configuration, and the energy of the vortices. This is why, if ΔT is set to 1 K, which is significantly less than the 120 K from the previous evaluated case but still unstable flow ($\text{Ra} = 8112.8$ K), the instability will be triggered -logically- sensitively later than in 4.28.

4. Results

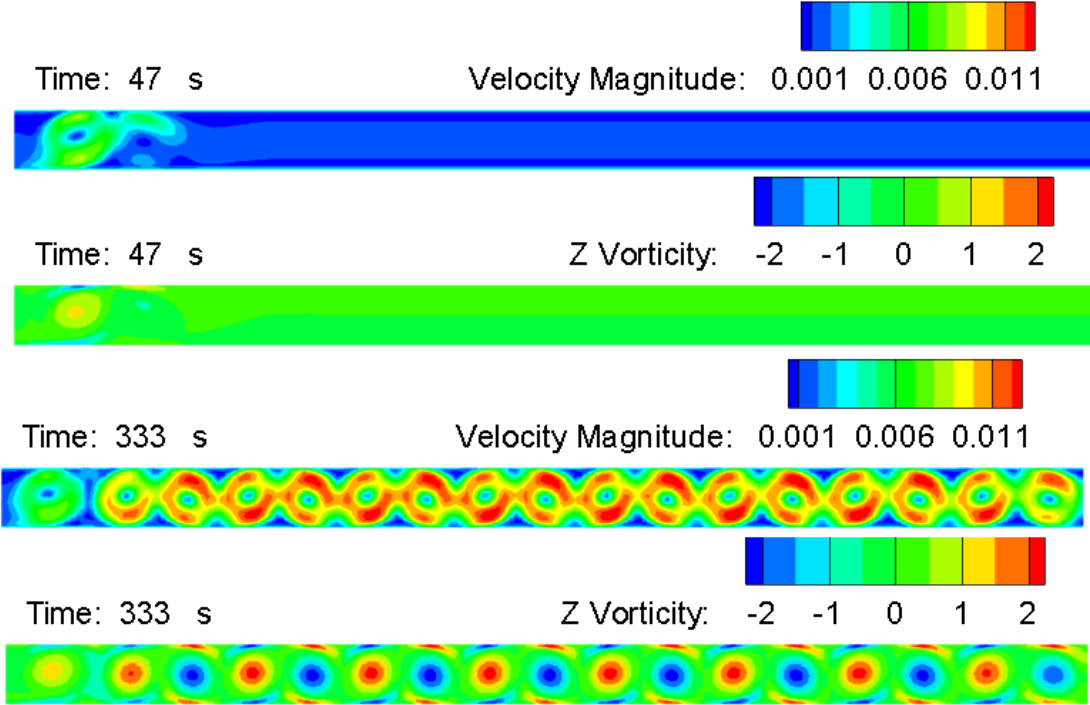


Figure 4.32: Rayleigh-Bénard instability onset for $\Delta T = 1 \text{ K}$

The first proof of onset is obtained at $t=47\text{s}$, then the turbulent case of ΔT has barely lost all the onset by turbulent energy diffusion. It reaches its maximum after $t=333\text{s}$ of simulations, which is pretty late compared with 4.28. As it is laminar, the diffusion will not be so significant thence this pattern will remain steady by a larger time than the previous case.

Thanks to these results, extremely useful ideas have been derived. Temperature difference indeed significantly contributes at which time the instability will be onset but also the intensity of the vortices. However, this intensity will also depend on if flow is turbulent or laminar, as diffusion will be much stronger in the turbulent case and the Bénard Cells will disappear sooner. Also, it has been proven that the Rayleigh number really serves to determine if the flow will be unstable or not, as two cases of unstable flows (Figures 4.28 and 4.32 with different ΔT) have developed instability and vortex cores while one in which the Rayleigh number was lower than the critical (Figure 4.31) could not, and would not for any time.

4. Results

4.5.2 Amendment on Tzirtzilakis Blood Modelling

Once reached this point, a parametric study was intended in order to determine additional traits and dependencies which might not be evident in the previous plots. However, when revisiting the parameters used by Tzirtzilakis in his blood model in [1], after analyzing them thoroughly, they come to be extremely inaccurate to model the blood flow. More than three variables have been made up and their values are distant from what is obtained in real life. Hence, a more accurate description of the real blood flow will be obtained by, using data from [14], [94] and [95] the following amendments have been made:

Flow parameter	Value
ρ	1060 kg/m ³
g	-9.81 m/s ²
c_p	3617.286 J/(kg K)
k	0.52 W/(m K)
μ	0.0032 Pa/s
Thermal expansion coefficient (α)	0.000257 (1/K)
thermal diffusivity (a)	$1.36 \cdot 10^{-7} \text{ m}^2/\text{s}$
T_{inlet}	320 K

Table 4.7: Corrected Flow Condition Values for the Simulations of Blood in a 2-D Rectangular Channel. Investigation of Rayleigh-Bénard Instability.

Considering that the height of the duct is the one from the geometry meshed ($h=0.005\text{m}$), if the Rayleigh number is computed so that

$$Ra = \frac{\alpha g h^3 (T_l - T_u)}{a \nu} \quad (4.3)$$

and the temperature of the lower plate T_l remains 1 K higher than the upper plate, a Rayleigh number of $Ra=2.46 \cdot 10^6$ is obtained. Indeed, it is higher than the Rayleigh number from the prior case (even though a temperature gradient of 120K was present) and is about 1000 higher than the critical Rayleigh number, so the instability will theoretically develop. Equally, one can obtain that the Rayleigh-Bénard Convection will be formed if the difference of temperatures between both plates, being greater in the lower plate, exceeds $6.7 \cdot 10^{-7} \text{ K}$.

Furthermore, regarding the blood fluid properties, an additional parametric study can be also developed to review the Ra dependency on its parameters. One could think of the example of, using blood, an extra-corporeal treatment such as the ones applied in mainly heart surgeries but also seen in some cancer cases, hypothermia and even in some severe Covid-19 patients. Depending on the unequal temperature of the duct, and its diameter,

4. Results

the Rayleigh-Bénard Instability could be triggered. This is why, we will represent Ra against the diameter considering a difference of temperature of 1 K in Figure 4.33a and by 4.33b, setting h as 0.05m such as in our geometry, varying the difference of temperature.

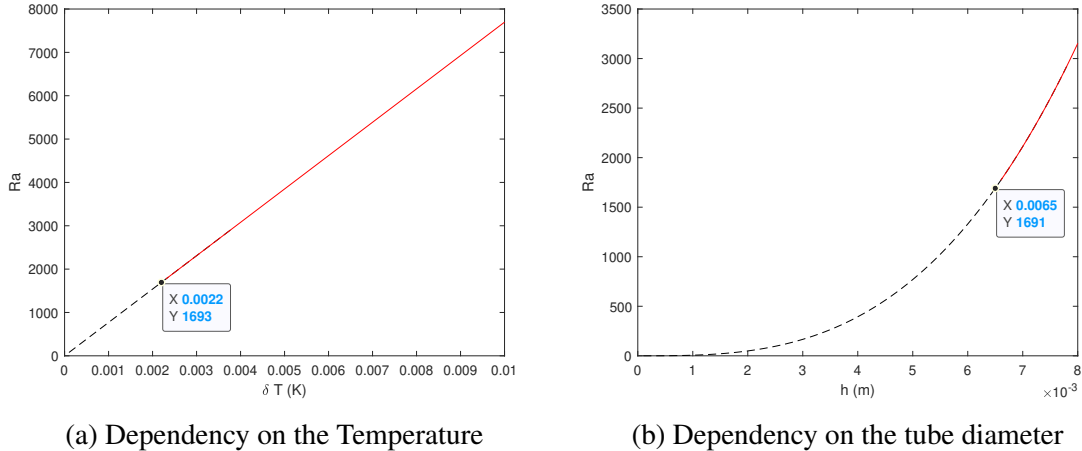


Figure 4.33: Rayleigh number parametric dependency

In the plots from above, the region where the flow becomes unstable is represented in red and the last point of stability is conveniently marked. As it can be seen, in 4.33a, if h is set to 0.05 m, and with a greater ΔT than 0.02 K, the instability will be driven. Similarly, if ΔT is set to 1K, for bigger heights than 0.0065m, this mechanism will subsequently be present too. In this last chase, one can scale by using another ΔT desired since the relationship between this variable and Ra is directly linear, proportional.

Besides, the PVC ducts -cannulas- used in extra-corporeal blood treatments are also considered as well. Their diameter tends to be measured in Fr, which is not one of the IS length measurements, and the most used correspond to 9 Fr (3mm), 12 Fr (4 mm), and 16 Fr (5.3mm). If blood is transported, in the following Table 4.8, the critical ΔT_c which will represent the threshold of developing the instability

Diameter (Fr)	Diameter (mm)	ΔT_c
9	3	10.27 (K or °C)
12	4	4.34 (K or °C)
16	5.3	1.86 (K or °C)

Table 4.8: Critical Temperature Different for different medical cannula sections.

Logically, as the equation 4.3 reveals, the greater diameter, the less difference of temperature required to trigger the instability. Given this information, one should definitely consider

4. Results

this data if ducts with relatively high h are used and remarkably non-uniformly heated.

As it has been shown, if a difference of 1 K or $1^\circ C$ is presented between both upper and lower boundaries (being hotter in the bottom plane), the Rayleigh number will be approximately $Ra = 2.46 \cdot 10^6$ which is definitely located in the unstable region. The Rayleigh Bénard Convection, at some point, will be consequently triggered. First, we will evaluate the flow with $U=0.001$ in order to not make the axial velocity sweep the convection, several temperature cases will be reviewed either with Laminar and Turbulent Flows, and finally a change in axial velocity will be introduced.

4.5.2.1 Laminar Case

The blood flow has been simulated under the conditions described previously in a duct with $L=0.9$ and $h=0.05$ with an adverse gradient of temperature of 1 K between the solid walls. Even though the Rayleigh number is significantly higher than the Tzirtzilakis blood model, a slower onset of the convective instability is presented. The main reason behind this trait is the fact that, with c_p with value 14.186, the fluid is able to propagate or conduct the temperature from the hotter to the colder region within a short amount of time. This is why, the convective instability in the Tzirtzilakis conditions has triggered the RBI significantly earlier. One solid conclusion, which is not so evident, has been therefore obtained: the higher Ra doesn't mean the higher trigger of the onset, specially when two different fluids are evaluated.

Figure 4.34 reveals that the convective instability does take place after, approximately, 239 seconds even though this change is really slow and gradual and from second 47 a faint instability nucleus can be witnessed. This instability, motivated by convection, reaches both plates at approximately 84.1 s, entailing a subsequent secondary flow movement. In that stage, two different but low-energetic contrarotatory vortexes take place in the perturbed region, with its secondary contrarotatory vortices in their corners. This trait evolves spatially as time goes by, triggering the instability in the outflow at $t=167.1$ s, such as it happened in the simulations carried out by using Tzirtzilakis Blood Model. Afterwards, this instability travels backwards until it reaches the perturbed region in the proximity of inflow, and this is where the instability reaches its maximum at approximately $t=239.1$ s. Both velocity and vorticity plots evidence an instability generalized through all the whole domain, but with significantly less energy than the one sighted in 4.29; this is why the same Bénard cells structure are not obtained. Finally, as time evolves, the pattern remains and moves in the x -direction but loses a bit of magnitude as a consequence of diffusion. Logically, the vortexes associated to the instability evolve accordingly as well.

4. Results

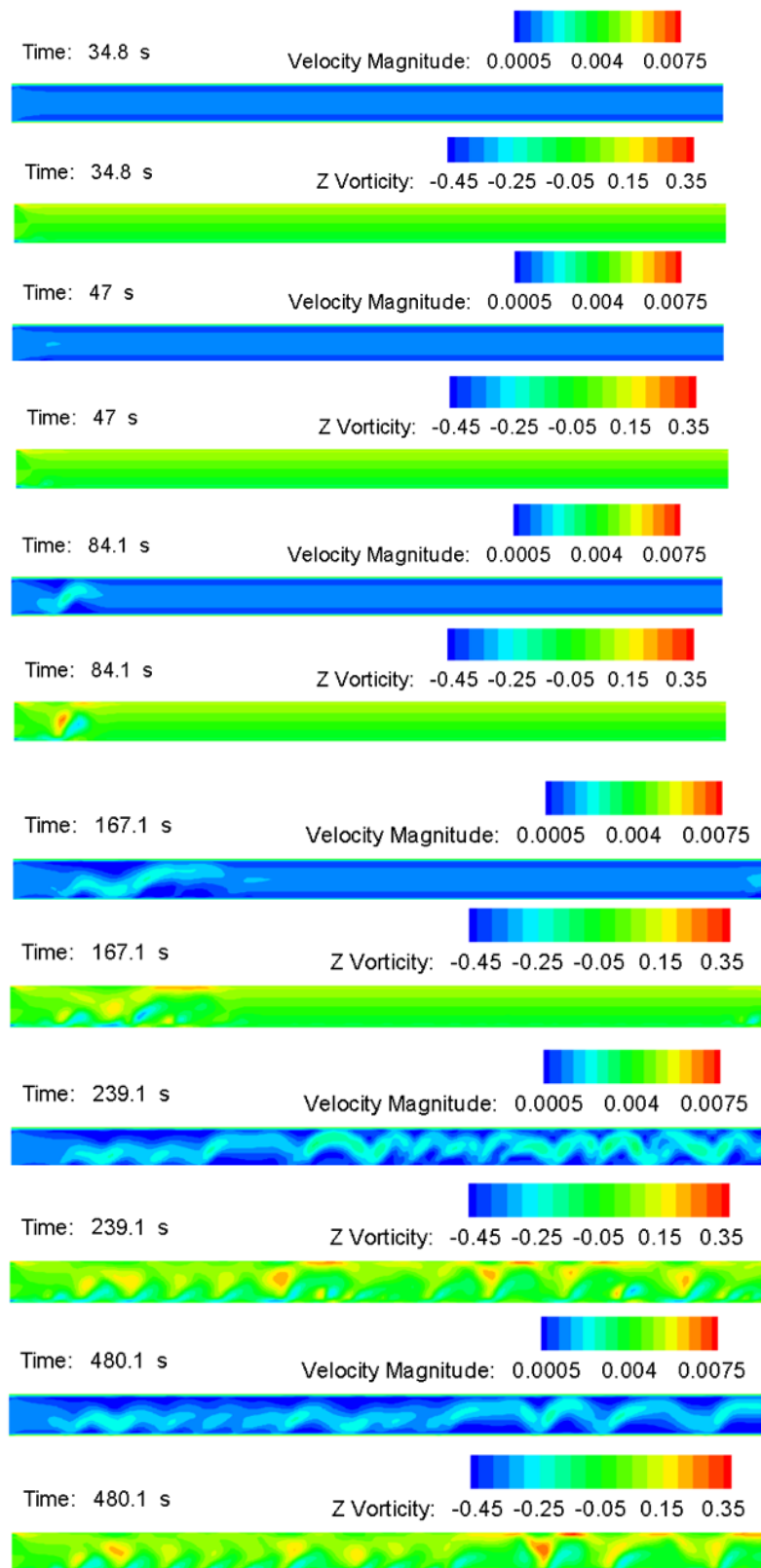
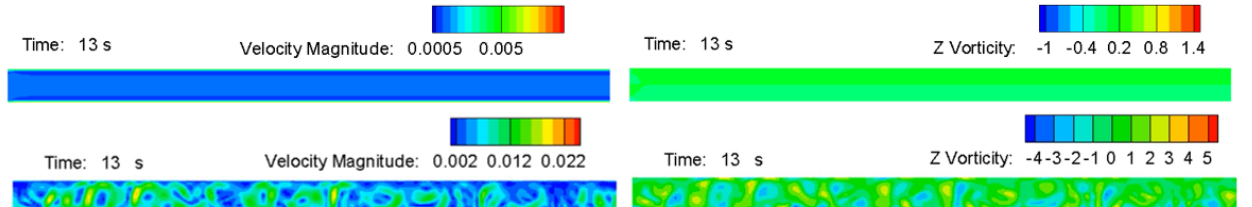


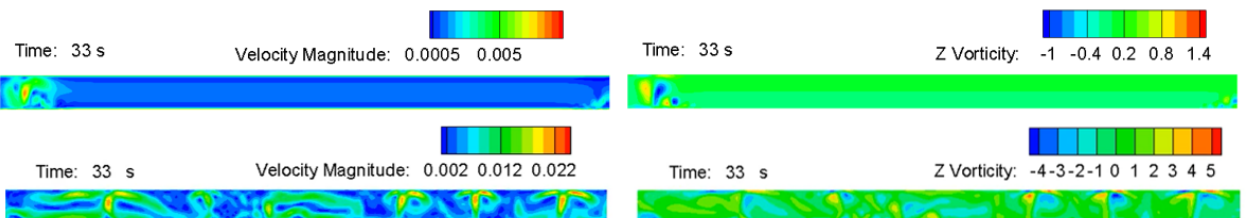
Figure 4.34: Laminar Transient RBI Simulation. Contours of Magnitude Velocity and
Z-Vorticity

4. Results

There's a significant difference between this pattern and the one sighted in Section 4.5.1.1. Even though the Rayleigh number is bigger by nearly 100 times, the convection is not onset with the same strength and Bénard Cells do not acquire those steady shapes. This is mainly because of two traits: while the conductivity is assumed to be the same than water ($k=0.61$), the c_p provided by Tzirtzilakis is 300 times smaller than the real for blood flows, 3500 against the 14.186 from [1]. This is why, the flow with his "conditions" hybridized with water is able to propagate and conduct temperature with more easiness, as the fluid does not require barely energy to increase its temperature due to the unrealistically low c_p . Conduction, and then convection, is massively over-predicted due to this issue in the setup. However, a very interesting conclusion has been obtained: The higher the Rayleigh number does not imply the more likelihood to notice the instability and also does not account for the strength of the RBI. Additionally, this onset is also dependant on the flow regime and even in the boundary conditions (inlet and walls), which the Rayleigh number does not consider either. Nevertheless, we will increase the temperature difference between the plates and enforce the convective instability to develop with higher instability and faster, so different setups of ΔT will be reviewed in the following lines.



(a) $t = 13$ s. Upper Image: $\Delta T = 10K$, Lower Image $\Delta T = 100K$



(b) $t = 33$ s. Upper Image: $\Delta T = 10K$, Lower Image $\Delta T = 100K$

Figure 4.35: Transient Simulation of Rayleigh Bénard Instability, variation of ΔT

4. Results

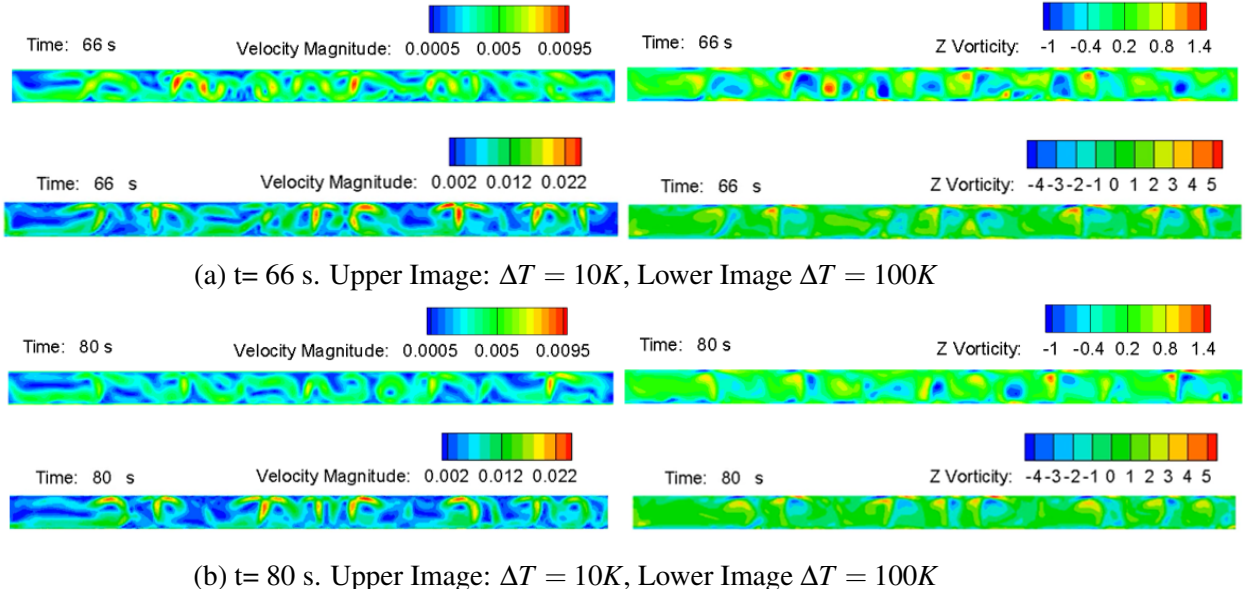


Figure 4.36: Transient Simulation of Rayleigh Bénard Instability, variation of ΔT

The partial instability witnessed with the $\Delta T = 1\text{K}$ case is now fully developed. Figures 4.36 and 4.36 show how different adverse temperature gradients affect the Rayleigh-Bénard instability onset. As its magnitude is bigger, convective and thence buoyancy forces are stronger. Due to this, the Bénard cells are triggered before, they time they take to appear is inversely proportional to ΔT . However, this trait is not the only one sighted, as the vortexes will be also stronger depending on this temperature gradient. The magnitudes of both velocity and vorticity in the Z-axis subsequently acquire bigger local extrema.

The main conclusion from the two different cases in which the temperature of the plate from below was raised with $\Delta T = 10$ and 100 K demonstrate that the higher the gradient, the quicker the instability will be triggered but also the more intense it will be. Additionally, it is also derived that the permanency of this Bénard-Cells patterns will be more perdurable with the highest temperature difference.

4.5.2.2 Turbulent Case

Now, the turbulent case, for the corrected Blood Flow Model will be investigated. The model chosen to describe the blood turbulent behaviour is the $k-\varepsilon$ due to its high accuracy and performance in the mean flow treatment but also on the boundary vicinity. As it has been detailed in the previous turbulent simulation 4.5.1.1 but also in literature [93] the turbulent Rayleigh-Bénard Convection definitely breaks the homogeneous patterns

4. Results

achieved in Figure 4.29 to produce chaotic, totally unsteady irregular patterns which are indeed very hard to model mathematically due to its strong non-linearity. However, they also introduce an important effect in the dissipation of the flow. Now, the same conditions from 4.7 will be considered, and the lower wall will be assumed to be 1 K hotter than the upper wall, which presents the same temperature than the inflow.

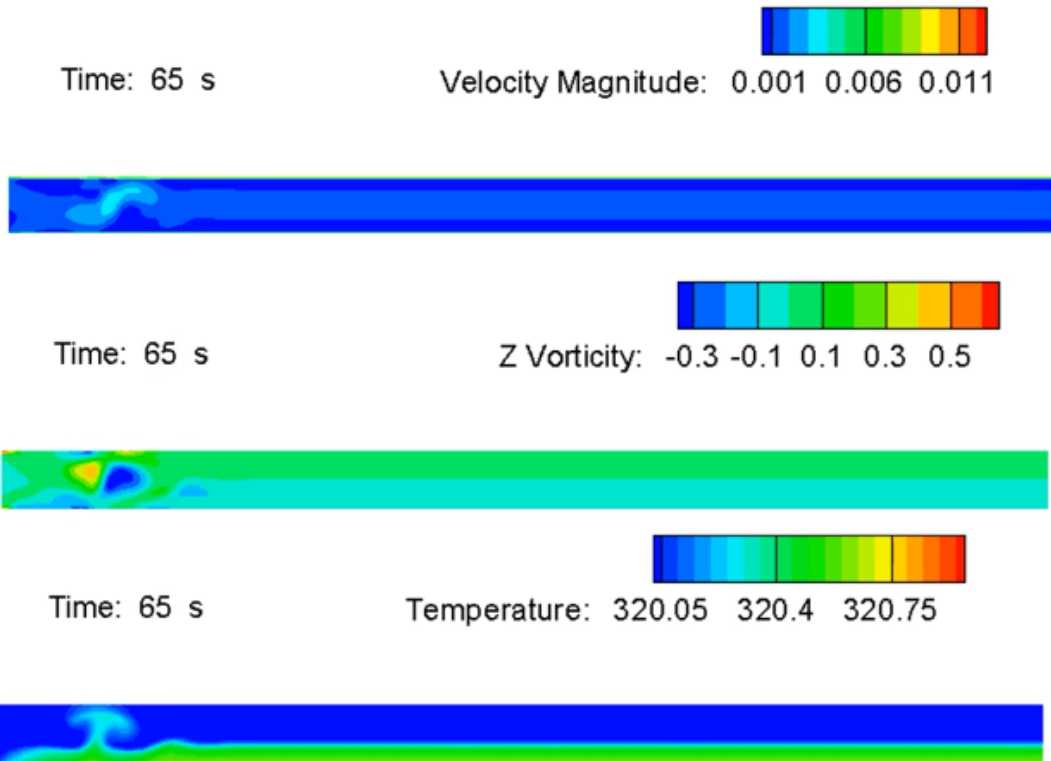


Figure 4.37: Turbulent Simulation $t = 65$ s

Figure 4.37 demonstrates at which time the first noticeable proof of the instability is onset. Approximately, it takes less time than the laminar case and the apparition is really sudden, it barely evolves in time, it just quickly appears. This characteristic is in fact a common trait of turbulent flows and gives an idea of the difficulty to analytically predict their behaviour. The velocity magnitude and the Z-vorticity plots are represented as it may be the most noticeable variables to capture the RBI, however the temperature distribution is also attached in order to detail the convection evolution. The mushroom-shaped energy transfer is here depicted as it was expected, creating two main contrarotatory vortexes with secondary ones in their corners. This onset will evolve to the outflow as time goes by, achieving an almost complete pattern of instability in the whole domain.

4. Results

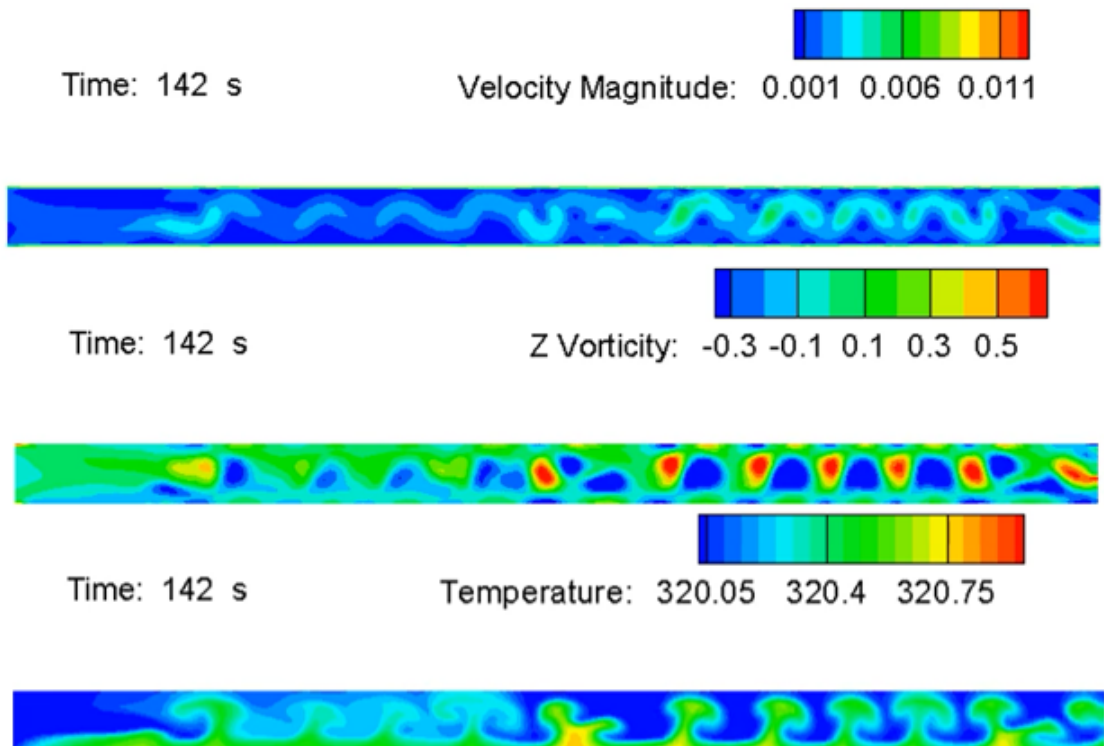


Figure 4.38: Turbulent Simulation, $t = 142$ s

Figure 4.38 demonstrates the time step (142s) at which the instability will achieve its maximum influence, presenting the highest values of velocity magnitude and vorticity due to the perturbation it introduces. By taking a look on the Laminar case from Figure 4.34, the turbulence case acquires its maximum significantly quicker (with a difference of almost 90 s) but also presents higher magnitude of the fluid variables. Thence, an important conclusion is obtained: the instability is significantly stronger in the turbulent case, it is sudden, hostile and more chaotic. However, turbulent dissipation also plays an important role in the time evolution of this highly unsteady and unpredictable pattern and, thence, after 280 seconds, an important part of this energetic state will be lost.

4. Results

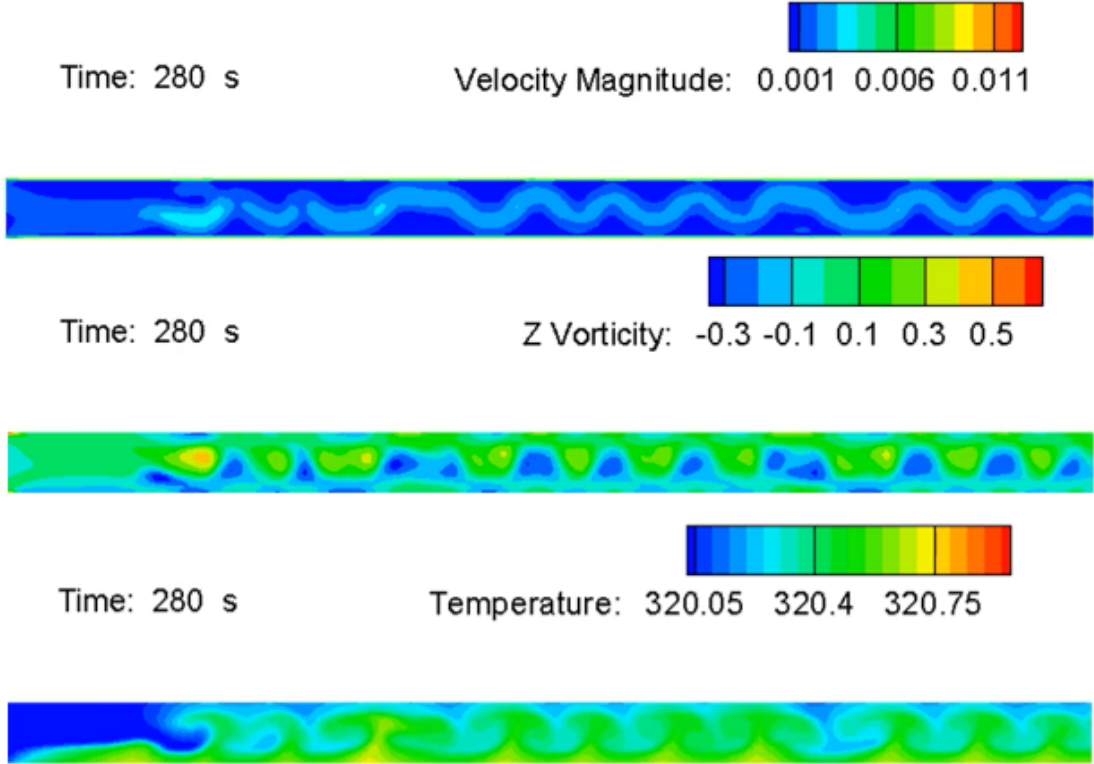


Figure 4.39: Turbulent Simulation, $t = 280$ s

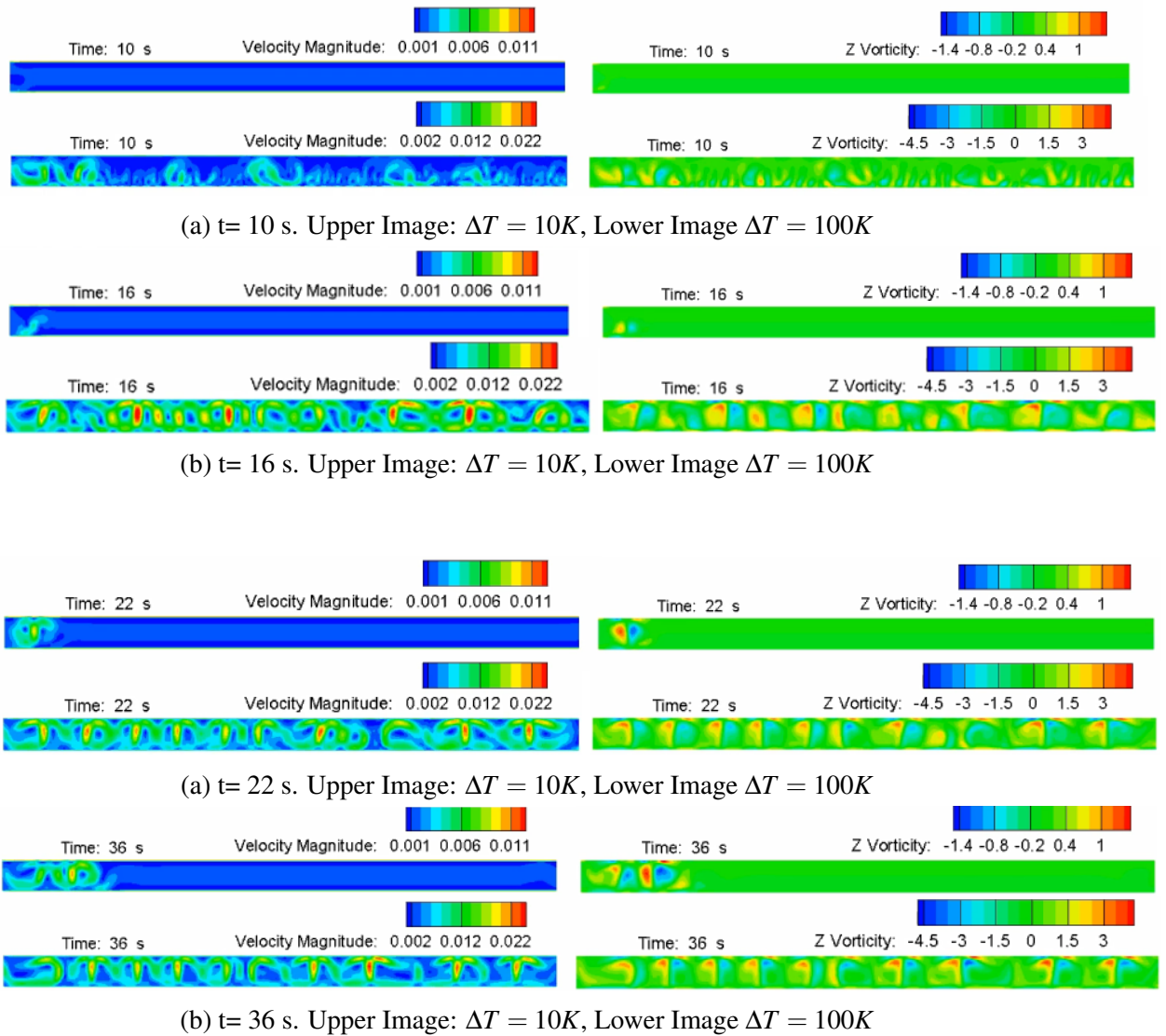
In Figure 4.38 one can notice the turbulent dissipation which strongly softens the instability. The vortexes seem to merge one with each other and consistently loose its structure and energy. In the temperature plot, an important diffusion of the convection heat transfer is noted in the medium, tending to a homogeneous distribution. This is why, one should expect that the time evolution will keep milder the instability. The fact that it is turbulent, however, could imply the creation of another very energetic meta-stable state such as the ones present in [93] so the advancement of the simulation is needed to assure, with reliability, the posterior behaviour of the flow.

The same thermal-dependency investigation carried out in the Laminar case will be also performed within the next lines. A difference of temperature of $\Delta T = 10$ K and $\Delta T = 100$ K will be imposed between both upper and lower wall, being consistently the hottest pole located along the lower surface. Find in the following images, the time evolution of both cases.

As it has happened in the $\Delta T = 1$ K case study, the instability will be triggered before than the laminar case, being the first to present it the simulation $\Delta T = 100$ K at approximately

4. Results

10 s, which is 16.67% sooner. The instability has been wholly triggered along the geometry domain. In the other hand, the turbulent flow with $\Delta T = 10$ K gradient will introduce an initial first vortex at approximately $t = 22$ s (27.7% sooner than the laminar case) which will evolve in time. Between these two time steps, the higher gradient case has developed a chaotic motion of the instability structure: it continually loses its shape. This is mainly due to the turbulent vortices, which are highly unsteady and not uniformly shaped; in fact, they pass from circularly-shaped to arbitrary randomized amorphous shape (with some tendency to T or L configurations) which evidence the importance of the turbulent energy. The magnitudes, accordingly, are higher than the Laminar case.



4. Results

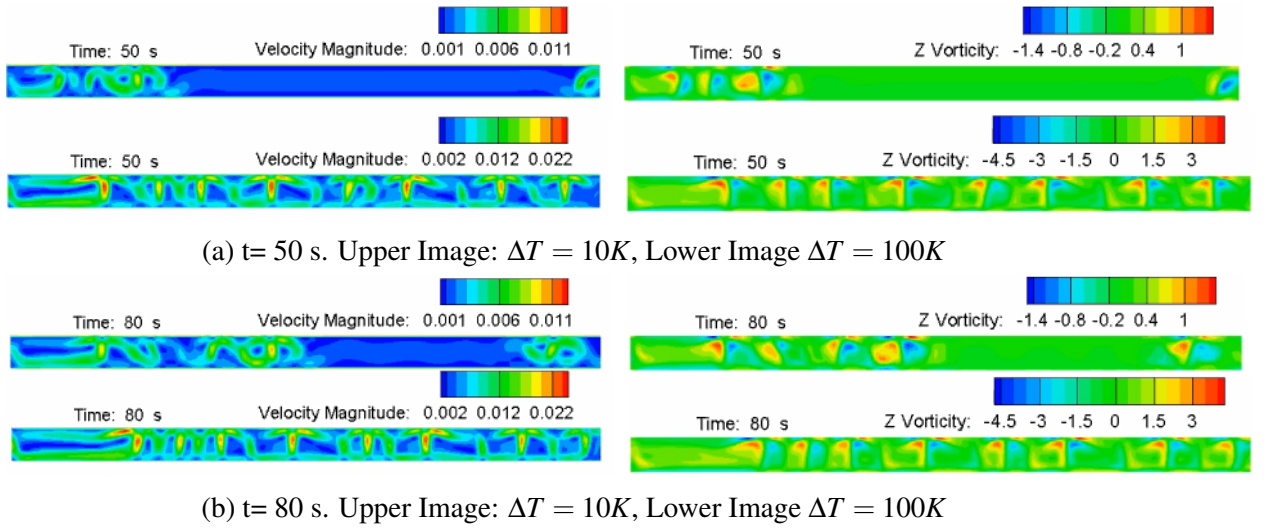


Figure 4.42: Turbulent Transient Simulation for Blood Flow Rayleigh-Bénard Convection onset, thermal case study

Surprisingly, in contrast with the Laminar Case, for $\Delta T = 10$ K, even though it sooner develops its first vortex, does not establish for the whole domain before than $t=80$ s. The vortex cores interact rather between their-selves than grow from the inlet to the outlet, whilst a secondary cortex core gets formed at the outlet proximity and advances towards the inlet. Besides, Velocity and Vorticity magnitudes are slightly higher than the Laminar Case. By acknowledging this, the turbulent contribution in which the flow becomes arbitrary, chaotic and hardly predictable is highly evidenced. Meanwhile, the more energetic case in which $\Delta T = 100$ K evolves in time with strong unsteady motion, constantly adopting new meta-stable configurations that suddenly evolve and move to another. As time goes by, vortexes experience a remarkable deviation from their initial and "idealized" round shape.

It must be said that the deviations between these laminar and turbulent cases were fully expected. The chaotic nature is inherent of turbulence: it is more energetic but more dissipative at the same time and as time goes by. The evolution is fully unsteady and flow variable magnitudes tend to be higher. Apart from these obvious differences, similar conclusions can be withdrawn such the ones presented in the Laminar study.

The whole study on the Rayleigh-Bénard Convection regarding the Blood Flow has been considering $U=0.001$ since a high velocity inlet would definitely sweep the convective instability. Even though the Rayleigh number is significantly bigger than the critical value $Ra_c = 1708$ with a high adverse gradient between both plates, and thence the flow is assumed unstable, if a strong velocity inlet is present, convection may never take place.

4. Results

Therefore, some modifications of the Rayleigh number should be further done by taking into account further variables such as inlet conditions. Here, we would like to present a case study of a real inlet velocity (0.3 m/s in the systole peak according to Figure 4.21) with a really strong temperature gradient of $T=100$ K to acknowledge if this effect is considerable in a real blood flow. Hence, we will set $U_{inlet} = 0.3$ m/s constant in time and $\Delta T = 100$ K.

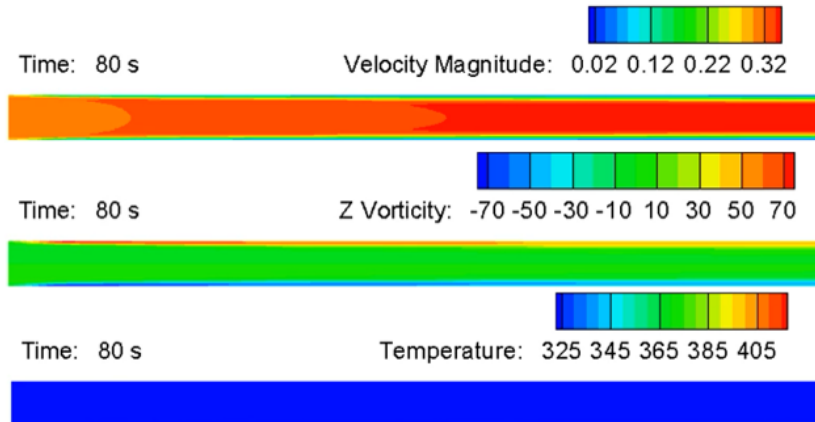


Figure 4.43: Real Velocity Systole Inlet, $\Delta T = 100$ K

As it can be seen, even though the Rayleigh number (Ra) is high enough $Ra = 2.46 \cdot 10^8$, the Bénard Cells will not develop. Velocity is sufficiently strong to impede the formation of the instability pattern. This is why, one should not worry about Rayleigh-Bénard Instability in blood circulating cases, but could if is is quasi-steady or steady. However, two tiny but very energetic vortexes form at the proximity of the wall resulting in two characteristic regions in which reversed flow is present in these small zones. This trait is consequence of the high gradient of temperature, which indeed locally affects the density and hence buoyancy, but convection is totally swept by the current. Logically, those regions will increase its surface as temperature gradient is higher, until both surfaces touch and they develop the instability pattern. Since there's no dependency -at least, in knowledge of the author- between instability onset with velocity to determine at which gradient the instability would be onset, it would be just matter of simulating different setups for a considerably long time.

By assuming a pulsatile velocity inlet, the instability should be even more difficult to trigger. Convection needs time to develop under the same local conditions, so it would be more easily erased by the changing velocity pulse.

4. Results

Regarding this last case study, no Rayleigh-Bénard Instability onset should be expected in the blood circulatory system.

4.6 Ferro- and Magneto-hydrodynamic effects in conjunction with Rayleigh-Bénard Instability

In the previous sections, two different perturbations in which blood flow is prone to get exposed have been separately studied: The FHD/MHD effect under a localized magnetic field and the Rayleigh-Bénard convective instability. Now, the combined effect of both will be coupled and studied. Several publications have been developed to describe the action and scope of the magnetocaloric effect, being one of the most relevant the contribution of [23]. In it, the convective instability is studied with the FHD assumption, obtaining that both phenomena have an additive (more precisely, multiplicative) effect on the onset of the stability. Here, we will study with a more complex blood flow model the interaction between both chattels.

The FHD/MHD study has been performed under the same model provided by [12] and [1] in order to validate the schemes and code used for the own investigation, hence here it will also be applied in order to drive a comparative analysis. However, one should remember that mistakes have been made in their publications and thence several amendments have been applied in this document so as to constitute a more accurate and solid blood flow model.

Hence, one should consider the conditions applied in Table 4.1, being the magnetic field induction $B = 10 \text{ T}$ with an initial constant velocity inlet of $U = 0.001 \text{ m/s}$. Even though the flow is clearly unstable with an adverse temperature gradient of ΔT between both plates, being hotter in the lower wall and resulting in $Ra \simeq 8000 > Ra_c = 1708$. However, as it has been shown, the highest temperature gradient the more intense the convective instability will be and the quicker it will appear. Therefore, in the following examples, both different temperature setups of $\Delta T = 50K$ and $\Delta T = 100K$ have been used in order to quantify the relationship between both phenomena.

4.6.1 Thermal difference of $T = 50 \text{ K}$

Flow quasi-instantly achieves a steady state in most of the flow variables but it does not for temperature. Since the axial velocity imposed by the velocity inlet is weak, the most important movement takes place in the vortexes triggered by the FHD contribution when ferromagnetic fluid faces the finite magnetization gradient. The MHD term, even though

4. Results

it is not so significant, curves the velocity flow within the localized magnetic field as a result of the Lorentz Force $F = q(E + v \times B)$. Nevertheless, now, instead of two main cores in velocity magnitude but also two vortexes, now we have an additional source coming from the convective instability. This one, given the temperature gradient, is not as much intense as the perturbation introduced by the FHD/MHD effect, but still is noticeable. Steady state results for the velocity magnitude, vorticity and streamlines are presented in Figure 4.44.

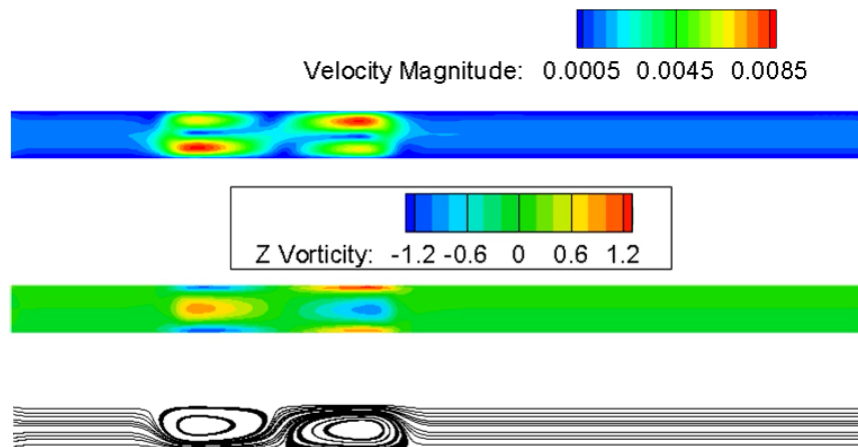


Figure 4.44: Steady Flow variables, FHD/MHD coupled with RBI for $\Delta T = 50$ K

As it can be seen, vortexes are indeed more intense than the ferro- and magneto-hydrodynamic results separately, in its higher value, velocity magnitude is multiplied by a factor of 8 which is indeed considerable. Streamlines also demonstrate the fact that these cores are consequently more intense. On the other hand, temperature -as it has been pointed out- will not develop a steady state as the thermal non-equilibrium between both plates will entail a heat transfer flow, first by conduction and then by convection. The presence of the "relatively" intense vortexes will make it curl around their cores.

4. Results

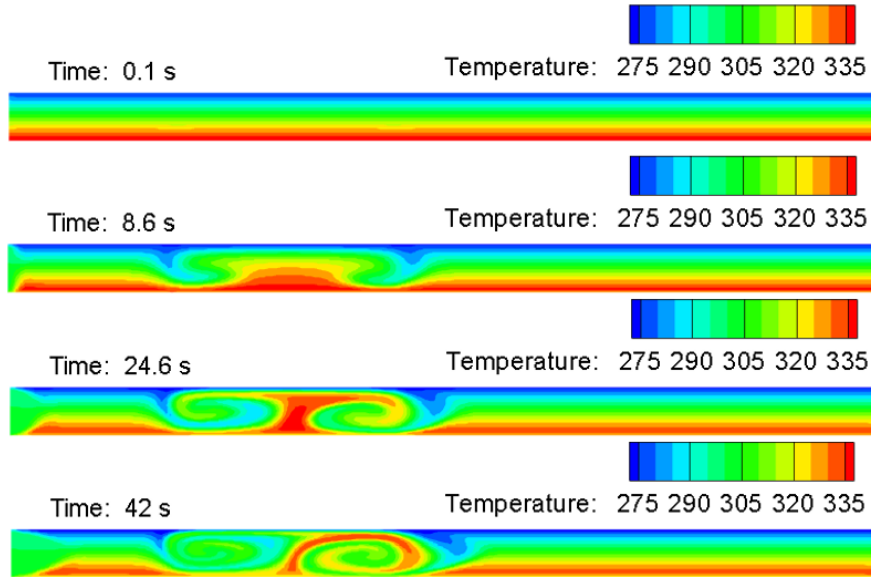


Figure 4.45: Temperature contour time evolution, FHD/MHD coupled with RBI for $\Delta T = 50$ K

Flow departs from an initially linearized state into a convective motion curling around the vortex core. The fact that no mixing phenomenon is sighted reveals that the program solves both temperature and velocity fields separately, as it has been corrected and performed in Section 4.2. If both equations were coupled, clearly, after the second vortex, a fully mixed contour would be sighted instead of recovering the initial linearized state. Nevertheless, here the aim is to detect how both perturbations interact. As it is reasonable, a stronger temperature gradient will primarily increase convection, thence buoyancy, and in minor rate magnetization and both magneto-caloric and joule dissipation energy terms. With an increment of ΔT , the FHD/MHD and RBI effects will be at similar order of magnitudes.

4.6.2 Thermal difference of $T = 100$ K

Interesting results have been obtained from imposing a temperature difference of 100 K between both upper and lower walls. The two effects reviewed are at the same time predominant then 4 fully developed structures are now in the velocity magnitude steady-state contour from Figure 4.46. Both contributions equalize their influence. The temperature evolution, as it happened with the prior case, will not be steady but transient and evolve as a convection, curling around the main vortex cores as it is shown in 4.45 therefore it will not be presented again.

4. Results

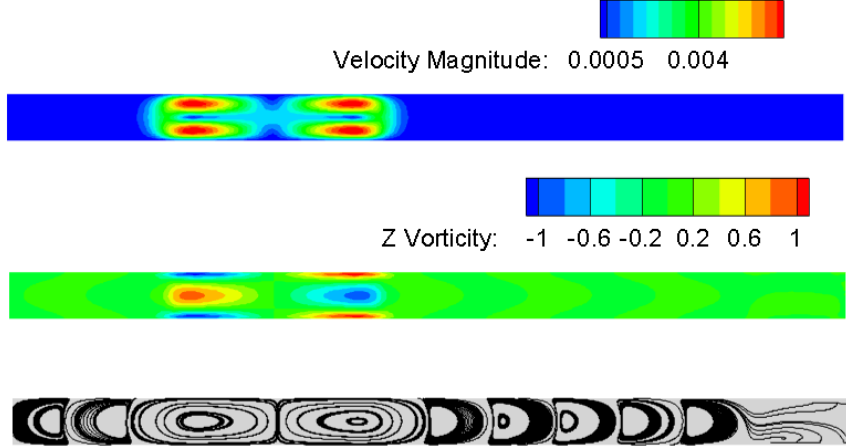


Figure 4.46: Steady Flow variables, FHD/MHD coupled with RBI for $\Delta T = 100$ K

Interestingly, the Rayleigh-Bénard Instability mainly develops in the localized magnetic field region, where it is totally onset, but does not seem to have influence in the whole rest of domain. Withal, in z-vorticity distribution plot but specially in the streamlines figure, it is perceived how it induces the formation of really weak contrarotatory vortexes in the rest of the domain, but with so little intensity that it barely accelerates or slows down the flow. Now, the main vortexes cores are indeed stronger than the ones obtained in Figure 4.44 as they totally reach both upper and lower walls. The fact that secondary vortexes die in the way the streamlines show is curious and not expected thence some minor adjustment, such as the use of finer mesh, higher-order schemes or both velocity-temperature coupled field should be further investigated in order to check the solidity of this result. However, one important qualitative conclusion has been proved: the Finlayson hypothesis from [23] arguing that both convective instability and FHD effects are multiplicative has been obtained and extended with the MHD source term.

Chapter 5

Conclusions

5.1 Introduction

The main purpose of this investigation was the Multiphysics evaluation of the Blood Flow Model by considering Non-Newtonian, Non-Isothermal fluid traits in conjunction with ferro and magnetohydrodynamic effects. The first document to consider both effects coupled was the research of Tzirtzilakis and Loukopoulos from [12] and [1] hence we have primarily compared our results with theirs but also with the latest investigations on the field. In the following lines, an initial description of the conductor line that has been followed will be briefly introduced to then give more details and solid conclusions of the findings.

The geometry we have used is a 2-D duct with the exact dimensions used in their investigations and from which 3-D effects can easily be extrapolated. The case to be studied models the application of a localized magnetic field with magnetization only in the Y direction which can suppose a good representative of MRI devices, electrostatic fields and other electrodynamic sources which the human being daily faces. The intensity of this magnetic field, which results in an evident impact on the human being, has been varied and subsequently contrasted. Then, after deriving similar results than Tzirtzilakis, the shear-thinning behaviour of blood – demonstrated in experimental investigations- has been taken into account by implementing several Non-Newtonian models which have been recently used in investigations and by setting their characteristic parameters to modelize the blood flow. The results predicted by the different blood models has been equally compared and here additional traits, which were not observed in the base-line validation simulation have been correctly witnessed.

According to very novel and recent publications, a further term should be introduced

5. Conclusions

in the viscosity in order to account for the -totally unsteady- orientation of erythrocytes in presence of magnetic field but also dependent of the flow conditions. This additional contribution, known as the magnetoviscous term, has been statistically obtained by [2] and also considered in this investigation, where interesting conclusions of its inclusion have been obtained.

Besides, depending on the location of the blood vessel (but also the vessel geometry), the velocity inlet function will vary along time. The closer it is to the heart, the more intense the blood pulse will be, and consequently its variation along time. This is why, the constant-in-time spatially – parabolic velocity inlet has now been replaced by a pulsatile velocity inlet whilst maintaining the Poiseuille distribution in the spatial domain. This new waveform has been constructed with, using as reference the real pulse from a healthy patient, mathematical means so as to obtain a really high-fidelity mathematical function of the inlet of an aorta. Comparing with the functions used in investigations, this new function entails a significantly more accurate model. But, importantly, special differences have been noted with the assumption of using time-constant velocity profile in the inflow which will be summarized in the following paragraphs.

The final section of the Multiphysics investigation implies the study of the convective instability of the blood flow, first separately and then in conjunction with the FHD/MHD effect. For the first, the magnetic field is disabled whilst for the second subsection it is accordingly considered again. Here, as it has happened in many of the prior sections, errors have been sighted in the Tzirtzilakis blood model hence they have been properly amended with more accurate values. The Rayleigh-Bénard convection has been studied under the basis of the linear stability theory which uses the Rayleigh number Ra to serve as threshold between stable and unstable flow. A parametric study has been carried out on the convective instability alone to then understand how the RBI and MHD/FHD effects interact. The solid conclusions regarding these phenomena will be soon explained.

5.2 Validation and FHD/MHD Effects

Both flow traits are consequence, first, of the magnetization curve that suffer the erythrocytes circulating in the core of the blood cells (FHD) and also the Lorentz Force created by the plasma ions circulating in a perpendicular direction to the applied magnetic field. Whilst the first will only take place where a gradient of the magnetic field is present (especially in the beginning and end of it), the other will influence the flow along the whole region

5. Conclusions

in which this last is applied. The two effects will consequently have a dissipative effect modelled in the energy equation as well, representing the phenomena which are known, respectively, as magneto-caloric effect (FHD) and the Joule effect (MHD). In fact, minor dissipative effects such as the skin effect do take place here but will not be considered due to their negligible contribution.

The shear-thinning basic nature of blood has been modelled by using simple power-law non-newtonian model with its characteristic parameters set by Least Square adjustment to real blood flow. The intensity of the applied magnetic field, being evaluated from 2 to 10 T, plays an important role in the results. As this is increased, both MHD and FHD effects increase. Whilst the first one has a tendency to curve the flow, the second one introduces two main vortexes which accelerate the flow and also create recirculation regions next to the walls where reverse flow is witnessed with a proportionality to the magnetic field intensity. Results from these simulations are in good agreement with similar conclusions reached by Tzirtzilakis et al and by Tzirakis et al. The presence of these vortexes, if the direct application in the medical field is considered, evidences the remarkable perturbation of the blood flow particularly considering that MRI devices oscillate between 0.4 to 6 T but for animal investigations even rise up to 10 T. If multiphase hemodynamic is considered, in the stagnation regions formed the Roleaux effect will be enhanced and therefore blood coagulation is more prone to happen. This effect is totally undesired as it can be fatal for a human being, hence, in blood flows denser than usual or with more LDL concentration, a risk by using MRI devices or Magnetic Drug Targetting is consequently introduced.

5.3 Non-Newtonian Modelling for Blood Shear-Thinning behaviour

Blood possesses a particular shear-thinning behaviour which is totally noticeable at very low shear rates but tends to the usual Newtonian viscosity formulation when high shear rates are present. If it is said in another manner, blood will entail a very viscous flow if it is not stressed by external forces or movements but will flow more easily as shear contributions are introduced to the domain. To yield this effect, several Non-Newtonian Models have been developed and particularized to blood flow depending on the attributes considered in them (viscoelasticity, viscoplasticity, etc.). According to literature, the most successful in describing the blood flow have been the Casson-type family and also latest investigations have recognized Quemada model as a very versatile and powerful model as well. Hence, in this section, the Newtonian, Simple Power-Law from the previous section, Casson-standard, Casson modified, Casson K-L and Quemada models are conveniently

5. Conclusions

evaluated in conjunction with the FHD/MHD effects.

All the models represent similar flow variable contours as the shear rate is considered to be in a high regime. However, important differences have been noted with the Power-Law model and some minor with the Quemada model. Here mixing phenomena is notably sighted after the second vortex in contrast with the figures that have been shown in the previous section. The reason beneath the important difference between Newtonian Model and Casson-type with Power-Law is due to the Simple Power-Law incapability to approach the Newtonian regime at high shear rates. When velocity profiles are compared in different sections along the x-axis, it has been shown that Simple Power-Law systematically underpredicts the intensity of the flow but also demonstrates more resistance to leave the parabolic spatial distribution. This is why, accordingly with other investigations such as [13], it will be concluded that the Simple Power-Law is not successful at high shear rates.

On the other hand, less deviations from the average profile have been noted with the Quemada model even though they are not practically visible in the flow variables contours, only in the velocity profiles at different sections. The Quemada model assumes a less blunt velocity parabola than the other methods, therefore the slight variations noticed. However, real multiphase hemodynamics show that multiphase entails a blunter parabolic profile than the assumed in the Poiseouille flow, hence it can be thought that Quemada Model, even though of its power and versatility, supposes a worse fit to the real flow than the Casson family, which is closer to the Newtonian Model. Interestingly enough, when the Wall Shear Stress values are computed in the top and bottom walls, the Quemada model predicts a more intense distribution as the vortex predicted are slightly closer to the walls. However, this conclusion needs the confirmation of more experimental investigations in order to acquire more solidity.

As it has been said, Casson-type models seem to have a more accurate prediction to the real flow and are the best approach to the Newtonian assumption. Logically, Modified Casson and particularly K-L model are the best descriptors since they represent an enhancement of the standard model, which might need three-scope functions to fit the three regimes of shear. The conclusions regarding this section have been supported by a deviation statistical study and show great consistence with similar investigations. The models chosen represent a really accurate behaviour of the real blood flow. However, thixotropy effects noted in experimental research strongly suggest the enhancement of the blood flow mathematical model which -by now- is not able to yield this trait. Hence, in a future, this Non-Newtonian models will be soon replaced when simulating blood cases.

5. Conclusions

5.4 Apparent viscosity change due to erythrocyte orientation

Yielding the experimental results from [2] and the simulations from [18] a noticeable change in blood effective viscosity (through a viscometer) is found at "in vitro" tests when it faces magnetic fields. Currently, it is thought that the reason behind this effect may be the RBC orientation change as a result of the magnetization. Therefore, in zones where fluid is more stagnated it will imply an additional resistance to flow (more effective or apparent viscosity) but in some other places it will flow more easily as a result of this orientation. This differential trait has been quantified and an experimental function through Least Squares Non-Linear Regression has been obtained.

In the research papers previously mentioned, a variation of up to a 10% of the flow variable magnitudes have been noted, and in here similar conclusions have been derived. In our problem, the mean flow presents a bigger effective viscosity (noticeable by the minimum extrema) but also entails slightly less maximum values. This fact can answer for the variations presented in velocity, vorticity and temperature contours. Besides, it is curious to note how, compared to the baseline viscosity model, it predicts with higher intensity the first vortex rather than the second. This feature is consistent with the logical reasoning since, as flow is perturbed by the magnetic field, it supposes more effort to introduce further perturbations, which is not likely to happen in a localized constant magnetic field.

5.5 High-Fidelity Aorta Velocity Function

The results obtained by using a really accurate systole-diastole cycle velocity inlet (particularized in the aorta region) show great differences with the time-constant function used in a wide variety of investigations but also in the ones carried out until this section. Here, the setup has been the same than in the first section but by introducing this real-case pulsatile inflow, but also without the application of the localized magnetic field. Thus, more accurate comparison of the real effect will be now obtained. In the systolic stage, where the highest velocity magnitude and pressure of the flow is onset, the region of maximum values is slightly higher in the case where FHD and MHD effects are considered, even though this difference is barely perceivable. On the other hand, in the point where it achieves its minimum value, in the relaxation or diastole phase, more intense velocity magnitude is present again when the magnetic field is applied.

Now, from diastole to the systole of the next period, a quasi-constant in time velocity profile will derive interesting conclusions. while the no MHD and no FHD assumption

5. Conclusions

simulation does develop a nearly constant velocity pattern, accentuating the value near the inlet and walls, the simulation with the magnetic field presents a similar distribution but with intenser cores as a result of the tiny vortex cores introduced by the FHD phenomenon. One vortex is located next to the upper wall and the second immediately above the lower wall. Initially, the upper vortex core is more intense, but as time goes by, it derives energy to the second core through dissipation, until the period is restarted.

The traits described are common in all the periods. Nonetheless, it is curious to note that results from one period to another vary slightly, inducing marginally more intense vortex cores and velocity contours with faintly bigger magnitude as time goes by. These simulations show that, even though the FHD/MHD effect is noticeable, it is not as strong as it has been obtained in the previous cases and similar investigations as vorticity is swiped at every cycle. The maximum effect is only onset in the diastole and its posterior quasi-constant state. Given that each period lasts 0.8 s, coagules are less likely to happen than predicted. However, this is only applicable to the aorta artery due to its proximity to the heart, since, the further the vessel is located, this cyclic nature will subsequently loose strength to be more alike the first section.

5.6 Rayleigh-Bénard Convective Instability

Two blood models have been evaluated, one by using Tzirtzilakis model from [12] and the other by performing some correction on its values. In both cases, the Rayleigh number for the geometry and considering 1 K gradient of temperature (being hotter in the lower wall) is remarkably higher than the critical value of 1708, hence blood is likely to onset the convective instability. Interestingly enough, the Rayleigh number (Ra) of the corrected flow is higher than the Tzirtzilakis model, hence one could think that the instability would take place faster and with more intensity. However, results actually prove the opposite. Whilst for the Tzirtzilakis flow Bénard Cells are perfectly formed and then disappear through diffusion, in the amended model, this instability takes more time to be triggered and it is only onset partially. This is due to the really low specific heat of the Tzirtzilakis model and the high value of conductivity. Thus, an important deduction which is not evident has been obtained: the higher Rayleigh number -specially comparing two different fluids or models- will not imply faster instability development or higher intensity, it will just indicate that flow is assumed to be in the unstable regime and Rayleigh-Bénard convection is likely to happen. However for the same model or fluid, if the height parameter is increased, such as the temperature gradient or gravity, the

5. Conclusions

instability will be developed faster and indeed more energetic. This conclusion is held by the thermal-variation cases simulated in the results section.

Moreover, differences between Laminar and Turbulent Flows (using $k-\varepsilon$ realizable model) have been obtained. Turbulence, contrary to the Laminar case, develops a sudden and more unstable pattern which evolves with some random nature, high unpredictability and vortexes vary their shape to elliptic morphology. Structures appear and disappear to form others or split into different, which is indeed not presented in the stability of the Bénard cells of the Laminar case. Even though the instability seems to be onset faster, it also seems to, eventually, loose its strength by dissipation in a quicker rate. These characteristics were totally expected and are in good agreement with the work from [93].

5.7 Rayleigh-Bénard Convective Instability in conjunction with Ferro and magneto-hydrodynamic effects

When both effects are coupled, it seems that, for 1 K of temperature gradient, the FHD and MHD effects are predominant hence within less than a second the steady-state results are achieved for almost all the flow variables except for temperature, which evolves in time and showing a mild convection. The temperature profile will logically roll over the two vortex cores due to their stronger influence of the blood flow. Notwithstanding, as it has been demonstrated, a more adverse temperature gradient forces the apparition of secondary patterns and vortexes due to the Rayleigh-Bénard convection. These ones, initially will be vague and will definitely reinforce the vortexes of the FHD/MHD effect such as it can be seen in the $\Delta T = 50K$. If the convection is further forced with more intense gradients of temperature between both plates, in the end, both effects will be at the same order of magnitudes and a strong pattern of both instabilities will be presented. This will mainly affect to the region where the localized magnetic field is present but streamlines evidence how small and weak vortexes are triggered in the whole domain, accompanying the two strong causing by the additive behaviour both of MHD/FHD and RBI. This trait was previously noticed, even though it was by only considering the FHD term, by Finlayson at [23] where magnetic and convective instabilities were conjectured to multiply their contribution. Hence results of both their and our investigation seem to result in similar conclusions.

5. Conclusions

5.7.1 Final Ideas and Future Work

The ability to capture very complex phenomena, such as the eddies witnessed in most of the plots (particularly regarding the plots from Rayleigh-Bénard Convection), with low-order schemes is indeed one of the surprising outcomes of the study. The magnetic field influence in blood has been numerically quantified, but also the influence of the variation of other flow parameters such as temperature, velocity, turbulence, etc. The performance of -considered by literature- very accurate Non-Newtonian models for this fluid has been examined as well. And also the RBI instability evaluated here for blood flows, even with Magnetic Field influence coupling, has not been sighted in recent research. In this sense, and given the time and situation in which these results have been obtained, considerable and interesting conclusions have been deduced from this work.

However, the scope of the blood flow modelling problem is wide enough so as to constantly enhance the work performed. More simulations over different geometries, cases, and magnetic fields applied could be analyzed. Furthermore, a Grid Convergence Study would also be interesting to conduct especially for those simulations in which reference data is not available. Nevertheless, many other more strong ideas have aroused during the elaboration of this research. A very attractive idea is the coupling of the MHD/FHD mono-phase effects with multi-phase hemodynamics that would certainly suppose a big step to a more accurate simulation and blood flow modelling. Also, the substitution of magnetic fields with unsteady electrodynamic waves would also be an interesting case to consider. And eventually, Non-Newtonian models will be replaced by models which consider thixotropy accurately and are still waiting to be developed.

Bibliography

- [1] EE Tzirtzilakis, M Xenos, VC Loukopoulos, and NG Kafoussias. Turbulent biomagnetic fluid flow in a rectangular channel under the action of a localized magnetic field. *International Journal of Engineering Science*, 44(18-19):1205–1224, 2006.
- [2] Yousef Haik, Vinay Pai, and Ching-Jen Chen. Apparent viscosity of human blood in a high static magnetic field. *Journal of Magnetism and Magnetic Materials*, 225(1-2):180–186, 2001.
- [3] Russell K Hobbie and Bradley J Roth. *Intermediate physics for medicine and biology*. Springer Science & Business Media, 2007.
- [4] Anna Marcinkowska-Gapińska, Jacek Gapinski, Waldemar Elikowski, Feliks Jaroszyk, and Leszek Kubisz. Comparison of three rheological models of shear flow behavior studied on blood samples from post-infarction patients. *Medical biological engineering computing*, 45:837–44, 10 2007.
- [5] Johannes Soulis, Dimitrios Fytanidis, Vassilios Papaioannou, Charis Styliadis, and George Giannoglou. Oscillating ldl accumulation in normal human aortic arch - shear dependent endothelium. *Hippokratia*, 15:22–5, 03 2011.
- [6] Albert L Lehninger, David L Nelson, Michael M Cox, et al. *Lehninger principles of biochemistry*. Macmillan, 2005.
- [7] Gillian Pocock, Christopher D Richards, and David A Richards. *Human physiology*. Oxford university press, 2013.
- [8] KESAVA REDDY, M REDDY, and R REDDY. Mathematical model governing magnetic field effect on bio magnetic fluid flow and orientation of red blood cells. *Pac.-Asian J. Math*, 5:344–356, 2011.
- [9] RE Rosensweig. *Ferrohydrodynamics* cambridge university press cambridge. *New York, Melbourne*, 1985.

Bibliography

- [10] YOUSEF Haik, V Pai, and CJ Chen. Biomagnetic fluid dynamics. *Fluid dynamics at interfaces*, pages 439–452, 1999.
- [11] Hannes Alfven. A new type of wave motion and its importance in solar physics. *Acta radiologica*, (3-4):228–242, 1946.
- [12] EE Tzirtzilakis. A mathematical model for blood flow in magnetic field. *Physics of fluids*, 17(7):077103, 2005.
- [13] Safoora Karimi, Mahsa Dabagh, Paritosh Vasava, Mitra Dadvar, Bahram Dabir, and Payman Jalali. Effect of rheological models on the hemodynamics within human aorta: Cfd study on ct image-based geometry. *Journal of Non-Newtonian Fluid Mechanics*, 207:42–52, 2014.
- [14] P NITHIARASU. Biofluid dynamics and biofluid-structure interaction. *International journal for numerical methods in fluids*, 57(5), 2008.
- [15] William F Hughes and Frederick John Young. The electromagnetodynamics of fluids. *elfl*, 1966.
- [16] MD Cowley and Ronald E Rosensweig. The interfacial stability of a ferromagnetic fluid. *Journal of Fluid mechanics*, 30(4):671–688, 1967.
- [17] LD Landau and EM Lifshitz. Fluid mechanics pergammon. *New York*, 61, 1959.
- [18] Konstantinos Tzirakis, Lorenzo Botti, Vasileios Vavourakis, and Yannis Papaharilaou. Numerical modeling of non-newtonian biomagnetic fluid flow. *Computers & Fluids*, 126:170–180, 2016.
- [19] Noriko Iida. Influence of plasma layer on steady blood flow in microvessels. *Japanese Journal of Applied Physics*, 17(1):203, 1978.
- [20] Suhas V Patankar. A calculation procedure for two-dimensional elliptic situations. *Numerical heat transfer*, 4(4):409–425, 1981.
- [21] Lorenzo Botti and Daniele A Di Pietro. A pressure-correction scheme for convection-dominated incompressible flows with discontinuous velocity and continuous pressure. *Journal of computational physics*, 230(3):572–585, 2011.
- [22] Gianluca De Santis, Peter Mortier, Matthieu De Beule, Patrick Segers, Pascal Verdonck, and Benedict Verhegghe. Patient-specific computational fluid dynamics: structured mesh generation from coronary angiography. *Medical & biological engineering & computing*, 48(4):371–380, 2010.

Bibliography

- [23] BA Finlayson. Convective instability of ferromagnetic fluids. *Journal of Fluid Mechanics*, 40(4):753–767, 1970.
- [24] CP Bean. Hysteresis loops of mixtures of ferromagnetic micropowders. *Journal of Applied Physics*, 26(11):1381–1383, 1955.
- [25] Peter J Stiles and Michael Kagan. Thermoconvective instability of a ferrofluid in a strong magnetic field. *Journal of colloid and interface science*, 134(2):435–448, 1990.
- [26] Rohit Goel and Pushpendra Vashishtha. On the stability of rayleigh – benard convection in a micropolar fluid. *Paripex - Indian Journal Of Research*, 3:1–2, 01 2012.
- [27] A Cemal Eringen. Theory of micropolar fluids. *Journal of Mathematics and Mechanics*, pages 1–18, 1966.
- [28] Subrahmanyam Chandrasekhar. *Hydrodynamic and hydromagnetic stability*. Courier Corporation, 2013.
- [29] Subbarama Pranesh, Rojipura V Kiran, et al. Study of rayleigh-bénard magneto convection in a micropolar fluid with maxwell-cattaneo law. *Applied mathematics*, 1(06):470, 2010.
- [30] Annamma Abraham. Rayleigh–benard convection in a micropolar ferromagnetic fluid. *International journal of engineering science*, 40(4):449–460, 2002.
- [31] N Rudraiah, IS Shivakumara, and CE Nanjundappa. Effect of basic temperature gradients on marangoni convection in ferromagnetic fluids. 2002.
- [32] PG Siddheshwar, C Kanchana, Y Kakimoto, and A Nakayama. Steady finite-amplitude rayleigh–bénard convection in nanoliquids using a two-phase model: theoretical answer to the phenomenon of enhanced heat transfer. *Journal of Heat Transfer*, 139(1), 2017.
- [33] BS Bhaduria, I Hashim, and PG Siddheshwar. Effect of internal-heating on weakly non-linear stability analysis of rayleigh–bénard convection under g-jitter. *International Journal of Non-Linear Mechanics*, 54:35–42, 2013.
- [34] IS Shivakumara, N Rudraiah, and CE Nanjundappa. Effect of non-uniform basic temperature gradient on rayleigh–benard–marangoni convection in ferrofluids. *Journal of magnetism and magnetic materials*, 248(3):379–395, 2002.

Bibliography

- [35] F Franchi and B Straughan. Continuous dependence on the relaxation time and modelling, and unbounded growth, in theories of heat conduction with finite propagation speeds. *Journal of Mathematical Analysis and Applications*, 185(3):726–746, 1994.
- [36] A Vikhansky. Thermal convection of a viscoplastic liquid with high rayleigh and bingham numbers. *Physics of Fluids*, 21(10):103103, 2009.
- [37] Alexander Vikhansky. On the stopping of thermal convection in viscoplastic liquid. *Rheologica acta*, 50(4):423–428, 2011.
- [38] Wubshet Ibrahim and OD Makinde. Magnetohydrodynamic stagnation point flow and heat transfer of casson nanofluid past a stretching sheet with slip and convective boundary condition. *Journal of Aerospace Engineering*, 29(2):04015037, 2016.
- [39] Osman Turan, Nilanjan Chakraborty, and Robert J Poole. Laminar rayleigh-bénard convection of yield stress fluids in a square enclosure. *Journal of Non-Newtonian Fluid Mechanics*, 171:83–96, 2012.
- [40] H Yamaguchi, Z Zhang, S Shuchi, and K Shimada. Heat transfer characteristics of magnetic fluid in a partitioned rectangular box. *Journal of Magnetism and Magnetic Materials*, 252:203–205, 2002.
- [41] Zineddine Kebiche, Cathy Castelain, and Teodor Burghelea. Experimental investigation of the rayleigh-bénard convection in a yield stress fluid. *Journal of Non-Newtonian Fluid Mechanics*, 203:9–23, 2014.
- [42] Bashar Albaalbaki and Roger E Khayat. Pattern selection in the thermal convection of non-newtonian fluids. *Journal of fluid mechanics*, 668:500, 2011.
- [43] SF Liang and A Acrivos. Experiments on buoyancy driven convection in non-newtonian fluid. *Rheologica Acta*, 9(3):447–455, 1970.
- [44] J Zhang, D Vola, and IA Frigaard. Yield stress effects on rayleigh-bénard convection. *Journal of Fluid Mechanics*, 566:389, 2006.
- [45] Maithili Sharan and Aleksander S Popel. A two-phase model for flow of blood in narrow tubes with increased effective viscosity near the wall. *Biorheology*, 38(5, 6):415–428, 2001.
- [46] Axel R Pries, Timothy W Secomb, P Gaehtgens, and JF Gross. Blood flow in microvascular networks. experiments and simulation. *Circulation research*, 67(4):826–834, 1990.

Bibliography

- [47] AE Medvedev and VM Fomin. Two-phase blood-flow model in large and small vessels. *56*(12):610–613, 2011.
- [48] Jacopo Buongiorno. Convective transport in nanofluids. 2006.
- [49] DY Tzou. Instability of nanofluids in natural convection. *Journal of Heat Transfer*, 130(7), 2008.
- [50] DY Tzou. Thermal instability of nanofluids in natural convection. *International Journal of Heat and Mass Transfer*, 51(11-12):2967–2979, 2008.
- [51] DA Nield and AV Kuznetsov. Thermal instability in a porous medium layer saturated by a nanofluid. *International Journal of Heat and Mass Transfer*, 52(25-26):5796–5801, 2009.
- [52] Chittin Tangthieng, Bruce A Finlayson, John Maulbetsch, and Tahir Cader. Heat transfer enhancement in ferrofluids subjected to steady magnetic fields. *Journal of Magnetism and Magnetic Materials*, 201(1-3):252–255, 1999.
- [53] Suzanne M Snyder, Tahir Cader, and Bruce A Finlayson. Finite element model of magnetoconvection of a ferrofluid. *Journal of Magnetism and Magnetic Materials*, 262(2):269–279, 2003.
- [54] G Vaidyanathan, R Sekar, R Vasanthakumari, and A Ramanathan. The effect of magnetic field dependent viscosity on ferroconvection in a rotating sparsely distributed porous medium. *Journal of Magnetism and Magnetic materials*, 250:65–76, 2002.
- [55] Erica Cherry and John Eaton. Simulation of magnetic particles in the bloodstream for magnetic drug targeting applications. *APS*, pages L11–001, 2012.
- [56] Krishna Sriram, Amy G Tsai, Pedro Cabrales, Fantao Meng, Seetharama A Acharya, Daniel M Tartakovsky, and Marcos Intaglietta. Peg-albumin supraplasma expansion is due to increased vessel wall shear stress induced by blood viscosity shear thinning. *American Journal of Physiology-Heart and Circulatory Physiology*, 302(12):H2489–H2497, 2012.
- [57] DE Brooks, JW Goodwin, and GV Seaman. Interactions among erythrocytes under shear. *Journal of Applied Physiology*, 28(2):172–177, 1970.
- [58] Kar W Yung, Peter B Landecker, and Daniel D Villani. An analytic solution for the force between two magnetic dipoles. *Magnetic and electrical Separation*, 9, 1970.

Bibliography

- [59] P Kopcansky, M Timko, M Hnatic, M Vala, GM Arzumanyan, EA Hayryan, L Jancurova, and J Jadlovsky. Numerical modeling of magnetic drug targeting. *Physics of Particles and Nuclei Letters*, 8(5):502, 2011.
- [60] PA Voltairas, DI Fotiadis, and LK Michalis. Hydrodynamics of magnetic drug targeting. *Journal of Biomechanics*, 35(6):813–821, 2002.
- [61] Alex J Apostolidis, Adam P Moyer, and Antony N Beris. Non-newtonian effects in simulations of coronary arterial blood flow. *Journal of Non-Newtonian Fluid Mechanics*, 233:155–165, 2016.
- [62] David A Johnson, Ulhas P Naik, and Antony N Beris. Efficient implementation of the proper outlet flow conditions in blood flow simulations through asymmetric arterial bifurcations. *International journal for numerical methods in fluids*, 66(11):1383–1408, 2011.
- [63] A Bar-Cohen and WM Rohsenow. Thermally optimum spacing of vertical, natural convection cooled, parallel plates. 1984.
- [64] Terumasa Higashi, Akio Yamagishi, Tetsuya Takeuchi, Naomasa Kawaguchi, S Sagawa, S Onishi, and M Date. Orientation of erythrocytes in a strong static magnetic field. 1993.
- [65] Tian Ma, Shouhong Wang, et al. Rayleigh bénard convection: dynamics and structure in the physical space. *Communications in Mathematical Sciences*, 5(3):553–574, 2007.
- [66] Shewaferaw S Shibeshi and William E Collins. The rheology of blood flow in a branched arterial system. *Applied Rheology*, 15(6):398–405, 2005.
- [67] PD Ballyk, DA Steinman, and CR Ethier. Simulation of non-newtonian blood flow in an end-to-side anastomosis. *Biorheology*, 31(5):565–586, 1994.
- [68] Barbara M Johnston, Peter R Johnston, Stuart Corney, and David Kilpatrick. Non-newtonian blood flow in human right coronary arteries: transient simulations. *Journal of biomechanics*, 39(6):1116–1128, 2006.
- [69] Yotsakorn Pratumwal, Wiroj Limtrakarn, Sombat Muengtaweepongsa, Phatsawadee Phakdeesan, Suttiprak Duangburong, Patipath Eiamaram, and Kannakorn Intharakham. Whole blood viscosity modeling using power law, casson, and carreau yasuda models integrated with image scanning u-tube viscometer technique. *Songklanakarin Journal of Science & Technology*, 39(5):625–31, 2017.

Bibliography

- [70] M. Casson. The rheology of disperse systems. *Pergamon Press*, 1959.
- [71] X. Luo and D.N. Schramm. Fractals and cosmological large-scale structure. *Science*, 256(5056):513–515, 1992.
- [72] Wen-Jei Yang. *Biothermal-fluid sciences: principles and applications*. Garland Science, 1989.
- [73] XY Luo and ZB Kuang. A study on the constitutive equation of blood. *Journal of biomechanics*, 25(8):929–934, 1992.
- [74] Jian-Bao Zhang and Zhen-Bang Kuang. Study on blood constitutive parameters in different blood constitutive equations. *Journal of Biomechanics*, 33(3):355–360, 2000.
- [75] Yuan-Cheng Fung. Mechanical properties and active remodeling of blood vessels. In *Biomechanics*, pages 321–391. Springer, 1993.
- [76] JR Buchanan, C Kleinstreuer, S Hyun, and GA Truskey. Hemodynamics simulation and identification of susceptible sites of atherosclerotic lesion formation in a model abdominal aorta. *Journal of biomechanics*, 36(8):1185–1196, 2003.
- [77] A Razavi, E Shirani, and MR Sadeghi. Numerical simulation of blood pulsatile flow in a stenosed carotid artery using different rheological models. *Journal of biomechanics*, 44(11):2021–2030, 2011.
- [78] Daniel Quemada. Blood rheology and its implication in flow of blood. In *Arteries and arterial blood flow*, pages 1–127. Springer, 1983.
- [79] Panagiotis Neofytou and Dimitris Drikakis. Non-newtonian flow instability in a channel with a sudden expansion. *Journal of Non-Newtonian Fluid Mechanics*, 111(2):127 – 150, 2003.
- [80] D Lerche, H Bäumler, W Kucera, W Meier, and M Paulitschke. Flow properties of blood and hemorheological methods of quantification. *Physical Characterization of Biological cells. Basic research and clinic relevance*. Ed. W. Scütt, H. Klinkmann, I. Lamprecht, T. Wilson, Verlag Gesundheit GmbH Berlin, pages 189–214, 1991.
- [81] Marian Smoluchowski. Drei vorträge über diffusion, brownsche molekularbewegung und koagulation von kolloidteilchen. *Pisma Mariana Smoluchowskiego*, 2(1):530–594, 1927.
- [82] R.W. Samsel and A.S. Perelson. Kinetics of rouleau formation. i. a mass action approach with geometric features. *Biophysical Journal*, 37(2):493 – 514, 1982.

Bibliography

- [83] Axel R Pries, D Neuhaus, and P Gaehtgens. Blood viscosity in tube flow: dependence on diameter and hematocrit. *American Journal of Physiology-Heart and Circulatory Physiology*, 263(6):H1770–H1778, 1992.
- [84] Suhas Vasant PATANKAR and Dudley Brian Spalding. *A calculation procedure for the transient and steady-state behaviour of shell-and-tube heat exchangers*. Imperial College of Science and Technology, Department of Mechanical Engineering, 1972.
- [85] Joel H Ferziger, Milovan Perić, and Robert L Street. *Computational methods for fluid dynamics*, volume 3. Springer, 2002.
- [86] B.E. Launder and B.I. Sharma. Application of the energy-dissipation model of turbulence to the calculation of flow near a spinning disc. *Letters in Heat and Mass Transfer*, 1(2):131 – 137, 1974.
- [87] W.P Jones and B.E Launder. The prediction of laminarization with a two-equation model of turbulence. *International Journal of Heat and Mass Transfer*, 15(2):301 – 314, 1972.
- [88] Sami Gabriel, RW Lau, and Camelia Gabriel. The dielectric properties of biological tissues: Iii. parametric models for the dielectric spectrum of tissues. *Physics in medicine & biology*, 41(11):2271, 1996.
- [89] R.A. Frewer. The electrical conductivity of flowing blood. 1974.
- [90] Ilias Konstantinou. Numerical investigation of newtonian and non-newtonian biofluids in the presence of a uniform magnetic field for 2d non-isothermal laminar and turbulent flows. 2016.
- [91] Cristopher Adkins. Investigation of ferro- and magneto- hydrodynamic effects on non-isothermal turbulent fluid flow in a cuboid channel under the influence of a localised uniform magnetic field. 2018.
- [92] WL Siauw, EYK Ng, and J Mazumdar. Unsteady stenosis flow prediction: a comparative study of non-newtonian models with operator splitting scheme. *Medical engineering & physics*, 22(4):265–277, 2000.
- [93] Ambrish Pandey, Janet D Scheel, and Jörg Schumacher. Turbulent superstructures in rayleigh-bénard convection. *Nature communications*, 9(1):1–11, 2018.
- [94] Yoed Rabin and Joseph Plitz. Thermal expansion of blood vessels and muscle specimens permeated with dmso, dp6, and vs55 at cryogenic temperatures. *Annals of Biomedical Engineering*, 33(9):1213–1228, 2005.

Bibliography

- [95] HELMUT Hinghofer-Szalkay. Volume and density changes of biological fluids with temperature. *Journal of applied physiology*, 59(6):1686–1689, 1985.

Chapter 6

Appendix

6.1 Appendix 1. Convergence Study. Residual Plots

In the whole document converged results have been assumed as residuals of the equations did stabilize at very low values at most of the cases. Here, evidence of the convergence through the residual plots will be provided.

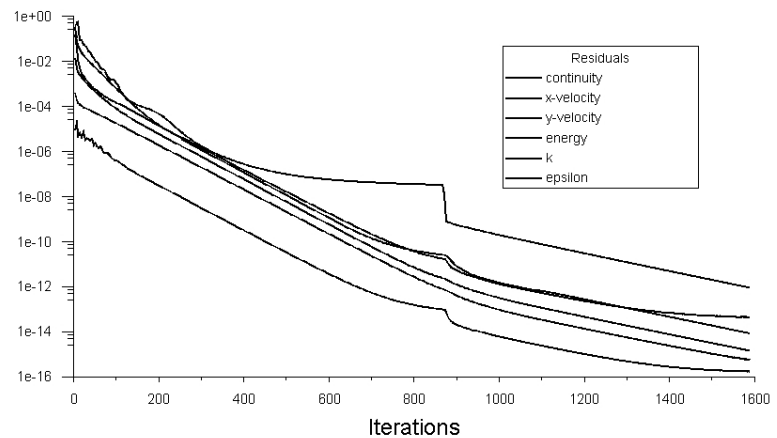


Figure 6.1: Residual Plot for $B=2$ T

6. Appendix

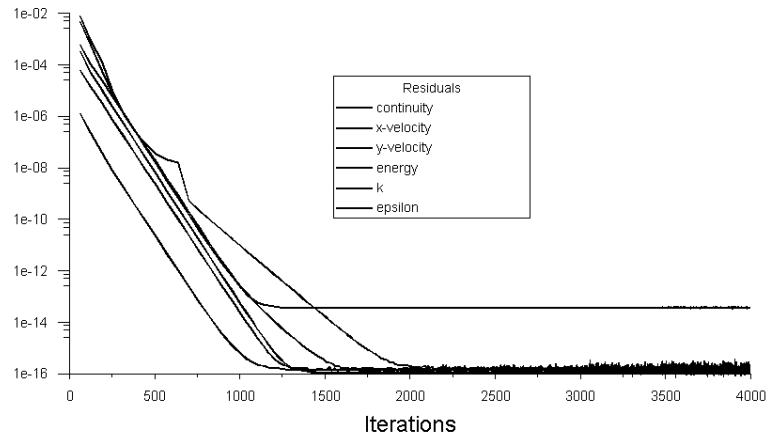


Figure 6.2: Residual Plot for $B=10$ T

The Validation Cases where FHD and MHD effects were implemented and evaluated for different magnetic field induction ($B=2$, $B=4$, $B=6$, $B=8$, $B=10$) do show overall similar convergence plots such as Figure 6.1 ($B=2$ T) and Figure 6.2 ($B=10$ T) demonstrate. It seems that, for $B=2$ T, the method did struggle a bit more to achieve really low residual values ($1e-15$) but at around $1e-12$ are still acceptable.

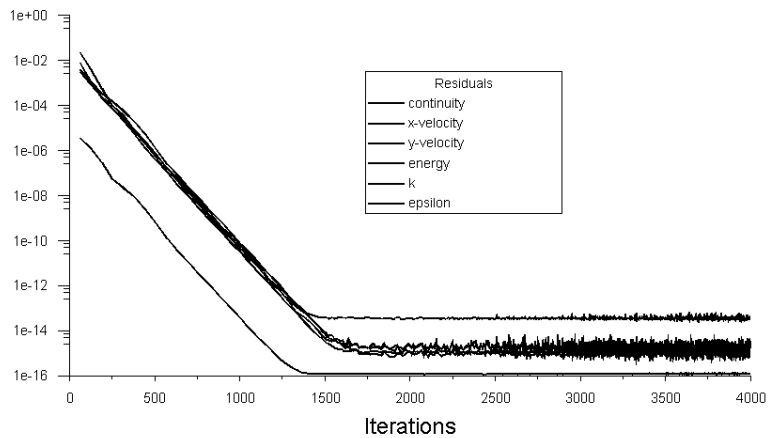


Figure 6.3: Residual Plot for Newtonian Model

6. Appendix

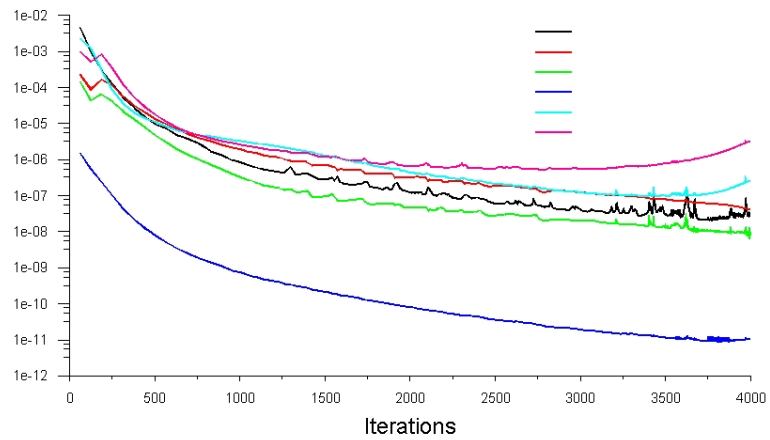


Figure 6.4: Residual Plot for Standard Casson Model

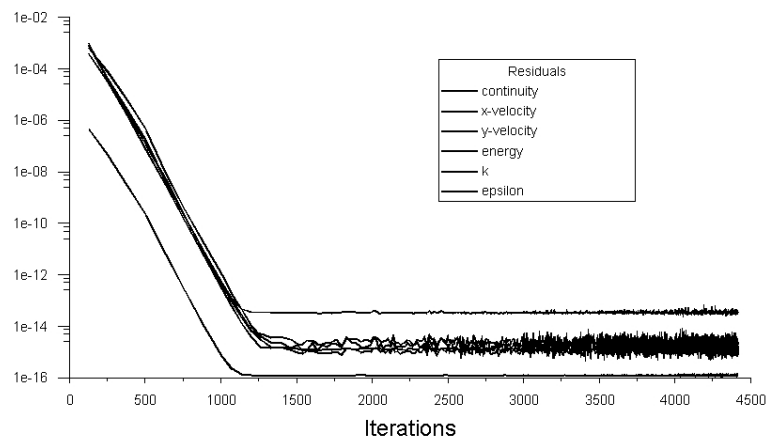


Figure 6.5: Residual Plot for Modified Casson Model

6. Appendix

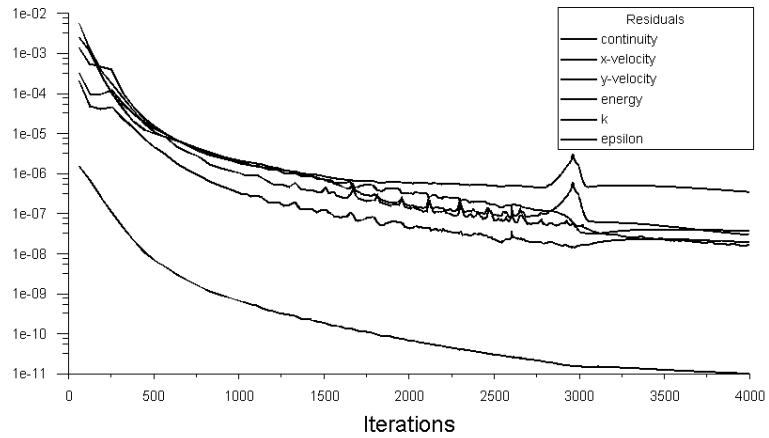


Figure 6.6: Residual Plot for K-L Casson Model

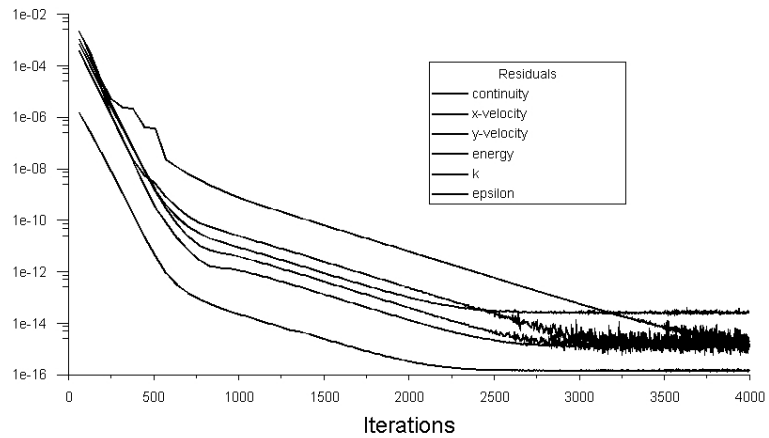


Figure 6.7: Residual Plot for Quemada Model

When the Non-Newtonian Models were evaluated, results did demonstrate the validity of the solutions as the flow variable contours show great consistency and similarity between one another. Most of the Models converge, averagely, with residuals at 1e-14 which is barely 0, probably fized by the own laptop power. However, Casson standard and K-L seem to have worse convergence as their residuals values tend to 1e-05 or 1e-06 which is still a decent value to consider converged results.

6. Appendix

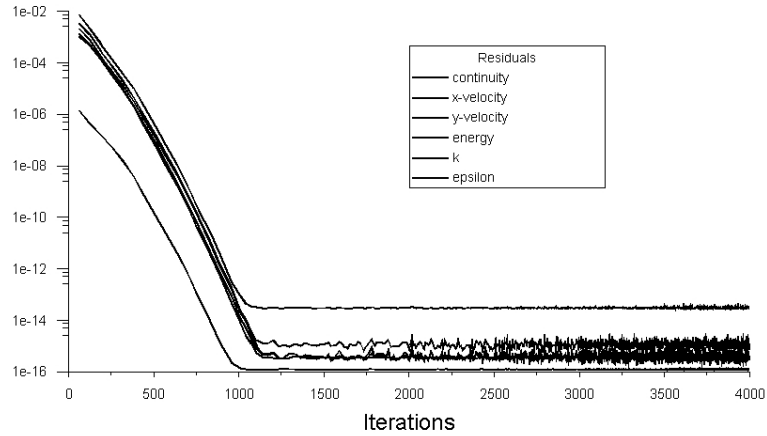


Figure 6.8: Residual Plot for the Magnetoviscous additional contribution

When the additional magnetoviscous contribution motivated by describing the orientation of RBC once applied the localized magnetic field was implemented, no remarkable issues have been introduced in the convergence of the solution, which is achieved quite fast after 1500 iterations.

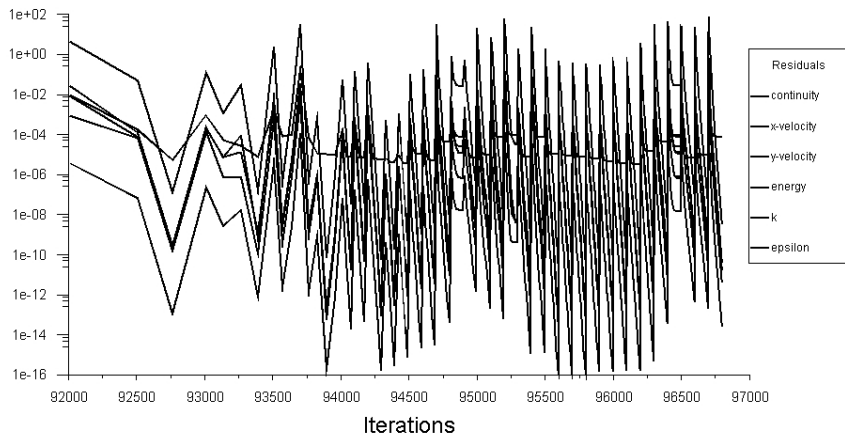


Figure 6.9: Residual Plot for Pulsatile Inflow

Here, where the pulsatile velocity was implemented, oscillations of values can be seen as a result of the transient simulation. In the end, the important value is not the average but the last value of each iteration, which is relatively low, around $1e-9$ as average.

6. Appendix

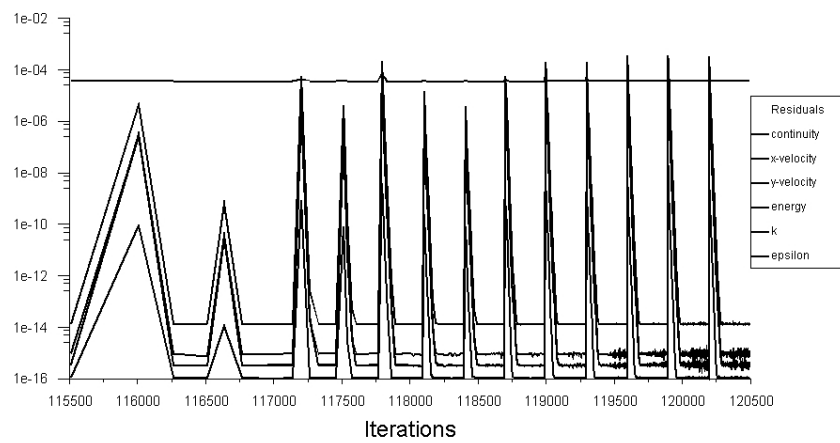


Figure 6.10: Residual Plot for Bénard-Rayleigh Convection

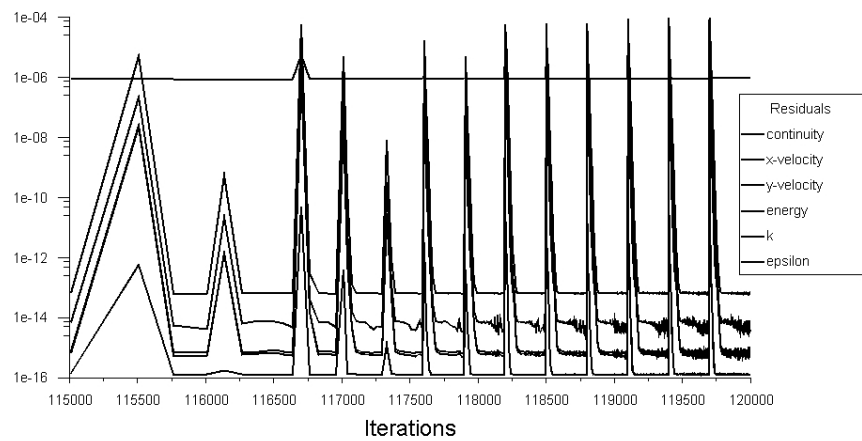


Figure 6.11: Residual Plot for Turbulent Bénard-Rayleigh Convection

6. Appendix

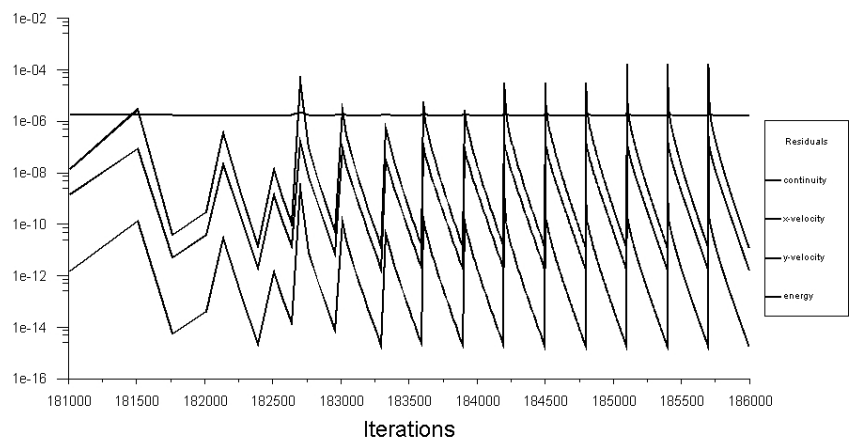


Figure 6.12: Residual Plot for Bénard-Rayleigh Convection in conjunction with FHD/MHD term

Finally, plots of the transient Rayleigh-Bénard Instability transient simulation demonstrate the good convergence of the solution, even though, when the FHD and MHD effects were introduced the convergence rate did slightly slow.

6. Appendix

6.2 Appendix 2. UDF Code

C:\Users\marcb\Desktop\Casson_Quemada_Magvis_Coupled.c

```
1  /
*-----*/
2 /* MHD-FHD UDF C Code for Solving Biofluid Flow Problems Using FLUENT      */
   Environment                           */
3  /
*-----*/
4 /* The original paper of Tzirzilakis and Loukopoulos (2005):                  */
   */
5  /
*-----*/
6 /* An Initial Version of the MHD-FHD code is Implemented by Dr. L. Könözsy '    */
   2015                                */
7  /
*-----*/
8 /* Example Code to Support Mr. Pietro Scienza MSc Thesis Project in AY          */
   2014/2015                            */
9  /
*-----*/
10 /* Corrections and New Feature Implementations by Mr. Marc Barcelo, 2020        */
   */
11  /
*-----*/
12
13 #include "udf.h"
14 #include "math.h"
15
16 /*
-----*/
17 /* H0                         Magnetic Field Strength                      */
   */
18 /* C_UDMI(c,cell_thread,0)  Magnetic Field Strength Intensity           */
   */
19 /* C_UDMI(c,cell_thread,1)  Magnetic Field Strength Intensity Gradient   */
   */
20 /*
-----*/
21
22 #define B    10.0              /* magnetic field (T) */
23
24 #define mu   3.2e-3            /* viscosity () */
25 /* Casson: eta_c 0.00414 tau_c 0.0038 / K-L: eta_c = 0.0035, tau_c=0.005,      */
   alpha_1=1, alpha_2=1.19523 / Modified Casson: eta_c = 0.002982,               */
   tau_c=0.002876, lambda= 4.02  */
26 #define eta_c 0.00414
27 #define tau_c 0.0038
```

```
28 #define lambda 4.020
29 #define alpha_one 1
30 #define alpha_two 1.19523
31 /*Quemada */
32 #define mu_f 1.2e-3
33 #define phi 0.45 /* haematocrit*/
34 #define gamma_c 5
35 #define k_inf 1.88
36 #define k_zero 4.33
37 /*Magnetoviscous Additive Term*/
38 #define alpha 0.9986
39 #define beta 0.01425
40
41 #define mu0 1.2566370614e-6      /* magnetic permeability of vacuum (H/m) */
42 #define k 1.832e-3                /* thermal diffusivity (W/m*K) */
43 #define L 0.65                   /* dimensional length (m) */
44 #define h 0.05                   /* dimensional height (m) */
45
46 #define a1 4.0                  /* magnetic field gradient coefficient 1 */
47 #define a2 4.0                  /* magnetic field gradient coefficient 2 */
48
49 #define x1 0.175                /* magnetic field start */
50 #define x2 0.4                  /* magnetic filed end */
51
52 #define sigma 0.8               /* Electrical conductivity (S/m) */
53 #define Tu 315.15                /* Upper Wall temperature (K) */
54 #define Tl 283.65                /* Lower Wall temperature (K) */
55
56 #define rho 1050.0
57
58 #define Re 400.0
59
60 /* B = 2 4 6 8 10 T */
61
62 #define MnM 62.5
63 /*#define MnM 2.5 10.0 22.5 40.0 62.5 */
64
65 #define MnF 2563.48
66 /*#define MnF 512.69 1025.39 1538.09 2050.78 2563.48 */
67
68 #define MnF_K_FACTOR_SCALE 1.0e-2
69
70 /* Magnetic Field Strength Intensity */
71 #define UDM_Hx 0
72 #define UDM_DHxDx 1
73 #define UDM_DHxDy 2
74
75 #define UDM_Hy 3
76 #define UDM_DHyDx 4
77 #define UDM_DHyDy 5
78
79 /* Applied Magnetic Field Induction */
80
```

```
81 #define UDM_Bx      6
82 #define UDM_DBxDx    7
83 #define UDM_DBxDy    8
84
85 #define UDM_By      9
86 #define UDM_DByDx   10
87 #define UDM_DByDy   11
88
89 #define UDM_B_Magnitude 12
90 #define UDM_DIMENSIONAL_TEMPERATURE_FIELD_FIXED 13
91 #define UDM_DIMENSIONLESS_TEMPERATURE_FIELD 14
92 #define shear_rate 15
93
94 /
*=====
=====
*/
95 /* DIMENSIONAL AND DIMENSIONLESS INITIALIZATION OF THE MAGNETIC FIELD
   STRENGTH INTENSITY (H-FIELD) */
96 /
*=====
=====
*/
97
98 DEFINE_INIT(initialization_H_field, domain)
99 {
100   cell_t cell_index;
101   Thread *cell_thread;
102
103   real xc[ND_ND], x, y, H0, By, DFDX, umax, K;
104
105   /*  $H0 = \sqrt{(\mu_0 \cdot \sigma) / (\rho \cdot \mu_0 \cdot h^2)}$ ; */
106
107   H0 = B/mu0;
108   umax = (Re*mu)/(rho*h);
109
110   thread_loop_c(cell_thread, domain)
111   {
112     begin_c_loop(cell_index, cell_thread)
113     {
114       C_CENTROID(xc, cell_index, cell_thread);
115
116       x = xc[0];
117
118       if((x >= x1) && (xc[0] <= x2))
119       {
120         /* MAGNETIC FIELD STRENGTH (H-FIELD) */
121         C_UDMI(cell_index, cell_thread, UDM_Hx) = (H0/2.0)*(tanh(a1*(x-x1))-tanh
122           (a2*(x-x2)));
123         C_UDMI(cell_index, cell_thread, UDM_DHxDx) = (H0/2.0)*((4.0*a1*cosh(a1*
124           (x-x1))*cosh(a1*(x-x1)))/((cosh(2.0*a1*(x-x1))+1.0)*(cosh(2.0*a1*(x-
125             x1))+1.0))-(4.0*a2*(cosh(a2*(x-x2))*cosh(a2*(x-x2))))/((cosh(2.0*a2*(
126               x-x2))+1.0)*(cosh(2.0*a2*(x-x2))+1.0)));
127         C_UDMI(cell_index, cell_thread, UDM_DHxDy) = 0.0;
128
129
130
131
132
133
134
135
136
137
138
139
140
141
142
143
144
```

```

C:\Users\marcb\Desktop\Casson_Quemada_Magvis_Coupled.c
125     C_UDMI(cell_index,cell_thread,UDM_Hy) = (H0/2.0)*(tanh(a1*(x-x1))-tanh
126         (a2*(x-x2)));
127     C_UDMI(cell_index,cell_thread,UDM_DHyDx) = (H0/2.0)*((4.0*a1*(cosh(a1*
128             (x-x1))*cosh(a1*(x-x1))))/((cosh(2.0*a1*(x-x1))+1.0)*(cosh(2.0*a1*(x-
129             x1))+1.0))-(4.0*a2*(cosh(a2*(x-x2))*cosh(a2*(x-x2))))/((cosh(2.0*a2*
130                 (x-x2))+1.0)*(cosh(2.0*a2*(x-x2))+1.0)));
131     C_UDMI(cell_index,cell_thread,UDM_DHyDy) = 0.0;
132
133 /* By is equal to constant does not trigger the vortices */
134 /* C_UDMI(cell_index,cell_thread,UDM_By) = By; */
135
136     C_UDMI(cell_index,cell_thread,UDM_By) = mu0*C_UDMI
137         (cell_index,cell_thread,UDM_Hy);
138     C_UDMI(cell_index,cell_thread,UDM_DByDx) = mu0*C_UDMI
139         (cell_index,cell_thread,UDM_DHyDx);
140     C_UDMI(cell_index,cell_thread,UDM_DByDy) = 0.0;
141 }
142 }
143
144 /*
145 *-----*/
146 /* INITIAL LINEAR TEMPERATURE DISTRIBUTION FROM THE LOWER WALL TO THE UPPER
147 *-----*/
148 /*-----*/
149 thread_loop_c(cell_thread,domain)
150 {
151     begin_c_loop(cell_index,cell_thread)
152     {
153         C_CENTROID(xc,cell_index,cell_thread);
154         y = xc[1];
155         C_T(cell_index,cell_thread) = Tl+(y/h)*(Tu-Tl);
156         C_UDMI(cell_index,cell_thread,UDM_DIMENSIONAL_TEMPERATURE_FIELD_FIXED) =
157             Tl+(y/h)*(Tu-Tl);
158         /* C_T(cell_index,cell_thread) = 0.0; */
159     } end_c_loop(cell_index,cell_thread)
160 }
161 /*-----*/
162 /* INITIAL DISTRIBUTION OF THE VELOCITY COMPONENTS (U,V) FROM THE LOWER
163 *-----*/

```

```
161  /
162  *-----*/
163  thread_loop_c(cell_thread, domain)
164  {
165  begin_c_loop(cell_index, cell_thread)
166  {
167  C_CENTROID(xc, cell_index, cell_thread);
168  y = xc[1];
169  C_U(cell_index, cell_thread) = 4.0*u_max*(y/h)*(1.0-(y/h));
170  C_U(cell_index, cell_thread) = 0.0;
171  C_V(cell_index, cell_thread) = 0.0;
172 } end_c_loop(cell_index, cell_thread)
173 }
174 Message("\nINITIALIZATION IS COMPLETED BY THE UDF(1)!\n");
175 }
176
177 /*=====
178 /* SPECIFY SOURCE TERMS FOR THE VELOCITY AND TEMPERATURE FIELDS */
179 =====*/
180
181 /*-----
182 /* DIMENSIONAL MHD-FHD SOURCE TERMS OF THE MOMENTUM EQUATION -U */
183 /*-----*/
184 DEFINE_SOURCE(source_term_momentum_u, cell_index, cell_thread, dS, eqn)
185 {
186 real u, v, T, Tc, H0, u_max, K;
187
188 real Mx, My;
189
190 real Hx, DHxDx, DHxDy;
191 real Hy, DHyDx, DHyDy;
192
193 real Bx, DBxDx, DBxDy;
194 real By, DByDx, DByDy;
195
196 real term_FHD_momentum_equation_u, term_MHD_momentum_equation_u, source = 0.0;
197
198 Hx = C_UDMI(cell_index, cell_thread, UDM_Hx);
199 DHxDx = C_UDMI(cell_index, cell_thread, UDM_DHxDx);
200 DHxDy = C_UDMI(cell_index, cell_thread, UDM_DHxDy);
201
202 Hy = C_UDMI(cell_index, cell_thread, UDM_Hy);
203 DHyDx = C_UDMI(cell_index, cell_thread, UDM_DHyDx);
204 DHyDy = C_UDMI(cell_index, cell_thread, UDM_DHyDy);
205
206 Bx = C_UDMI(cell_index, cell_thread, UDM_Bx);
207 DBxDx = C_UDMI(cell_index, cell_thread, UDM_DBxDx);
208 DBxDy = C_UDMI(cell_index, cell_thread, UDM_DBxDy);
209
210 By = C_UDMI(cell_index, cell_thread, UDM_By);
```

```
211  DByDx = C_UDMI(cell_index,cell_thread,UDM_DByDx);
212  DByDy = C_UDMI(cell_index,cell_thread,UDM_DByDy);
213
214  /*T = C_UDMI
215   (cell_index,cell_thread,UDM_DIMENSIONAL_TEMPERATURE_FIELD_FIXED); */
216  T = C_T(cell_index,cell_thread);
217  Tc = Tu;
218
219  H0 = sqrt((MnM*mu)/(mu0*mu0*h*h*sigma));
220  /* H0 = B/mu0; */
221  umax = (Re*mu)/(rho*h);
222  K = (MnF*rho*umax*umax)/(mu0*H0*H0*(Tu-Tl));
223
224  u = C_U(cell_index,cell_thread);
225  v = C_V(cell_index,cell_thread);
226
227  Mx = K*Hx*(Tc-T);
228  My = K*Hy*(Tc-T);
229
230  term_FHD_momentum_equation_u = 0.0;
231  term_MHD_momentum_equation_u = -sigma*u*(By*By);
232
233  term_FHD_momentum_equation_u = mu0*Mx*DxDx;
234  /* term_MHD_momentum_equation_u = sigma*(-u*By*By+v*Bx*By); */
235  term_MHD_momentum_equation_u = -sigma*u*(By*By);
236
237  source = term_FHD_momentum_equation_u + term_MHD_momentum_equation_u;
238  dS[eqn] = 0.0;
239
240  return(source);
241 }
242 */
243 /* DIMENSIONAL MHD-FHD SOURCE TERMS OF THE MOMENTUM EQUATION -V */
244 /*
245 DEFINE_SOURCE(source_term_momentum_v, cell_index, cell_thread, dS, eqn)
246 {
247  real u, v, T, Tc, H0, umax, K;
248
249  real Mx,My;
250
251  real Hx,DxDx,DxDy;
252  real Hy,DHyDx,DHyDy;
253
254  real Bx,DBxDx,DBxDy;
255  real By,DByDx,DByDy;
256
257  real term_FHD_momentum_equation_v, term_MHD_momentum_equation_v, source =
258  0.0;
259  Hx = C_UDMI(cell_index,cell_thread,UDM_Hx);
260  DxDx = C_UDMI(cell_index,cell_thread,UDM_DxDx);
261  DxDy = C_UDMI(cell_index,cell_thread,UDM_DxDy);
```

```
262
263 Hy = C_UDMI(cell_index,cell_thread,UDM_Hy);
264 DHyDx = C_UDMI(cell_index,cell_thread,UDM_DHyDx);
265 DHyDy = C_UDMI(cell_index,cell_thread,UDM_DHyDy);
266
267 Bx = C_UDMI(cell_index,cell_thread,UDM_Bx);
268 DBxDx = C_UDMI(cell_index,cell_thread,UDM_DBxDx);
269 DBxDy = C_UDMI(cell_index,cell_thread,UDM_DBxDy);
270
271 By = C_UDMI(cell_index,cell_thread,UDM_By);
272 DByDx = C_UDMI(cell_index,cell_thread,UDM_DByDx);
273 DByDy = C_UDMI(cell_index,cell_thread,UDM_DByDy);
274
275 /* T = C_UDMI
   (cell_index,cell_thread,UDM_DIMENSIONAL_TEMPERATURE_FIELD_FIXED); */
276 T = C_T(cell_index,cell_thread);
277 Tc = Tu;
278
279 H0 = sqrt((MnM*mu)/(mu0*mu0*h*h*sigma));
280 /* H0 = B/mu0; */
281 umax = (Re*mu)/(rho*h);
282 K = (MnF*rho*umax*umax)/(mu0*H0*H0*(Tu-Tl));
283
284 u = C_U(cell_index,cell_thread);
285 v = C_V(cell_index,cell_thread);
286
287 Mx = K*Hx*(Tc-T);
288 My = K*Hy*(Tc-T);
289
290 term_FHD_momentum_equation_v = 0.0;
291 /* term_MHD_momentum_equation_v = sigma*(u*Bx*By - v*Bx*Bx); */
292
293 /* term_FHD_momentum_equation_v = mu0*Mx*DHyDx; */
294 term_MHD_momentum_equation_v = 0.0;
295
296 /* term_FHD_momentum_equation_v = 0.0; */
297 /* term_MHD_momentum_equation_v = 0.0; */
298
299 source = term_FHD_momentum_equation_v + term_MHD_momentum_equation_v;
300 /*source = source/Vol;*/
301 dS[eqn] = 0.0;
302 return(source);
303 }
304
305 /
*-----*/
306 /* DIMENSIONAL AND DIMENSIONLESS MHD-FHD SOURCE TERMS OF THE TEMPERATURE
   EQUATION */
307 /
*-----*/
308 DEFINE_SOURCE(source_term_temperature, cell_index, cell_thread, dS, eqn)
```

```
309  {
310    real u, v, T, H0, umax, K;
311
312    real Mx, My;
313
314    real Hx, DHxDx, DHxDy;
315    real Hy, DHyDx, DHyDy;
316
317    real Bx, DBxDx, DBxDy;
318    real By, DByDx, DByDy;
319
320    real term_FHD_temperature_equation, term_MHD_temperature_equation, source = ↵
321      0.0;
322
323    Hx = C_UDMI(cell_index, cell_thread, UDM_Hx);
324    DHxDx = C_UDMI(cell_index, cell_thread, UDM_DHxDx);
325    DHxDy = C_UDMI(cell_index, cell_thread, UDM_DHxDy);
326
327    Hy = C_UDMI(cell_index, cell_thread, UDM_Hy);
328    DHyDx = C_UDMI(cell_index, cell_thread, UDM_DHyDx);
329    DHyDy = C_UDMI(cell_index, cell_thread, UDM_DHyDy);
330
331    Bx = C_UDMI(cell_index, cell_thread, UDM_Bx);
332    DBxDx = C_UDMI(cell_index, cell_thread, UDM_DBxDx);
333    DBxDy = C_UDMI(cell_index, cell_thread, UDM_DBxDy);
334
335    By = C_UDMI(cell_index, cell_thread, UDM_By);
336    DByDx = C_UDMI(cell_index, cell_thread, UDM_DByDx);
337    DByDy = C_UDMI(cell_index, cell_thread, UDM_DByDy);
338
339    u = C_U(cell_index, cell_thread);
340    /* T = C_UDMI
341       (cell_index, cell_thread, UDM_DIMENSIONAL_TEMPERATURE_FIELD_FIXED); */
342    T = C_T(cell_index, cell_thread);
343
344    H0 = sqrt((MnM*mu)/(mu0*mu0*h*h*sigma));
345    /* H0 = B/mu0; */
346    /* By = mu0*H0; */
347    umax = (Re*mu)/(rho*h);
348    K = (MnF*rho*umax*umax)/(mu0*H0*H0*(Tu-Tl));
349
350    term_FHD_temperature_equation = mu0*K*Hy*T*u*DHyDx;
351
352    /* term_FHD_temperature_equation = 0.0; */
353
354    term_MHD_temperature_equation = sigma*(By*By)*(u*u);
355
356    /* "VISCOS HEATING" OPTION IS SWITCHED ON IN THE FLUENT VISCOS PANEL
357       SETTINGS (=>VISCOS DISSIPATION TERM IS SWITCHED ON BY FLUENT) */
358    source = term_FHD_temperature_equation+term_MHD_temperature_equation;
359    dS[eqn] = 0.0;
```

```
359     return(source);
360 }
362 /
363 */
364 /* EXECUTE AT THE END OF THE COMPUTATIONAL LOOP FOR SOLVING THE SYSTEM OF
   GOVERNING EQUATIONS */
365 /
366 */
366 DEFINE_EXECUTE_AT_END(execute_at_end)
367 {
368     cell_t cell_index;
369     Thread *cell_thread;
370     Domain *domain;
371
372     real T;
373
374     domain = Get_Domain(1);
375
376 /
377 */
377 /* INITIAL DISTRIBUTION OF THE VELOCITY COMPONENTS (U,V) FROM THE LOWER
   WALL TO THE UPPER WALL */
378 /
379 */
379 thread_loop_c(cell_thread,domain)
380 {
381     begin_c_loop(cell_index,cell_thread)
382     {
383         T = C_T(cell_index,cell_thread);
384         C_UDMI(cell_index,cell_thread,UDM_DIMENSIONLESS_TEMPERATURE_FIELD) = (T-
385             T1)/(Tu-T1);
386     } end_c_loop(cell_index,cell_thread)
387 }
388
389 */
390 /* SPECIFY BOUNDARY CONDITIONS FOR THE VELOCITY AND TEMPERATURE FIELDS */
391 */
392
393 */
394 /* INLET DIMENSIONAL AND DIMENSIONLESS VELOCITY PROFILES */
395 */
396 DEFINE_PROFILE(inlet_velocity_profile, face_thread, velocity_index)
397 {
398     real xc[ND_ND], y, umax;
399     face_t face_index;
```

```
401  /* DIMENSIONLESS VELOCITY PROFILE */
402  begin_f_loop(face_index,face_thread)
403  {
404      F_CENTROID(xc,face_index,face_thread);
405      y = xc[1];
406      umax = (Re*mu)/(rho*h); /* OJO*/
407      F_PROFILE(face_index,face_thread,velocity_index) = 4.0*umax*(y/ h)*(1.0-
408          (y/h));
409  } end_f_loop(face_index,face_thread)
410 }
411 /*
412 /* INLET DIMENSIONAL AND DIMENSIONLESS TEMPERATURE PROFILES */
413 */
414 DEFINE_PROFILE(inlet_temperature_profile, face_thread, temperature_index)
415 {
416     real xc[ND_ND], y;
417     face_t face_index;
418
419     /* DIMENSIONAL TEMPERATURE PROFILE */
420     begin_f_loop(face_index,face_thread)
421     {
422         F_CENTROID(xc,face_index,face_thread);
423         y = xc[1];
424         F_PROFILE(face_index,face_thread,temperature_index) = Tl+(y/h)*(Tu-Tl);
425     } end_f_loop(face_index,face_thread)
426 }
427 /*
428 /* DIMENSIONAL AND DIMENSIONLESS COEFFICIENT OF THERMAL DIFFUSIVITY */
429 */
430 /*
431 DEFINE_PROPERTY(thermal_diffusivity_coefficient, cell_index, cell_thread)
432 {
433     real thermal_diffusivity_coefficient = 0.0;
434
435     thermal_diffusivity_coefficient = k;
436
437     return(thermal_diffusivity_coefficient);
438 }
439 /*
440 /* DIMENSIONAL AND DIMENSIONLESS COEFFICIENT OF VISCOS DIFFUSIVITY */
441 */
442 /*
443 DEFINE_PROPERTY(viscous_diffusivity_coefficient, cell_index, cell_thread)
444 {
445     real viscous_diffusivity_coefficient;
446     real shear_rate = C_STRAIN_RATE_MAG(cell_index, cell_thread);
447     real Hy;
448     Hy = C_UDMI(cell_index,cell_thread,UDM_Hy);
449     /*
450         if (shear_rate < 1e-33)
451         {
452             viscous_diffusivity_coefficient = mu;
```

```
453     }
454     else {
455         viscous_diffusivity_coefficient = mu;
456         /* Casson*/
457         /*viscous_diffusivity_coefficient = (sqrt(eta_c) +sqrt(tau_c /
458             shear_rate))*(sqrt(eta_c) +sqrt(tau_c / shear_rate)); */
459         /* viscous_diffusivity_coefficient = (1 / shear_rate) * (tau_c +
460             eta_c * (alpha_two * sqrt(shear_rate) + alpha_one *
461                 shear_rate)); /* K-L*/
462         /* viscous_diffusivity_coefficient = (sqrt(eta_c) + (sqrt(tau_c)) /
463             (sqrt(lambda) + sqrt(shear_rate))) * (sqrt(eta_c) + (sqrt(tau_c)) /
464                 (sqrt(lambda) + sqrt(shear_rate))); /* Modified Casson*/
465         /*Quemada*/
466         /* viscous_diffusivity_coefficient= mu_f/pow((1-0.5*(k_zero+k_inf*sqrt(
467             (shear_rate/gamma_c))/(1+sqrt(shear_rate/gamma_c))*phi),2); */
468
469     /* DEFINE_DIFFUSIVITY(diffusive_coefficient, cell_index, cell_thread,
470         diffusivity_index) */
471     /* END */
472
473
```

6. Appendix

6.3 Appendix 3. MATLAB Code

6.3.1 Non-Newtonian Plot Code

```
% MSc Thesis Non Newtonian and Comp Vel profiles Marc Barcelo
clc
clear all;
format long;
clc;
clear all;
mu= 3.2e-3;
%Casson: eta_c 0.00414 tau_c 0.0038 / K-L: eta_c_kl = 0.0035, tau_c=0.005, ↴
alpha_1=1, alpha_2=1.19523 / Modified Casson: eta_c = 0.002982, tau_c=0.002876, ↴
lambda= 4.02 */
eta_c= 0.00414;
tau_c= 0.0038;
eta_c_kl = 0.0035;
tau_c_kl=0.005
lambda= 4.020;
alpha_1=1;
alpha_2= 1.19523;
eta_c_mod = 0.002982,
tau_c_mod =0.002876,
mu_f= 1.2e-3;
phi=0.45;
gamma_c=5;
k_inf=1.5;
k_0=4;
i=1;
for (shear_rate=0.01:0.01:1000)
    shear_rate_vec(i)=shear_rate;
    mu(i)=3.2e-3;
    powerlaw(i)=0.017*shear_rate^(0.708-1);
    casson(i)= (sqrt(eta_c) +sqrt(tau_c / shear_rate))*(sqrt(eta_c) +sqrt(tau_c / ↴
shear_rate));
    casson_kl(i)= (1 / shear_rate) * (tau_c_kl + eta_c_kl * (alpha_2 * sqrt ↴
(shear_rate) + alpha_1 * shear_rate));
    casson_mod(i)=(sqrt(eta_c_mod) + (sqrt(tau_c_mod)) / (sqrt(lambda) + sqrt ↴
(shear_rate))) * (sqrt(eta_c_mod) + (sqrt(tau_c_mod)) / (sqrt(lambda) + sqrt ↴
(shear_rate)));
    sqrt_gamma_ratio = sqrt(shear_rate/gamma_c);
    k = (k_0+k_inf*sqrt_gamma_ratio)/(1+sqrt_gamma_ratio);
    mu_q = mu_f/(1-0.5*k*phi)^2;
    %kq=(k_0 +k_inf*sqrt (shear_rate/gamma_c))/(1+sqrt (shear_rate/gamma_c));
    quemada(i)= mu_q;
    i=i+1;
end
figure
loglog(shear_rate_vec,mu,'--k');
hold on
loglog(shear_rate_vec, powerlaw);
hold on
loglog(shear_rate_vec,casson, '-.')
hold on
loglog(shear_rate_vec,casson_kl, '--xb')
```

```

hold on
loglog(shear_rate_vec, casson_mod, ':')
hold on
loglog(shear_rate_vec, quemada, '.')
title('Comparison of the different Non-Newtonian Models')
ylabel('Effective viscosity \eta')
xlim([0.1 1000])
ylim([0.002 0.1])
xlabel(' Shear rate \gamma');
legend('Newtonian','Power-Law', 'Casson Standard', 'Casson K-L', 'Casson Modified',  

'Quemada')
%% Velocity Profile mu ct
mu = importdata('mu_ct\Results\u(x=3).dat');
N= length(mu(:,1));
Y_mu = zeros(N,1);
Vel_mu= zeros(N,1);
Y_mu = mu(:,1);
Vel_mu = mu(:,2);
N=0;
% WSS mu ct
wss_mu= importdata('mu_ct\wss.txt');
N= length(wss_mu(:,1));
X_mu = zeros(N,1);
X_mu = wss_mu(:,1);
WSS_mu_lower = wss_mu(:,2);
WSS_mu_upper = wss_mu(:,3);
N=0;

pow = importdata('power_law\Results\u(x=3).dat');
N= length(pow(:,1));
Y_pow = zeros(N,1);
Vel_pow = zeros(N,1);
Y_pow = pow(:,1);
Vel_pow = pow(:,2);
N=0;

cas_n= importdata('Casson_normal\Results\u(x=3).dat');
N= length(cas_n(:,1));
Y_cas_n = zeros(N,1);
Vel_cas_n = zeros(N,1);
Y_cas_n = cas_n(:,1);
Vel_cas_n = cas_n(:,2);
N=0;
% WSS Casson
wss_cas= importdata('Casson_normal\wss.txt');
N= length(wss_cas(:,1));
X_cas = zeros(N,1);
X_cas = wss_cas(:,1);
WSS_cas_lower = wss_cas(:,2);
WSS_cas_upper = wss_cas(:,3);
N=0;

cas_kl = importdata('Casson_KL\Results\u(x=3).dat');

```

```

N= length(cas_kl(:,1));
Y_cas_kl = zeros(N,1);
Vel_cas_kl = zeros(N,1);
Y_cas_kl = cas_kl(:,1);
Vel_cas_kl = cas_kl(:,2);
N=0;
% WSS Casson KL
wss_cas_kl= importdata('Casson_KL\wss.txt');
N= length(wss_cas_kl(:,1));
X_cas_KL = zeros(N,1);
X_cas_KL = wss_cas_kl(:,1);
WSS_caskl_lower = wss_cas_kl(:,2);
WSS_caskl_upper = wss_cas_kl(:,3);
N=0;

cas_mod = importdata('Casson_Modified\Results\u(x=3).dat');
N= length(cas_mod(:,1));
Y_cas_mod = zeros(N,1);
Vel_cas_mod = zeros(N,1);
Y_cas_mod = cas_mod(:,1);
Vel_cas_mod = cas_mod(:,2);
N=0;
% WSS Casson KL
wss_cas_mod= importdata('Casson_Modified\wss.txt');
N= length(wss_cas_mod(:,1));
X_cas_mod = zeros(N,1);
X_cas_mod = wss_cas_mod(:,1);
WSS_mod_lower = wss_cas_mod(:,2);
WSS_mod_upper = wss_cas_mod(:,3);
N=0;

quem = importdata('Quemada\Results\u(x=3).dat');
N= length(quem(:,1));
Y_quem = zeros(N,1);
Vel_quem = zeros(N,1);
Y_quem = quem(:,1);
Vel_quem= quem(:,2);
N=0;
% WSS quem
wss_quem= importdata('Quemada\wss_low.dat');
N= length(wss_quem(:,1));
X_quem = zeros(N,1);
X_quem = wss_quem(:,1);
WSS_quem_lower = wss_quem(:,2);
wss_quem_up= importdata('Quemada\wss_upp.dat');
N= length(wss_quem_up(:,1));
X_quem_up = zeros(N,1);
X_quem_up = wss_quem_up(:,1);
WSS_quem_upper = wss_quem_up(:,2);

```

figure

```

plot(Vel_mu,Y_mu, '--k')
hold on
plot(Vel_pow,Y_pow, '-.')
hold on
plot(Vel_cas_n,Y_cas_n, '--xb')
hold on
plot(Vel_cas_kl, Y_cas_kl, ':')
hold on
plot(Vel_cas_mod, Y_cas_mod)
hold on
plot(Vel_quem, Y_quem, '.')

title('Velocity profile at x/h=7')
ylabel('Y coordinate (m)')
ylim([0 0.05])
xlabel('X-Velocity (m/s)');
legend('Newtonian', 'Power-Law', 'Casson Standard', 'Casson K-L', 'Casson Modified', 'Quemada')

norm_1_pow = 0; norm_1_cas_n=0; norm_1_cas_m=0; norm_1_cas_kl=0; norm_1_quem=0;
norm_3_pow=0; norm_3_cas_n=0; norm_3_cas_mod=0; norm_3_cas_kl=0; norm_3_quem =0;
for i=1:41
    % Norm 1
    norm_1_pow=norm_1_pow +abs( Vel_mu(i,1)-Vel_pow(i,1));
    norm_1_cas_n=norm_1_cas_n +abs( Vel_mu(i,1)-Vel_cas_n(i,1));
    norm_1_cas_m=norm_1_cas_m +abs( Vel_mu(i,1)-Vel_cas_mod(i,1));
    norm_1_cas_kl= norm_1_cas_kl +abs( Vel_mu(i,1)-Vel_cas_kl(i,1));
    norm_1_quem= norm_1_quem +abs( Vel_mu(i,1)-Vel_quem(i,1));
    % Norm 3
    if (abs(Vel_mu(i,1)-Vel_pow(i,1))> norm_3_pow)
        norm_3_pow=abs(Vel_mu(i,1)-Vel_pow(i,1));
    end

    if (abs(Vel_mu(i,1)-Vel_cas_n(i,1))>norm_3_cas_n)
        norm_3_cas_n=abs( Vel_mu(i,1)-Vel_cas_n(i,1));
    end
    if (abs(Vel_mu(i,1)-Vel_cas_mod(i,1))>norm_3_cas_mod)
        norm_3_cas_mod=abs(Vel_mu(i,1)-Vel_cas_mod(i,1));
    end
    if (abs(Vel_mu(i,1)-Vel_cas_kl(i,1))>norm_3_cas_kl)
        norm_3_cas_kl=abs( Vel_mu(i,1)-Vel_cas_kl(i,1));
    end
    if (abs(Vel_mu(i,1)-Vel_quem(i,1))>norm_3_quem)
        norm_3_quem=abs( Vel_mu(i,1)-Vel_quem(i,1));
    end
end
norm_1_pow=norm_1_pow/41;
norm_1_cas_n=norm_1_cas_n/41;
norm_1_cas_m=norm_1_cas_m/41;
norm_1_cas_kl=norm_1_cas_kl/41;
norm_1_quem=norm_1_quem/41;
%Norm 2
norm_2_pow=immse(Vel_mu,Vel_pow);
norm_2_cas_n=immse(Vel_mu,Vel_cas_n);

```

```

norm_2_cas_m=immse(Vel_cas_mod,Vel_mu);
norm_2_cas_kl=immse(Vel_mu,Vel_cas_kl);
norm_2_quem=immse(Vel_mu,Vel_quem);

figure
plot(X_mu,WSS_mu_lower, '--k')
hold on
plot(X_cas,WSS_cas_lower, '--xb')
hold on
plot(X_cas_KL, WSS_caskl_lower, ':')
hold on
plot(X_cas_mod, WSS_mod_lower )
hold on
plot(X_quem, WSS_quem_lower, '.')

title('WSS Profile at lower wall')
ylabel('WSS (Pa)')
xlabel(' X Position (m)');
legend('Newtonian', 'Casson Standard', 'Casson K-L', 'Casson Modified', 'Quemada')

figure
plot(X_mu,WSS_mu_upper, '--k')
hold on
plot(X_cas,WSS_cas_upper, '--xb')
hold on
plot(X_cas_KL, WSS_caskl_upper, ':')
hold on
plot(X_cas_mod, WSS_mod_upper )
hold on
plot(X_quem, WSS_quem_upper, '.')

title('WSS Profile at upper wall')
ylabel('WSS (Pa)')
xlabel(' X Position (m)');
legend('Newtonian', 'Casson Standard', 'Casson K-L', 'Casson Modified', 'Quemada')

% WSS quem
wss_mag_low= importdata('mu_ct/wss_magnetoviscous_lower.dat');
N= length(wss_quem(:,1));
X_mag = zeros(N,1);
X_mag = wss_mag_low(:,1);
WSS_mag_lower = wss_mag_low(:,2);
wss_mag_up= importdata('mu_ct/wss_magnetoviscous_upper.dat');
X_mag_up = wss_mag_up(:,1);
WSS_mag_upper = wss_mag_up(:,2);

figure
plot( X_mu, WSS_mu_lower,'-.k', X_mag, WSS_mag_lower, '--b')
ylabel('WSS (Pa) Lower Wall')
xlabel(' X Position (m)');
legend('Newtonian', 'Magnetoviscous Contribution')

figure

```

```
plot( X_mu, WSS_mu_upper, '-.k', X_mag_up, WSS_mag_upper, '--b')
ylabel('WSS (Pa) Upper Wall')
xlabel(' X Position (m)');
legend('Newtonian', 'Magnetoviscous Contribution')
```

6. Appendix

6.3.2 Rayleigh-Bénard Plot Code

```
dens=1060;
g=9.81;
cp=3617
k=0.52;
mu=0.0032;
nu=mu/dens;
beta=0.000257;
alpha=k/(dens*cp);
deltaT= 1;
%% Ra against h
h=0.0001:0.0001:0.05;
Ra=(beta*g*deltaT*h.^3)/(alpha*nu);
figure
plot (h(Ra<3000),Ra(Ra<3000), '--k');
hold on;
plot(h(Ra>1708), Ra(Ra>1708), 'r');
xlim([0 0.008])
xlabel('h (m)')
ylabel('Ra')
%% Ra against DeltaT
h=0.05;
deltaT=0.0001:0.0001:4;
Ra=(beta*g*deltaT*h.^3)/(alpha*nu);
figure
plot (deltaT(Ra<3000),Ra(Ra<3000), '--k');
hold on;
plot(deltaT(Ra>1708), Ra(Ra>1708), 'r');
xlim([0 0.01])
xlabel('\Delta T (K)')
ylabel('Ra')
%%
Ra=1707.8;
h=0.003
deltaT_3=(alpha*nu*Ra)/(beta*g*h.^3);
h=0.004;
deltaT_4=(alpha*nu*Ra)/(beta*g*h.^3);
h=0.0053;
deltaT_5_3=(alpha*nu*Ra)/(beta*g*h.^3);
figure
scatter ( 3,deltaT_3)
hold on
scatter ( 4,deltaT_4)
hold on
scatter ( 5.3,deltaT_5_3)
plot(deltaT(Ra>1708), Ra(Ra>1708), 'r');
xlim([0 10])
ylabel('\Delta T (K)')
xlabel('diameter (mm)')
```